The Effect of Temperature and Crystallite Size on the Growth and Morphology of Carbon Nanotubes

Thesis submitted to the University of Cape Town as partial fulfilment of requirements for a Master of Science Degree in Chemical Engineering

By

Jacques N. Kleinsmidt

BSc Eng (Chemical)

February 2005

ACKNOWLEDGEMENTS

I would firstly like to thank my supervisor, Prof. Eric van Steen for his help and guidance throughout this study. His open door policy meant I could always receive both academic and personal guidance throughout the course of my Masters, which I deeply appreciate.

I would also like to thank Sasol for the opportunity to do a Masters degree and for the financial support as well as allowing me to perform experiments vital to the study in the labs in Sasolburg. I also would like to thank my supervisor at Sasol, Dr. Frans Prinsloo for organising trips to Wits and Pretoria for important characterisation.

I would like to thank the University of Cape Town especially the Post Graduate Funding Office for additional financial assistance. I would like to also thank the Catalysis Research Unit and the Chemical Engineering Department in general including Dr. Michael Claeys and Helen Divey for allowing me the use of the facilities. I also would like to thank Mohammed Jaffer for his help and patience when using the Electron Microscope. I would also like to thank Itai Mabaso for his input and his patience when explaining important concepts.

I would finally like to thank my friends and family for helping me through this process. There is one special friend who was always patient and understanding and for that I am always grateful.

SYNOPSIS

The aim of the study was to synthesise iron oxide crystallites with different crystallite sizes supported on γ-Al_2O_3 using the reverse micelle technique. It was hypothesised that changing the crystallite size of the synthesised iron oxide crystallites could lead to the control of the external nanotube diameter. The effect of temperature on the external diameter and productivity was also investigated.

It was found through titration and AAS that the iron loading was lower than the expected 15 wt.-%. Furthermore, it was observed that the loading was not consistent through different catalyst samples. This was attributed to incomplete precipitation of iron using the reverse micelle technique, the rigorous cleaning regime implemented and weak metal-support interaction. It was found through XRD and TEM that crystallites in the nanometre range were produced although they were not well distributed over the support. It was also found that the expected linear relationship between water to surfactant ratio and crystallite size was not achieved. Hence the obtained crystallite sizes were significantly different from those obtained in the work by Mabaso (2005).

The productivity of carbon nanotubes was determined gravimetrically. At low temperature, the productivity increases with increasing temperature and is governed by kinetics (possibly due to low diffusion coefficients and carbon decomposition rates). At higher temperature, the productivity decreases with increasing temperature. At this stage it is still unclear whether the productivity at high temperature is controlled by catalyst deactivation (encapsulation of the crystals with carbon) or by thermodynamic limitations. In the case of kinetic limitations, there is some evidence of encapsulation of the iron oxide crystallites with carbon, which may prevent further growth of the carbon nanotubes. However, the productivity of carbon nanotubes might be thermodynamically limited. From the temperature dependency of the ratio of the partial pressures of the exiting gases, a heat of reaction for the formation of carbon nanotubes of -

233 kJ/mol was determined. This is significantly higher than that for the temperature dependency for the Boudouard reaction. Furthermore, it was noted that if thermodynamic limitations play a role in the synthesis of carbon nanotubes, the formation of carbon nanotubes is energetically less favoured than the formation of graphite. This might be attributed to strain energy present in nanotubes as opposed to planar graphite.

The carbon nanotube external diameters were not equal to the iron oxide crystallite diameters for a constant synthesis temperature. This was attributed to sintering of the iron crystallites under reduction and synthesis conditions. The poor metal distribution on the support and the weak metal-support interaction may have enhanced sintering. It was found that the external nanotube diameter did increase with an increase in water to surfactant ratio.

It was found that the external nanotube diameter both increased and decreased with an increase in temperature becoming more uniform. The increase was again attributed to sintering. The decrease was attributed to the formation of a quasi-liquid state composed of iron oversaturated with carbon. It is believed that sintering and redispersion of the iron oxide crystallites took place to produce a narrower Gaussian distribution. This produced carbon nanotubes with a narrower and more uniform external nanotube diameter. It was also found that more than one growth mechanism might be present at elevated temperatures from the tip growth mechanism at low temperature to both the tip growth and base growth mechanisms at elevated temperatures.

TABLE OF CONTENTS

PAGE

LIST OF FIGURES

PAGE

LIST OF TABLES

PAGE

CHAPTER 1: AN INTRODUCTION TO CARBON NANOTUBES

1.1 A Brief History of Carbon Filaments and Future Outlook

Carbon nanotubes were first discovered by Iijima (1991) during the production of fullerenes (C_{60}) in the arc-discharge process. The formation of graphitic carbon in the form of carbon filaments was at that stage well known and extensively studied. Filamentous carbon was formed in reactions of industrial and economic importance and can lead to the destruction of the catalyst, the catalyst support structure as well as doing great damage to the reactor itself (Rostrup-Nielsen, 1984; de Bokx et al., 1985a).

Initially, the study on filamentous carbon was focused on the mechanisms of nucleation and growth in order to gain a better understanding of this form of carbon with a view to suppress its formation (Baker et al., 1972; Yang and Chen, 1989). Since the discovery of carbon nanotubes by Iijima (1991) which appear to have similarities to filamentous carbon, studies have been focused on understanding the unique properties of carbon nanotubes and finding new and exciting applications for these aforementioned nanotubes (Ajayan and Zhou, 2001; Popov, 2004). Previous studies now form a very important foundation for the understanding of the formation of carbon nanotubes.

1.2 Basic Morphology and Structure of Carbon Nanotubes

In order to exploit the unique properties of carbon nanotubes, it is important to first understand the basic structure and morphology of these materials. Carbon nanotube research often focuses on either single-walled carbon nanotubes (SWNT) (Iijima and Ichihashi, 1993; Bethune et al., 1993) or multi-walled carbon nanotubes (MWNT) (Iijima, 1991). The difference between these two types of

carbon nanotubes is the number of carbon sheets, which form the walls of these materials (see Figure 1-1 and Figure 1-2).

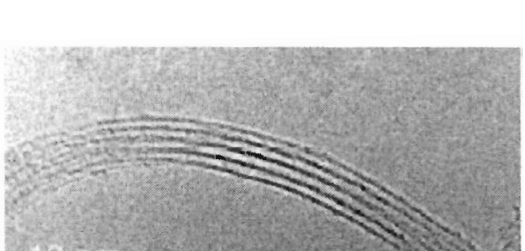

Figure 1- 1. A TEM image of a group of single-walled nanotubes. Single-walled nanotubes are often found in nanoropes composed of a number of single-walled nanotubes. (Daenen et al., 2003)

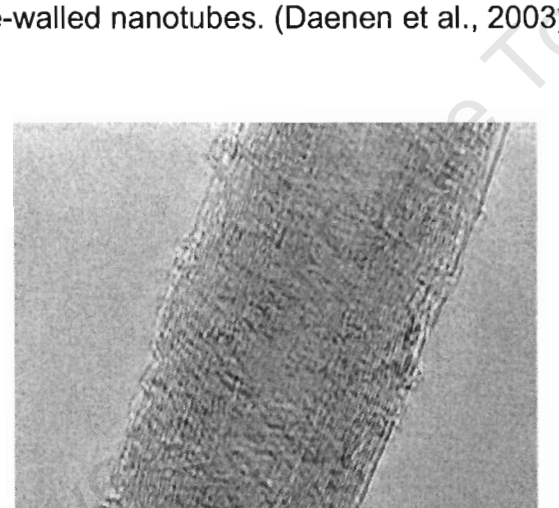

Figure 1- 2. HRTEM image of a multi-walled carbon nanotube (Kibria et al., 2002)

Single-walled nanotubes are rarely seen individually. They tend to form nanoropes, which are composed of a number of individual SWNTs in a triangular lattice. Multi-walled nanotubes can appear with either a parallel orientation or a fishbone orientation of the sheets (Hoogenraad, 1995) as seen in Figure 1-3. In the parallel structure we see that basal planes are exposed where as in the

fishbone structure, only edge planes are exposed. The obtained morphology is dependent on the catalyst used during synthesis.

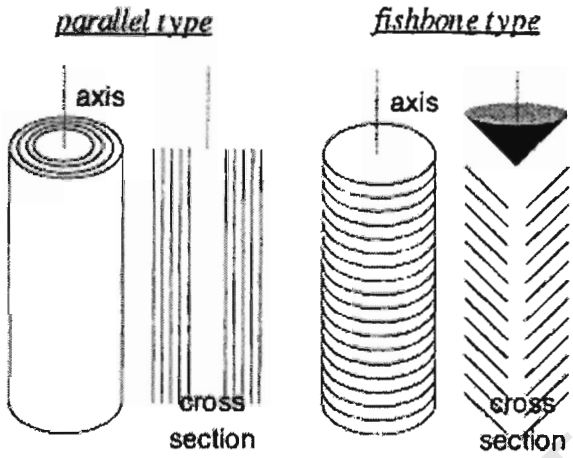

Figure 1- 3. Simplified structure showing parallel multi-walled nanotube (left) and fishbone multi-walled carbon nanotube (right), (Hoogenraad, 1995)

For the purpose of this work it is important to differentiate between carbon fibrils and carbon nanotubes. The former, carbon fibrils, will refer to a structure lacking the hollow internal cavity while a carbon nanotube will refer to a structure with a hollow internal cavity.

1.3 Atomic Structure of Carbon Nanotubes

Carbon nanotubes are a form of graphitic carbon in which carbon is in the sp^2 hybridization state with carbon atoms in a honeycomb formation. Taking SWNTs as a template for MWNTs, an ideal nanotube can be visualized as an infinite sheet of graphite (graphene sheet – see Figure 1-4), which is then rolled up into a seamless cylinder with a cylindrical symmetry.

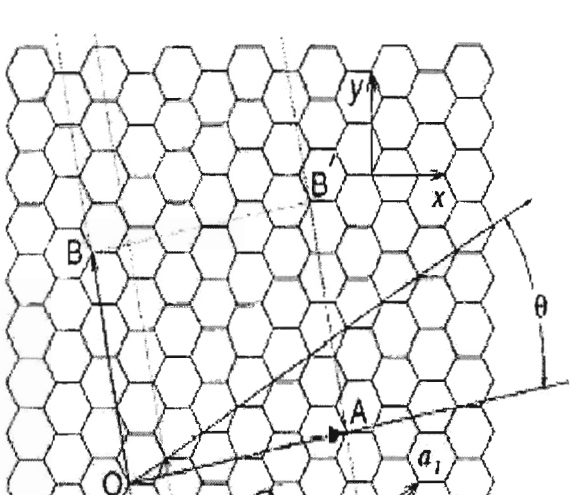

Figure 1- 4. A 2-D representation of the graphene sheet used to define the type of carbon nanotube (Dresselhaus et al., 1995)

The manner in which the graphene sheet is rolled up determines not only the structure of the nanotube but also its electronic properties. Figure 1-4 shows an infinite graphene sheet bounded by the rectangle OAB'B. The unit cell of a nanotube can be formed by overlapping the atom at O with A and B' with B. The chiral vector $\mathbf{C}_h$ is defined as $\mathbf{C}_h = n\mathbf{a}_1 + m\mathbf{a}_2$, where $\mathbf{a}_1$ and $\mathbf{a}_2$ are unit vectors and n and m are integers. The chiral vector itself is perpendicular to the nanotube axis and corresponds to the circumference of the nanotube. The chirality or twist of the nanotube is determined by the values of n and m. This determines the structure and physical properties e.g. whether the tubes are conducting or semi-conducting.

Table 1- 1. The three unique structures of carbon nanotubes

Type of Nanotube	Chiral Angle (θ)	(n,m)
Armchair	30°	$n = m$
Zigzag	0°	n or $m = 0$
Chiral	$0° < \theta < 30°$	N/A

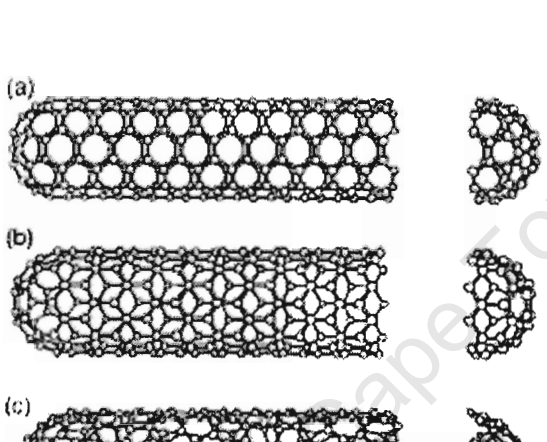

Figure 1- 5. Simplified diagram showing the 3 types of nanotubes with (a) armchair, (b) zigzag and (c) chiral (Dresselhaus et al., 1995)

The ideal nanotube is characterized by a large aspect ratio with a length to diameter ratio of up till 1000 and in the case of MWNTs a lattice spacing of 0.34 nm (Iijima, 1991).

The tube ends of these carbon nanotubes may be either open or capped after synthesis. The end of capped carbon nanotubes is encapsulated with carbon. A closed carbon nanotube may subsequently be opened after synthesis via a post-treatment step.

1.4 Unique Properties and Possible Applications of Carbon Nanotubes

The interesting properties associated with carbon nanotubes as well as fibrils include their electrical conductivity, mechanical strength and chemical reactivity. It is thus worthwhile investigating these properties and identifying where possible applications may lie.

1.4.1 Electrical Conductivity

An important area in nanotube research is the electronic properties of carbon nanotubes. A sheet of graphite can be viewed as a semiconductor with a band gap (distance between the valence band and conducting band) of zero (Baughman et al., 2002). Nanotubes are unique because they can exhibit either metallic or semiconducting properties. The electronic behaviour depends on the "twist" or chirality of the tube (see Figure 1-5). An armchair SWNT is metallic in nature while tubes defined by the integer relationship, $n - m = 3k$ (with k a non-zero integer) are semiconducting with small band gaps. All other nanotubes are semiconductors with a band gap inversely proportional to the tube diameter (Dresselhaus et al., 1995). The tube tends towards becoming planar graphite, which has a band gap of zero as the tube diameter increases.

It should be mentioned that MWNTs have similar electronic properties to SWNTs because the concentric tubes in MWNTs are only weakly bound to each other via van der Waals forces, which do not impact hugely on the electronic properties.

1.4.2 Mechanical Strength

An important measure of strength of carbon nanotubes is its Young's modulus, which is defined as the ratio of stress versus strain. The stress can be seen as the force per unit area or pressure applied to the nanotube and the strain is the increase in length due to the stress applied relative to the original measured

length. Carbon fibrils have been reported to have a Young's modulus of 685 GPa (Jacobson et al., 1995) using a vibrating reed technique where an individual nanotube is mounted as a cantilever with one end fixed. For MWNTs, a Young's modulus of between 270 and 950 GPa was found (Yu et al., 2000). MWNTs have also been found to have a tensile strength (maximum stress applied before failure) of up to 75 times that of steel (Demczyk et al., 2002). The values quoted for nanotube strength should always be directly related to the experimental conditions and are highly dependent on the manner in which they are defined.

The main challenge associated with the application of carbon nanotubes in reinforcing composite materials is the difference in strength between individual nanotubes and agglomerates as single or individual nanotubes are rarely found. Single-walled nanotubes tend to be found in agglomerates or ropes (see Figure 1-6).

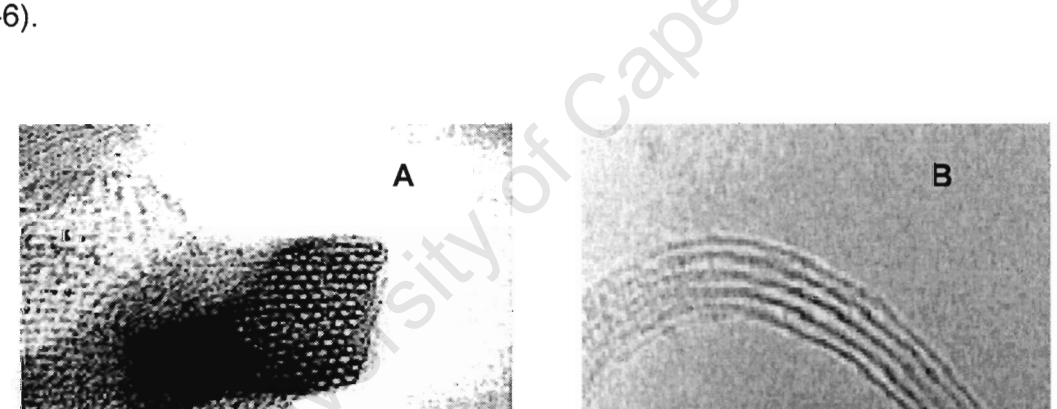

Figure 1- 6. (A) A SEM image of a typical nanorope composed of approximately 100 SWNTs. (Thess et al., 1996). (B) A TEM image of a side view of a nanorope segment. (Daenen et al., 2003)

Individual SWNT are expected to be stronger than MWNT. Theory has suggested that SWNTs might have a Young's modulus of up to 1 TPa (Yakobson et al., 1996). This difference is attributed to the sliding of the individual cylinders in MWNTs, which are only loosely bonded by van der Waals forces. This lower strength of MWNTs compared to SWNTs is analogous to the graphite layers sliding in the "lead" of a pencil. Demczyk et al. (2002) found that when nanotubes failed and broke into two separate pieces, the sum of the lengths of the two pieces were greater than the length of the original piece and this suggested a sword-in-sheath breaking mechanism. This accounts for the loss of strength in the nanotube agglomerates. A similar idea can be extended to SWNT ropes where the individual tubes which make up the rope can be broken from the rope due to shearing (Ayajan and Zhou, 2000) which could then compromise the strength of this rope altogether.

An interesting application of carbon nanotubes which combines both the mechanical strength and electrical conductivity is in their use as nanoprobes e.g. in a scanning probe microscope. The properties of nanotubes, which favour this application, are their strength, flexibility (ability to bend easily) as well as their high conductivity. Due to the slenderness of the tip, it has greater access to areas such as small surface cracks and because the tip is elastic, it will not be crushed but will simply buckle and reversibly regain its original shape, because the tip is elastic (Ajayan and Zhou, 2001).

1.4.3 Chemical Reactivity

In general, planar graphite is inert. Any reactions, which may occur, will be at defect sites in the ordered arrangement. These defects include missing atoms in the hexagonal lattice or where non-hexagons exist (Prinsloo, 2000). In the case of carbon nanotubes, the graphene layers are believed to have enhanced reactivity due to their curvature. This curvature results in both a pyramidalization of the conjugated carbon atoms and a mismatch of the pi-orbitals. This induces a

strain, which might lead to an enhanced chemical reactivity over planar graphite (Niyogi et al., 2002). Both the pyramidalization angle and pi-orbital mismatch are inversely proportional to the carbon nanotube diameter, which indicates that a smaller tube would probably be more reactive.

There are a number of challenges associated with the chemical reactivity of carbon nanotubes. Single-walled nanotubes as well as MWNTs are chemically inert (Niyogi et al., 2002) due to a lack of surface functional groups and appear to be hydrophobic (Prinsloo, 2000). Hence they are insoluble in any solvent (Kuzmany et al., 2004). These problems can be overcome by functionalizing the surface of the carbon nanotubes, e.g. by treating them with a strong oxidising agent such as nitric acid (Lui et al., 2002). Nitric acid serves to also open carbon nanotubes due the reactivity of the end caps, which have greater curvature relative to the side walls (Niyogi et al., 2002). Nitric acid also purifies the carbon nanotubes by removal of the metal catalysts and any amorphous carbon. Nitric acid introduces carboxyl and carbonyl groups, which can then serve as anchorage sites for positively charged metal complexes (Prinsloo, 2000). Functionalization of carbon nanotubes with azomethine has also been successful and has yielded SWNTs, which were soluble in both $CHCl_3$ and water (Kuzmany et al., 2004).

The chemical reactivity of carbon nanotubes shows great promise in the field of heterogeneous catalysis research. Research has focussed on the use of both carbon fibrils and nanotubes as a catalyst support (Hoogenraad, 1995; Prinsloo, 2000; Toebes et al., 2003). The role of the catalyst support is to disperse the catalytically active phase so as to achieve a large surface area to mass of catalyst used. Carbon nanotubes are believed to have great potential as a catalyst support because of their chemical and thermal stability, resistance to attrition and medium to high specific surface area (Nhut et al., 2002). The application of MWNTs as well as carbon fibrils as a catalyst support in liquid phase reactions has also been of great interest due to their mesoporosity, which

is believed to reduce mass-transfer limitations (Serp et al., 2003). The metal-support interactions and wall texture (basal versus edge planes exposed) can be directed using carbon fibrils and carbon nanotubes as the support material (De Jong and Geus, 2000).

A clear example of the advantages of MWNTs as a catalyst support over conventional grain size SiC was shown by Nhut et al (2003) in the selective oxidation of H_2S (see Figure 1-7). The sustained higher activity and conversion of MWNT-supported NiS_2 was attributed to the tubular structure of the nanotube support. The capillary forces allowed for the wetting of the inner walls by condensed steam, which transported the product sulphur out of the tubes. This allowed free access to the active sites and prevented deactivation by sulphur plugging.

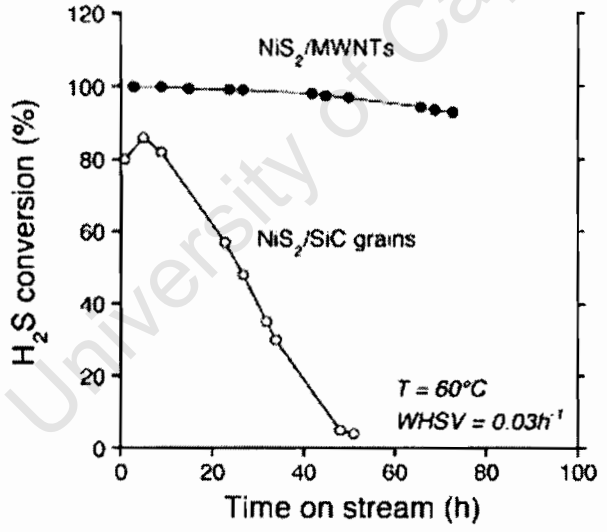

Figure 1- 7. Catalytic results of the selective oxidation of H_2S for SiC grains and MWNTs at 60°C and WHSV of 0.03h^{-1} (Nhut et al., 2003).

1.5 Synthesis of Carbon Nanotubes

Carbon nanotubes are synthesised by various methods but the most common are arc discharge (Iijima, 1991), laser ablation (Thess et al., 1996) and catalytic chemical vapour deposition (CVD) (Jose-Yacaman et al., 1992).

1.5.1 Arc Discharge

Nanotubes were accidentally discovered by Iijima (1991) during the arc discharge synthesis of fullerenes. Since then, the arc discharge technique has become a relatively simple method to synthesise carbon nanotubes with reasonable yields of up to 75 % relative to the solid carbon source (Ebbesen and Ajayan, 1992).

The arc discharge synthesis can be used to produce both SWNTs and MWNTs. In the synthesis of both single and multi-walled nanotubes, two carbon rods are placed end to end in an inert (He) atmosphere and at a low pressure of 670 mbar (Ebbesen and Ajayan, 1992; Journet et al., 1997). A high temperature discharge of up to 4000 K (Bonard et al., 1998) is produced via a dc current of 100 A driven by a potential difference of approximately 18 V, which then vaporises one of the carbon electrodes (Ebbensen and Ajayan, 1992). Nanotubes are formed during the condensation of the vaporised electrode onto the unvaporised electrode.

During the synthesis of SWNTs, a metal catalyst (Fe, Co or Ni) of approximately 2 at% is placed in powdered form into a hole bored into one of the electrodes (Iijima and Ichihashi, 1993; Bethune et al., 1993). The synthesis of SWMTs may be aided with the addition of methane in the evaporation chamber (Iijima and Ichihashi, 1993).

The MWNT product consists of tubes with external diameters of between 2 to 50nm and internal diameters of approximately 2.2nm (Iijima, 1992). The SWNT product in contrast consists of both single tubes and nanotube bundles. The tubes have diameters of between 0.75nm up to 1.6nm (Iijima and Ichihashi, 1993) and tube bundles of 5 to 20nm consisting of approximately 20 nanotubes (Journet et al., 1997).

As mentioned above, yields of up to 75% have been reported. The tubes obtained by arc-discharge are often coated with amorphous carbon. In the synthesis of SWNTs up to 25% of the product is composed of encapsulated metal particles.

1.5.2 Laser Ablation

Laser ablation was first performed by Guo et al. (1995). In general, a graphite target together with a small amount of transition metal (Ni-Co) (Thess et al., 1996) are vaporised by a laser in an oven at 1200°C filled with an inert gas (He or Ar) at a pressure of 670mbar. This facilitates the formation of a vapour cloud which rapidly condenses on a water-cooled collector located on the outside the oven. During condensation nanotubes are formed on the water-cooled collector.

The inclusion of the transition metal on the graphite target allows the laser ablation technique to produce exclusively SWNTs with yields of >70% relative to the solid carbon source (Thess et al., 1996). The product consists of nanotube bundles or ropes (Figure 1-6) approximately 5 to 20nm in diameter and with lengths of >100μm. The individual nanotubes are bound to each other in a triangular lattice via van der Waals intertube bonding (Thess et al., 1996). The SWNTs found in the ropes have an almost uniform length since termination of the tubes occurs at the end of the rope. The metal catalyst particles can also be found in the product and are covered with amorphous carbon (Thess et al., 1996).

In general SWNTs prepared via laser ablation have greater yields, higher purity and a narrower size distribution than those prepared via arc-discharge synthesis (Daenen et al., 2003).

1.5.3 Catalytic Chemical Vapour Deposition (CVD)

Catalytic carbon vapour deposition has been used to synthesise carbon fibrils for many years (Baker et al., 1972; Rostrup-Nielsen, 1984; de Bokx et al., 1985a; Yang and Chen, 1989) and preceded the documented discovery of carbon nanotubes by Iijima (1991). The first reported use of CVD to produce MWNT was reported by Jose-Yacaman et al. (1992) using a Fe/graphite catalyst at 700°C. The first reported synthesis of SWNTs via CVD was reported by Dai et al. (1996) using a Mo/Al_2O_3 catalyst at 1200°C.

For the synthesis of MWNTs, the CVD process involves the catalytic decomposition of hydrocarbons (e.g. ethylene, acetylene or methane) or CO in a fixed bed and more recently, a fluidized bed reactor (Ivanov et al., 1995; Hernadi et al., 1996; Weizhong et al., 2003). The catalyst used in CVD is usually a supported transition metal with Fe, Co and Ni being the most common ones. The synthesis temperatures range from 550°C up to 800°C (Ivanov et al., 1995).

The synthesis of SWNTs via CVD is performed using two different methods. The first method is similar to the one above where the hydrocarbon or CO in the gas phase is passed over the supported metal catalyst (Dai et al., 1996). Synthesis temperatures range from 700°C up to 1200°C and the synthesis performed at atmospheric pressure (Dai et al., 1996; Mauron et al., 2003). The second method involves the introduction of either the hydrocarbon or CO together with the metal catalyst in the gas phase. Nikolaev et al. (1999) introduced iron pentacarbonyl ($Fe(CO)_5$) together with CO into a continuous-flow gas-phase process. The thermal decomposition of $Fe(CO)_5$ produced iron clusters in the gas phase which

served as nuclei for SWNT synthesis. The synthesis is typically performed at elevated temperatures and pressures of 1200°C and 10atm respectively (Nikolaev et al., 1999) in heated furnace or reactor.

The product of CVD synthesis consists of MWNTs, carbon fibrils (as defined earlier), amorphous carbon and metal particles encapsulated by both amorphous carbon and encapsulated by the tube or fibril itself. In general, MWNTs can range from 2 to 50nm in diameter and up to 50μm in length (Jose-Yacaman et al., 1993). Internal diameters of up to 10nm have also been reported (Hernadi et al., 2000; Avdeeva et al., 2002). The yield with respect to MWNTs is usually reported as grams of carbon per gram of catalyst and hence, yields of up 240 g/g_{cat} have been reported (Avdeeva et al., 1996). The yield of carbon nanotubes relative to impurities such as encapsulated metal particles and amorphous carbon is generally dependent on the synthesis conditions such as temperature (Jose-Yacaman et al., 1993) and hence is subject to great variation. Yields of between 50 to 65% of carbon nanotubes relative to the total carbon produced have been reported (Jose-Yacaman et al., 1993; Ivanov et al., 1995).

In the synthesis of SWNTs via CVD, the product consists of nanotubes, amorphous material and encapsulated metal particles. The tube diameters range from 1nm up to 5nm for the supported catalyst method (Dai et al., 1996) and from 0.7nm to 2nm for the gas phase method (Bladh et al., 2000). Yields of up to 44wt. % SWNTs of the total product have been reported (Nikolaev et al., 1999).

1.5.4 Comparison of Synthesis Techniques

One of the many challenges associated with the synthesis of nanotubes is the purity of the final product. A classic example of this can be seen in the soot of the arc discharge process. The product can contain metal crystallites, encapsulated particles, fullerenes and only about 30 % nanotubes of varying quality (Niyogi et al., 2002). Currently all synthesis techniques for SWNTs produce large amounts

of impurities (Baughman et al., 2002) and this can be extended to MWNTs as well. There is thus a need for the optimization of nanotube synthesis, which favours an increase in the yield of desirable products (morphology) and reduces the amount of waste. Another important challenge associated with carbon nanotube synthesis is the production of large-scale quantities. Commercialisation of carbon nanotubes can only be realised through large-scale production driven by research (Weizhong et al., 2003).

The arc discharge and laser ablation techniques produce nanotubes with an amorphous carbon coating and hence require a large amount of purification in order to obtain a clean nanotube product. The production of nanoropes (Section 1.5.2) by laser ablation limits its application in composite materials because of the loss of surface available for stress transfer (Baughman et al., 2002). Purification in the form of acid treatment can bring in more impurities as well as affect the length and compromise the purity of the sample. Both arc discharge and laser ablation also require operation at high temperature (above 1000°C) with the laser ablation technique being particularly expensive which make it less attractive for large scale industrial synthesis. High purity samples of SWNTs cost as much as $750/g and low purity samples costing as much as $60/g (Baughman et al., 2002). Included in the difficulties associated with these synthesis techniques is the fact that it is difficult to tailor the growth of nanotubes (Kibria et al., 2001). The fact that both laser ablation and arc-discharge synthesis essentially operates as a batch process indicates that scaling up to industrial operation may prove to be difficult.

The CVD process has numerous advantages over the arc discharge and laser ablation methods. There is the ability to tailor the size (external diameter), morphology and length by changing the operating conditions, metal catalyst, carbon source gas as well as the metal crystallite size. The synthesis conditions for MWNTs are moderate in comparison to arc discharge and laser ablation. In terms of the product, MWNTs contain similar impurities such as the amorphous

carbon and encapsulated particles. However, the purity of nanotubes produced by CVD is believed to be sufficient for further applications due to the lack of the carbonaceous impurities on the tubes themselves (Baughman et al., 2002).

In terms of SWNTs, CVD offers the opportunity to grow individual nanotubes rather than nanotube bundles or ropes. Also the SWNTs grown via CVD are found to be free of the amorphous carbon coating found in arc-discharge and laser ablation synthesis (Dai et al., 1996).

Although the yield of carbon nanotubes based on the carbon source in the arc-discharge and laser ablation appear to be greater, the basis for the yield is based on the recovery of the vaporised carbon rod. In CVD, the basis is usually the mass of catalyst itself and the productivity (g/g_{cat}) shows that for 1g of catalyst up to 240g of carbonaceous material can be synthesised (Avdeeva et al., 1996) of which up to 65% can be seen to be carbon nanotubes (Jose-Yacaman et al., 1993). In the case of arc-discharge for example, 4.3g of carbon nanotubes are produced from vaporising a 5.4g carbon rod (Journet et al., 1997). The mass of carbon nanotubes is thus limited by the size of the rod itself and hence limits the applicability of both arc-discharge and laser ablation for large-scale nanotube synthesis. The advantage of the CVD system in the synthesis of carbon nanotubes is that unused carbon source gas can be recycled. This system is most advantageous when applied to the synthesis of carbon nanotubes on an industrial scale.

Multi-walled nanotubes synthesised by via CVD is believed to the most cost-effective way to achieve large-scale industrial synthesis (De Jong and Geus, 2000). Hyperion Catalysis International, Inc. has shown that multi-ton quantities of nanotubes can be produced (Baughman et al., 2002). Large-scale and continuous operation can possibly be realised using a fluidised bed in which both the carbon nanotube product and deactivated catalyst can be removed (Weizhong et al., 2003).

De Jong and Geus (2000) have identified some of the important factors determining the economic feasibility of large-scale synthesis:

- Scale of production
- Feedstock used (carbon source)
- Reactor type and related type of operation
- Yield of carbon fibers with respect to catalytic metal
- Reaction time and temperature

An indication of the growth and interest in carbon nanotubes is that a Japanese company, Mitsui, has announced plans to establish a production facility, which produces 120 ton/year of MWNTs. They plan to produce 20nm diameter nanotubes at $75/kg, which clearly shows that MWNTs are far less expensive to produce than the $60000/kg SWNTs (Baughman et al., 2002).

1.6 Growth mechanism of carbon fibrils and nanotubes

The growth and nucleation of carbon nanotubes and fibers has been thoroughly researched and documented. The actual growth mechanism though is not fully understood.

1.6.1 General Schematic Picture of Growth

The generally accepted mechanism for growth of carbon nanotubes and fibres using CVD is depicted in Figure 1-8. The carbon source gas e.g. methane or ethylene adsorbs onto the exposed metal surface and is subsequently decomposed yielding surface carbon (and surface hydrogen if a hydrocarbon is used as the carbon source). Carbon can diffuse into the bulk of the metal and surface hydrogen will desorb as molecular hydrogen. The carbon atoms then diffuse through the metal and precipitate on the support side of the metal in the

form of graphitic carbon. Furthermore, growth may also occur through surface diffusion of carbon over the metal particle. A characteristic feature of carbon fibril and carbon nanotube synthesis is that the metal particle is found at the tip of the grown fibril or nanotube (see Figure 1-9) and is often encapsulated with layers of carbonaceous material. Therefore, this growth mechanism is often referred to as the tip growth mechanism.

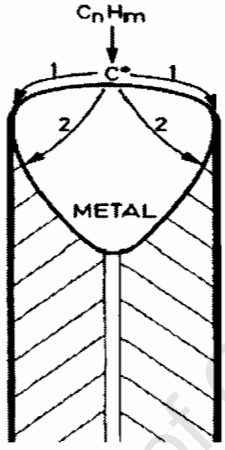

Figure 1- 8. Typical schematic of the growth of carbon fibrils (Hoogenraad, 1995)

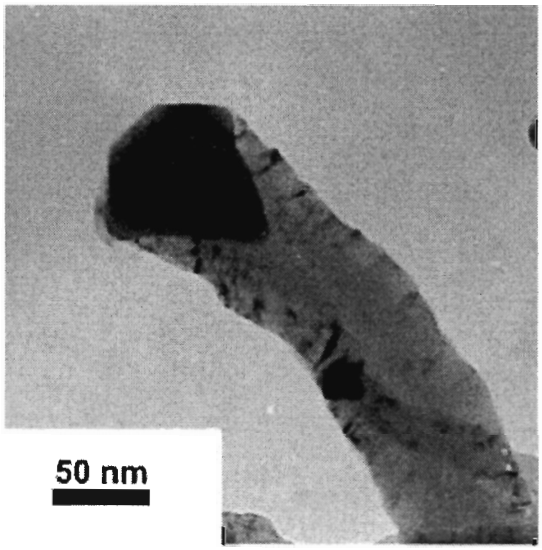

Figure 1- 9. Carbon fibril showing metal particle at its tip (Avdeeva et al., 2002)

Both Hoogenraad (1995) and de Bokx et al. (1985a) believe that metal carbide is an important intermediate in the growth of the carbon fibrils. Hoogenraad (1995) has developed a mechanistic picture for carbon fibrils, which takes into account the encapsulation of the metal particle, the carbide and the fact that the particle is found at the end of the fibril after synthesis. In this mechanistic picture, after carbon has dissolved into the metal, a metal carbide is formed. Due to its instability, it decomposes into the metal and graphite which then totally encapsulates the metal particle. Due to the huge pressure build-up within the encapsulated region, the metal particle is squeezed out exposing a fresh surface for carbon decomposition. Steady-state growth proceeds either via pulsed growth or continuous growth as seen in Figure 1-10.

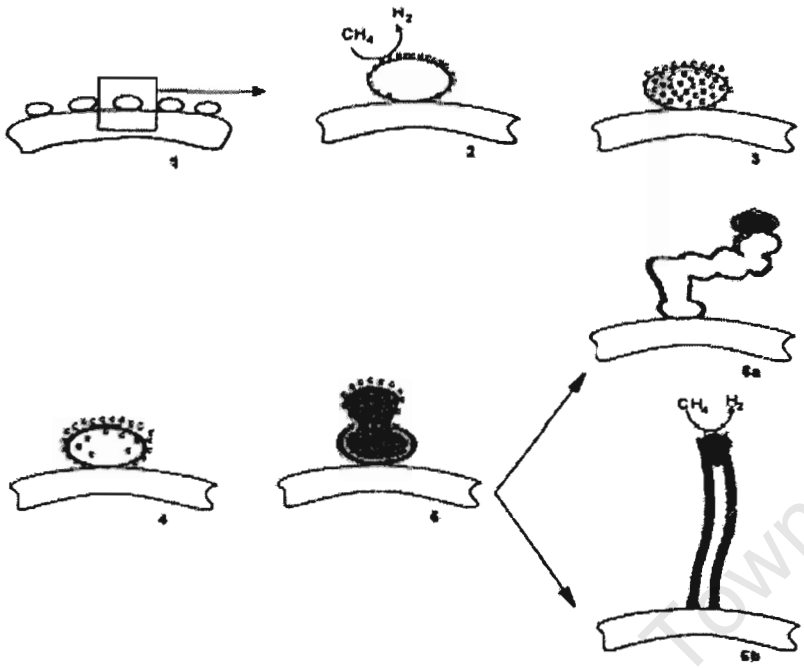

Figure 1- 10. A proposed growth mechanism by Hoogenraad (1995)

In general, the direction of growth of these fibrils or nanotubes is random and this results in interweaving (Figure 1-11). This interweaving is what is responsible for the mechanical strength of fibril or nanotube agglomerates.

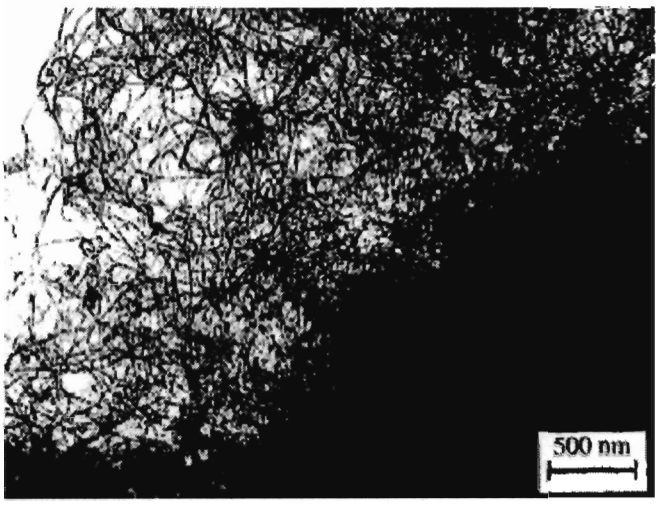

Figure 1- 11. Low magnification of interweaving nanotubes grown over Fe/silica at 700°C (Hernadi et al., 1996)

Because of the greater amount of dissolved carbon on the gas-side of the metal particle than at the support side, a concentration gradient exists over the metal particle. This concentration gradient creates a driving force for carbon diffusion over the metal particle (Snoeck et al., 1997).

The formation of the hollow filament is believed to be dependent of the rates of nucleation, diffusion and the diffusional path lengths within the metal (Snoeck et al., 1997). At low temperature, the rate of nucleation is low relative to the rate of diffusion and the whole metal becomes saturated with carbon (metal/gas and metal/support) before nucleation takes place. This results in full fibrils being formed when the precipitation occurs and the metal is lifted from the support via the tip growth mechanism. At higher temperature the rate of nucleation is almost instantaneous and nucleation of carbon nanotubes occurs as soon as supersaturation occurs at the start of the support/metal interface where the diffusional path lengths are shorter. The whole support/metal interface does not take part in the growth process, as is the case at lower temperature. The metal particle is still lifted from the support but a hollow channel remains. The hollow

channel remains throughout the growth process since no driving force exists for diffusion to occur via longer path lengths (Figure 1-12).

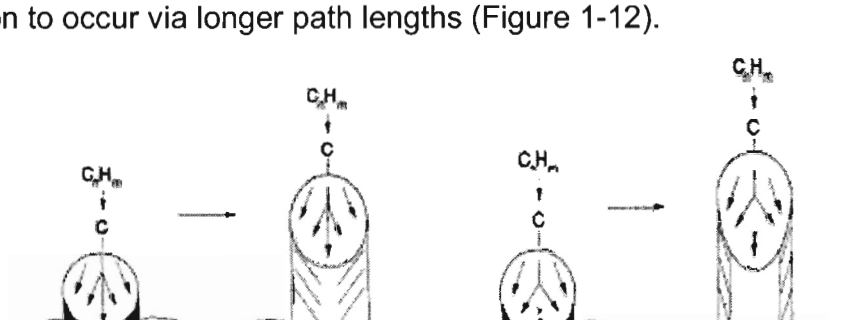

Figure 1- 12. A schematic diagram showing the growth of a fibril (left) where precipitation occurs over entire back of the particle whereas for the growth of a nanotube (right), precipitation only occurs on the gas-metal interface (Snoeck et al., 1997)

1.6.3 The Role of Hydrogen

Under steady-state conditions of growth, there is balance between the dissociation of carbon atoms on the metal surface and the diffusion of the carbon atoms through the metal and the segregation of the carbon into graphitic layers. The carbon concentration at the surface is crucial in maintaining this balance Hoogenraad (1995). Hoogenraad (1995) found that when the carbon concentration was in excess, the metal particles became completely encapsulated. This occurred when CO was fed without H_2. Hydrogen gas co-fed with the CO, serves to hydrogenate the excess carbon atoms at the gas/metal interface, which then lowers the partial pressure of carbon at the surface and prevents complete deactivation and encapsulation of the metal particle.

1.7 Factors Affecting Growth and Morphology of Carbon Nanotubes

1.7.1 The Nature of the Metal Crystallite

Nanotubes with a parallel structure can be grown using iron and cobalt particles (De Jong and Geus, 2000) while nickel particles seem to lend to growth of the fishbone structure. During synthesis of carbon nanotubes of fibrils via nickel particles, it believed that the nickel particle undergoes faceting. The faceting of the particle allows for different crystallographic planes to be either exposed to the carbon containing gas or be responsible for the precipitation of carbon in the form of graphite. This faceting is caused by surface reconstruction (Yang and Chen, 1989). Graphite formation takes place on the epitaxial planes. The epitaxial planes refers to the fact that the structure of the graphitic planes in the nanotube or fibril is directly related to the metal crystallographic planes from which it precipitates. This means that the final shape of the nickel particle should clearly reflect the orientation of the graphitic planes hence the fishbone structure.

With iron particles, the precipitation is far less structure sensitive (De Jong and Geus, 2000) and the graphite layers grow at an angle to the metal surface. Hence parallel fibres or nanotubes can be formed.

As far as metal particle size is concerned, Baker et al. (1972) observed that the fibril diameter was equal to the metal particle at its tip. Thus it is believed that the nanotube diameter can be tailored by tailoring the metal crystallite size. Cheung et al. (2002) showed this hypothesis to be true by using iron nanoclusters on an oxidised silicon support. The carbon nanotubes grown via CVD showed a similar diameter distribution to that of the synthesised iron nanocluster sizes.

In order to achieve the size control of carbon nanotube diameters, there is thus a need for a narrow particle size distribution (De Jong and Geus, 2000; Cheung et

al. 2002) and hence emphasis must be put on the synthesis technique of the metal precursor (De Jong and Geus, 2000).

1.7.2 Effect of Temperature

The synthesis temperature of carbon nanotubes greatly influences the yield, quality and diameter of carbon nanotubes.

1.7.2.1 Yield

Kibria et al. (2002) found that the yield in terms of carbon formation relative to the catalyst mass increased with increasing temperature from 600°C to 700°C on a 20Fe:20Ni:60Al_2O_3 bimetallic catalyst with acetylene as the carbon containing gas. Ermakova et al. (2001) found with Fe/SiO_2 (15wt% SiO_2) and methane as the carbon source that the carbon yield increased with increasing temperature from 660°C up to 700°C where a maximum in the yield was reached and with a further elevation in the synthesis temperature, the carbon yield decreased. A similar trend was found by Li et al. (2002) with iron nanoparticles imbedded in silica and acetylene as the carbon source. It can be seen that in general, the carbon yield increases with an increasing temperature, reaches a maximum and then decreases.

At low temperatures, the catalytic activity is low and accounts for the low yields. Hoogenraad (1995) suggested that for both methane and synthesis gas over Ni/Al_2O_3 that as the synthesis temperature is increased, the rate of dissociative adsorption of the carbon source gas on the catalyst surface increased and hence more carbon atoms were present on the catalyst surface. The growth rate of carbon nanotubes and yield should increase with an increase in temperature provided the increased amount of carbon atoms at the surface can be transported through the metal and incorporated into nanotube growth. Lee et al.

(2001) reported that the growth rate of carbon nanotubes increased from 0.5 to 2nm/min when the synthesis temperature was increased from 750 to 950°C for acetylene over a Fe/SiO_2.

The carbon yield decreases after reaching a maximum because a further increase in temperature results in a further increase in the rate of carbon dissociation on the free surface. Because the rate of diffusion through the metal particle and precipitation as nanotubes can not accommodate this increase of carbon at the surface, the metal particle becomes encapsulated with a shell of carbon and results in a complete loss of activity. With the surface of the metal encapsulated with carbon, there is no access to the carbon source and nanotube growth stops. This loss of activity due to carbon encapsulation becomes more severe with an increase in temperature (Li et al., 2002). This suggests that simply optimising the synthesis temperature can optimise the yield of carbon.

1.7.2.2 Quality

The quality of carbon nanotubes improves with an increase in temperature (Ivanov et al., 1995; Lee et al., 2001; Cheung et al., 2002; Li et al., 2002; Kibria et al., 2002). The graphitic layers of the carbon nanotube appear to be more ordered and are less defective as the synthesis temperature increases (Lee et al., 2001)(see Figure 1-13). Cheung et al. (2002) also found that by increasing the synthesis temperature from 800°C to 900°C that the as-grown carbon nanotubes contained fewer defects in terms of both bends and kinks in the nanotube walls.

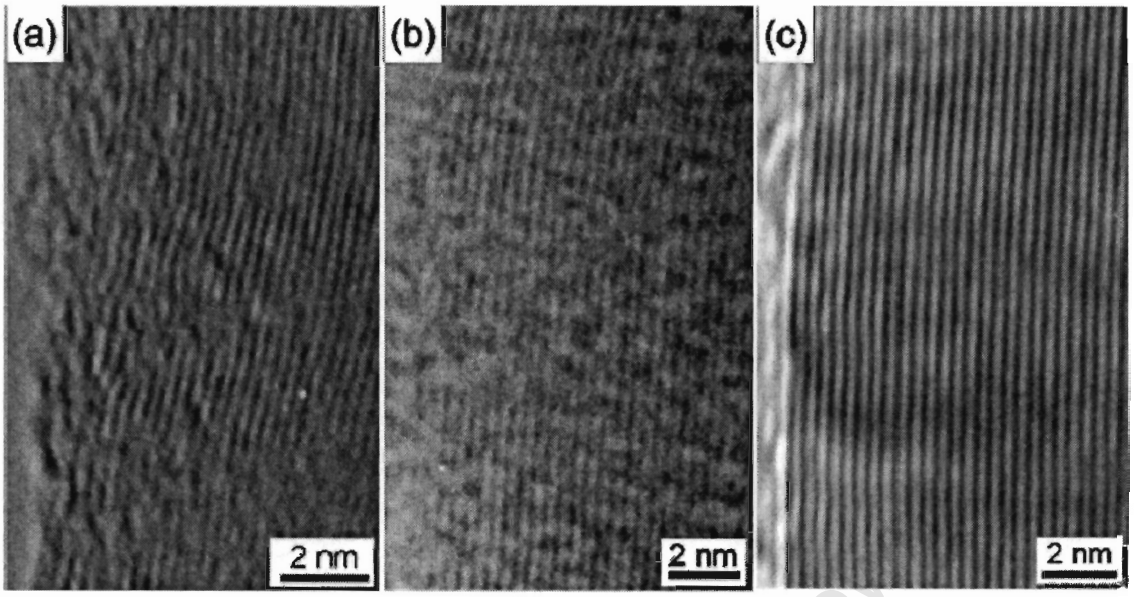

Figure 1- 13. HRTEM images of carbon nanotubes grown at (a) 750°C, (b) 850°C (c) 950°C from Fe/SiO_2 and acetylene as the carbon source (Lee et al., 2001)

The amount of amorphous carbon has been found to also be temperature dependent and increases with increasing temperature (Cheung et al., 2002). This is due to the pyrolysis of the carbon containing gas (Ivanov et al., 1995) at elevated temperatures. The amorphous carbon is usually found deposited on the walls of the carbon nanotubes.

1.7.2.3 Diameter

The synthesis temperature affects the nanotube diameter (Hoogenraad, 1995; Lee et al; 2001; Ducati et al., 2002; Li et al., 2002). The nanotube diameter increases with increasing temperature when acetylene was the carbon source gas. The reason for this increase in nanotube diameter is due to sintering of the metal crystallites (Lee et al., 2001; Li et al., 2002; Ducati et al., 2002). The smaller tube diameters at lower temperature can be ascribed to lower diffusion coefficients and solubility and therefore preferential growth on smaller metal

crystallites will occur. The fact that smaller crystallites are more reactive is due to the increased surface energy and enhances the effect of smaller nanotubes being synthesised at lower temperatures (Ducati et al., 2002; Lee et al., 2001).

Quite contrary to the above findings, Hoogenraad (1995) found that with synthesis gas as the carbon source gas, the diameter decreased with an increase in temperature (Figure 1-13). This was ascribed to the exothermicity of the Boudouard reaction. At low temperature, the partial pressure of carbon on the metal surface is high and only the larger crystallites are able to accommodate this carbon and hence the large crystallites are responsible for large diameter carbon fibrils or nanotubes. The smaller and more reactive crystallites are rapidly encapsulated and hence do not form either nanotubes or fibrils. As the temperature increases, the partial pressure of carbon on the surface of the metal decreases and hence smaller crystallites are active in carbon fibril or nanotube synthesis due to their increased reactivity. The partial pressure of carbon at the surface metal at the elevated temperatures is insufficient for fibril or nanotube growth from the large metal crystallites.

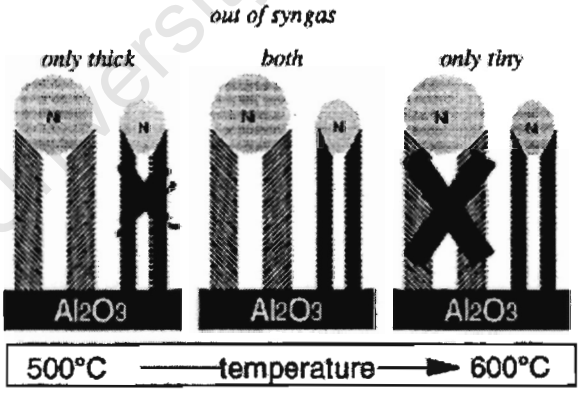

Figure 1- 14. Diagram showing the growth conditions for thick fibrils (left) low temperature and thin fibrils at high temperature (Hoogenraad, 1995)

1.7.3 Carbon Source

The amount of amorphous carbon increases with increasing synthesis temperature as discussed above. It has been suggested that by using a more stable carbon source than e.g. acetylene, a good quality nanotube product can be obtained with increasing temperature while reducing the amount of amorphous carbon formed. Carbon nanotubes are also believed to be good catalysts for amorphous carbon formation especially at elevated temperatures (Hernadi et al., 2000).

The following reactivity series has been found by Hernadi et al. (2000) for various carbon-containing compounds with respect to carbon yield (g/g_{cat}) for 2.5wt% Co/SiO_2:

acetylene > acetone > ethylene > n-pentane > propylene >> methanol = toluene >> methane

It should be pointed out that the same reactivity series was also found by Hernadi et al. (2000) for Fe/SiO_2 with respect to the carbon source gases (acetylene, ethylene, propylene and methane) but showed a product with a lower purity and increased amorphous material was obtained.

From this reactivity series, it was concluded that that acetylene is the most reactive hydrocarbon due to the more reactive triple bond. In general, unsaturated hydrocarbons are more reactive than saturated ones due to the high reactivity of the double bond. Hernadi et al. (2000) believe that unsaturated bonds are required for the bonding of the carbon source to the active site.

The higher reactivity of n-pentane is attributed to the higher dehydrogenation activity. n-Pentane is dehydrogenated to n-pentene, which contains the isolated double bond, which can then bond to the active site. Toluene is found to be

relatively unreactive due the stability of the aromatic ring. Although the unsaturated double bond was seen as a prerequisite for bonding to the active site, Hernadi et al. (2000) believe that the actual formation of an olefin is equally important.

Hernadi et al. (2000) found that the nanotube purity was generally the same for all carbon source gases that showed good activity i.e. acetylene, acetone, ethylene, n-pentane and propylene using Co/SiO_2 as the catalyst. The purity of the product obtained using ethylene and propylene is slightly better due to lower amounts of amorphous carbon being formed. The internal diameter of the carbon nanotubes was found to be 7nm but in the case of ethylene and n-pentane as the carbon source, an internal diameter of 5nm was obtained. The external diameter of carbon nanotubes synthesised using ethylene as the carbon source was found to be 12nm while the average diameter with the other carbon sources was 17nm. They pointed out that the carbon source gas may also need to be taken into account and not just the particle size distribution of the catalyst when trying to synthesise a desired nanotube size.

Cheung et al. (2002) found that by using a less reactive gas i.e. methane as opposed to ethylene for high temperature synthesis (>800°C), the nanotube tube product appeared to have no amorphous carbon coating. From this result it was concluded that both clean and crystalline nanotubes could be grown by optimising the growth conditions together with the choice of carbon source gas.

The yield of carbon nanotubes has been found to be dependent on both the nature of the metal crystallite and the reactivity of the carbon containing gas (Toebes et al., 2002). They found with Ni/SiO_2 that the reactivity of the carbon gas affects the yield of carbon fibres when the Ni crystallites are small (5 to 10nm). Toebes et al. (2002) also found that low reactivity carbon source gases such as CO and CH_4 to be ideal with CO producing the highest yield. This was ascribed to the small crystallites exposing the planes more active for dissociation

of the carbon containing gas. The low reactivity gases enabled steady state growth due to the balance obtained between dissociation on the surface of the metal, diffusion through the metal and precipitation at the support side. When ethylene was used as the carbon source gas, the small crystallites ensured the rapid dissociation of the carbon containing gas, which led to encapsulation and hence rapid deactivation occurred.

1.7.4 Catalyst Support Considerations

The catalytic properties of a supported metal nanotube catalyst were found to be dependent on the metal-support interactions governed by the preparation method of that support (Hernadi et al., 1996; Nagaraju et al., 2002). Hernadi et al. (1996) found that Fe/SiO_2 prepared via ion-adsorption precipitation produced a yield of 4 times that of Fe/SiO_2 prepared via impregnation. The product was also more uniform in terms of nanotube diameter and contained less amorphous carbon.

It can be seen Table 1-2 that when either Co or Fe were supported on alumina prepared via the hydrolysis of aluminium isopropoxide (Al_2O_3(P)) a greater activity and higher yields of carbon nanotubes were obtained compared to a commercial sample of alumina (Al_2O_3(C), corundum alumina)). Similar results were found for Co or Fe on silica where SiO_2(SG) refers to silica prepared by the sol-gel technique and SiO_2(C) refers to a commercial sample (silica-60 Aldrich).

The increased activity on the Al_2O_3(P) support was ascribed to its basicity due to the production of surface hydroxyl groups via the hydrolysis of aluminium isopropoxide. The basicity allowed for the better mixing and a homogenous distribution of the metal on the support surface on the introduction of the metal salt solution. This basicity was not realised on the commercial alumina (Al_2O_3(C)). The sol-gel method used in the preparation of silica (SiO_2(SG)) was also believed to produce a more homogenous distribution of metals on the support.

Table 1- 2. Carbon deposit (%) from acetylene decomposition at 700°C on different metal(s) supported catalysts (adapted from Nagaraju et al., 2002)

Support	Carbon deposit[1] (%)	
	Co	Fe
Al_2O_3(P)	22.2	21.4
Al_2O_3(C)	1.5	1.8
SiO_2(SG)	8.9	8.0
SiO_2(C)	3.0	5.9

1. The carbon deposit is defined as the carbon yield (g/g_{cat}) multiplied by 100.

Zeolite supported Co and Fe catalysts (Co/Y and Fe/Y) prepared by ion exchange were found to be active in carbon nanotube synthesis (Hernadi et al., 2002). The product was well graphitised and crystalline but there was great variation in the diameter. The activity was not as a result of the pore structure of the zeolite but rather due to metals generated from ions located on the outer surface. It was concluded that, in general, only metals situated on the surface of porous supports or in pores large enough to catalyse nanotube formation were responsible for nanotube growth.

Hoogenraad (1995) noted that if the active metal is not properly dispersed on the support, sintering might occur which severely affects the final product. Through sintering the metal catalysts can behave as if there is no support and different and undesirable morphologies can arise through reduced yield and purity (Popov, 2004).

1.8 Proposed Work

Literature has shown that the diameter of the nanotubes corresponds to the metal particle found at the tip of the grown tube and that temperature too can be

used to control the nanotube external diameter. This work aims to control the diameter of the grown carbon nanotube by initially defining the particle size distribution. In order to achieve this, a novel technique will be employed i.e. the water-in-oil micro emulsion or reverse micelle technique (Boutonnet et al., 1982). The advantage of this technique is that it allows for the control of both the size and shape of the particle formed (Boutonnet et al., 1982).

Reverse micelles consist of two immiscible liquids i.e. an oil phase and a water phase, which is stabilised by a surfactant. The oil phase is usually non-polar while the water phase can consist of any polar solvent. The surfactant itself should be soluble in the oil phase but insoluble in the water phase. The non-polar tail of the surfactant is found associated with the oil phase while the polar heads together enclose the water phase (Chang et al., 2000) (Figure 1-15).

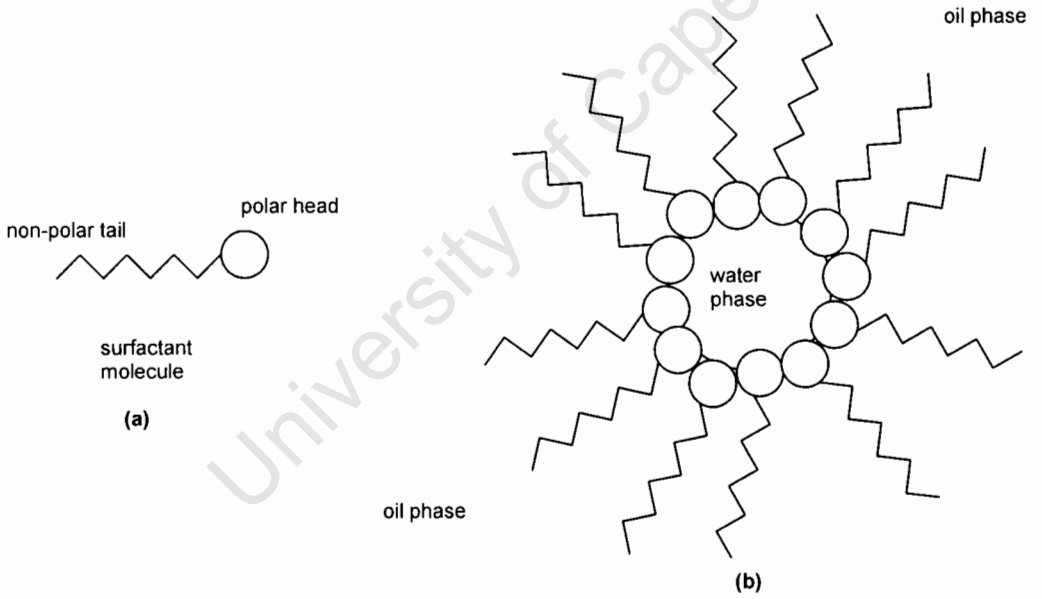

Figure 1- 15. Diagram showing (a) a surfactant molecule and (b) a reverse micelle system.

The formation of nano-sized metal particles using the reverse micelle technique can best be seen in Figure 1-15. In the first reverse micelle mixture, the metal

salt is dissolved in the water phase and in the second mixture, the precipitating agent is dissolved in the water phase. The two reverse micelle mixtures are contacted and the metal nano-particles precipitate. The precipitation itself occurs on the reverse micelle droplet and the size and shape of the particle reflects that of the interior of the droplet itself (Pillai et al., 1995).

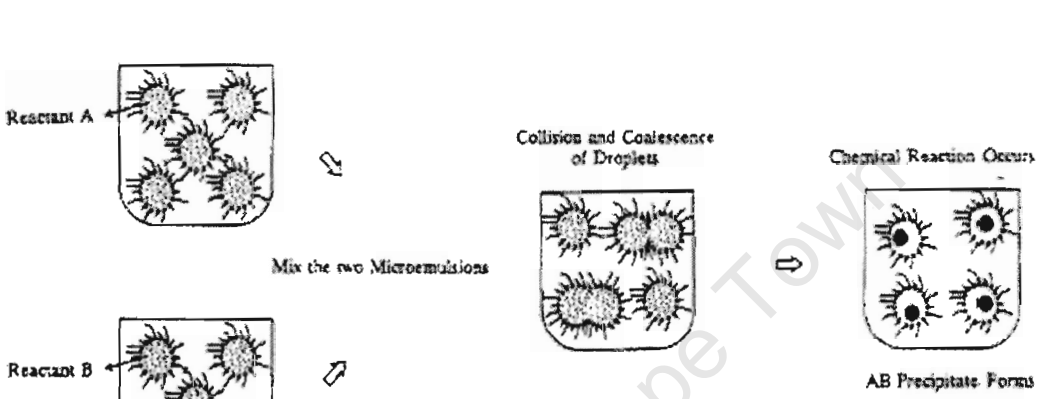

Figure 1- 16. A diagram describing the formation of metal nanoparticles using the reverse micelle technique. Reactant A represents the metal salt in solution and Reactant B is the precipitating agent (Capek, 2004).

The work also aims to investigate how the synthesis temperature affects the diameter of the as grown carbon nanotubes.

CHAPTER 2: EXPERIMENTAL

2.1 Preparation of the Catalysts for Carbon Nanotube Synthesis

Supported iron on alumina catalysts were used for the synthesis of carbon nanotubes. The aim was to synthesise catalysts with different iron crystallite sizes. This would hopefully lead to the synthesis of carbon nanotubes with different diameters related to the size of these iron crystallites. In order to achieve a desired metal crystallite size, the water-in-oil micro-emulsion or reverse micelle technique was employed (Boutonnet et al., 1982). This method was chosen because it allows for control of the metal crystallite size by varying the water to surfactant ratio. The actual procedure used was based on the method by Mabaso (2005) and is summarised in Table 2-1.

The reverse micelle system used consisted of a water phase and an oil phase stabilized by a surfactant. The water phase consisted of either 0.5M $Fe(NO_3)_3.9H_2O$ or 2 M $(NH_4)_2CO_3$ as a precipitating agent dissolved in distilled water. The oil phase consisted of n-hexane (Ar Grade, Kimix) and the surfactant consisted of pentaethylene glycol dodecyl ether (Berol – Akzo Nobel). The amount of each phase required was dependent on the desired crystallite size, which could be increased by increasing the water to surfactant ratio (Mabaso et al. 2005) (see Table 2-1).

Table 2- 1. The amount of the water, oil and surfactant phase required for reverse micelle preparation of supported iron crystallites

Sample Code	Water Phase[1] (g)	Surfactant Phase (Berol) (g)	Oil Phase (n-hexane) (g)	Projected Crystallite Sizes[2] (nm)
WS 5-40	5	40	250	3.0
WS 9-35	9	35	250	7.4
WS 15-50	15	50	250	8.2
WS 15-40	15	40	250	9.0
WS 20-33	20	33	250	17.2

1. Water phase contains either 0.5M $Fe(NO_3)_3.9H_2O$ or 2M $(NH_4)_2CO_3$ in solution in water.
2. Projected crystallites sizes from Mabaso et al. (2005) for the corresponding water to surfactant ratios.

The metal salt solution was prepared by weighing out 50.5g of $Fe(NO_3)_3.9H_2O$ (98.0%, SIGMA) and dissolving it in 250ml deionised water to obtain a concentration of Fe^{3+} ions of 0.5M. The precipitating agent was prepared in a similar manner with a mass of $(NH_4)_2CO_3$ (30-33%, Fluka) of 48.0g required to obtain a concentration of 2M.

In order to have sufficient catalyst for both characterisation and nanotube synthesis, approximately 4g of each catalyst was synthesised with an iron loading of 15 wt.-%. The amounts used in the synthesis assumed that the reverse micelle method is 100% efficient in the precipitation.

The surfactant/oil mixtures were made in duplicate by adding the appropriate amount of Berol to 250g of n-hexane in a 500ml Erlenmeyer flask. The two Erlenmeyer flasks were covered and allowed to stand for 24hrs. Any impurities in the Berol will settle in this period. The mixtures were then filtered. Two reverse micelle mixtures were then prepared by adding the appropriate amount of the

metal salt solution to one flask and the same amount of the precipitating agent to the other flask.

The reverse micelle mixture containing the metal salt was subsequently transferred to a 2L beaker, which was placed in a water bath being maintained at 25°C and stirred at 800rpm. The reverse micelle solution containing the precipitating agent was then rapidly added to the 2L beaker containing the metal salt and the mixture stirred at 800rpm for 1hr. The alumina support (Condea Alumina Puralox SCCa 5-150) was subsequently added and the solution was stirred for a further 5min before adding 1L of acetone (CP Grade, Kimix) still under stirring to solubulise the surfactant. This mixture was stirred for a further 30 min. The mixture was removed from the temperature bath and the metal precipitate allowed to settle together with the alumina support. The clear liquid was then decanted leaving behind a slurry which contained the precipitated metal crystallites and the alumina support.

In order to obtain the desired 4g of catalyst, the above procedure was repeated a number of times. The obtained slurries were combined with the first in a single 2L beaker. The slurry was then cleaned by adding 1.25L of acetone and manually swirling the mixture several times and then allowing the contents to settle. The clear liquid was again decanted and the procedure repeated.

It should be noted that the settling time was dependent on the crystallite size and resulted in the sample with the highest water to surfactant ratio (WS 20-33) settling rapidly within 10min and the sample with a far lower water to surfactant ratio (WS 9-35) taking up to 2hrs to settle. Sample WS 5-40 appeared to remain in suspension and thus a centrifuge was used. Sample WS 5-40 was divided by volume into four plastic containers and placed in a centrifuge (Beckman Avanti J-25) at 10000rpm for 10min at 25°C. The clear liquid was poured off and the remaining slurry containing the metal catalyst and support was again placed into the 2L beaker.

After the cleaning step, 200ml of acetone was added to the 2L beaker. The beaker containing the acetone and catalyst sample was placed in an ultrasonic bath (Ceia CP823) for three 15min intervals at 1.9kW maintained at a temperature of 25°C.

The sample still containing the acetone was then dried in a rotavapor (Buchi Rotavapor R-205) using the following programme for the purpose of slow drying the catalyst sample:

1. P = 400mbar; T = 55°C; t = 45min.
2. P = 250mbar; T = 55°C; t = 45min.
3. P = 100mbar; T = 55°C; t = 45min.

The ultrasonication step and drying step were subsequently repeated in order to achieve a better distribution of the metal on the support.

The obtained sample of approximately 4g was calcined in a glass fluidised bed reactor in synthetic air (Air Liquide) at 230ml (STP)/min whereby the temperature was ramped at a rate of 1°C/min from 30°C up to 300°C and held there for 16hrs. The sample was subsequently allowed to cool to room temperature.

2.2 Carbon Nanotube Synthesis

Carbon nanotubes were synthesised using a cylindrical quartz reactor. A schematic diagram of the experimental setup can be found in Figure 2-1. All gases used for both catalyst reduction and carbon nanotube synthesis were obtained from gas bottles (CO – 99.97%; H_2 – 99.999%; N_2 – 99.999%). All gases were fed using Brooks mass flow controllers, which were calibrated using a wet gas flow meter. Calibration curves corresponding to the various mass flow controllers were then generating from the calibration data and can be found in Appendix A.

Both the reduction and the carbon nanotube synthesis were performed on the same experimental setup under atmospheric pressure.

The experimental programme consisted of three sets of experiments in order to examine the effect of temperature and crystallites size on the yield and quality of carbon nanotubes. The details of the experiments have been summarised in Table 2-2.

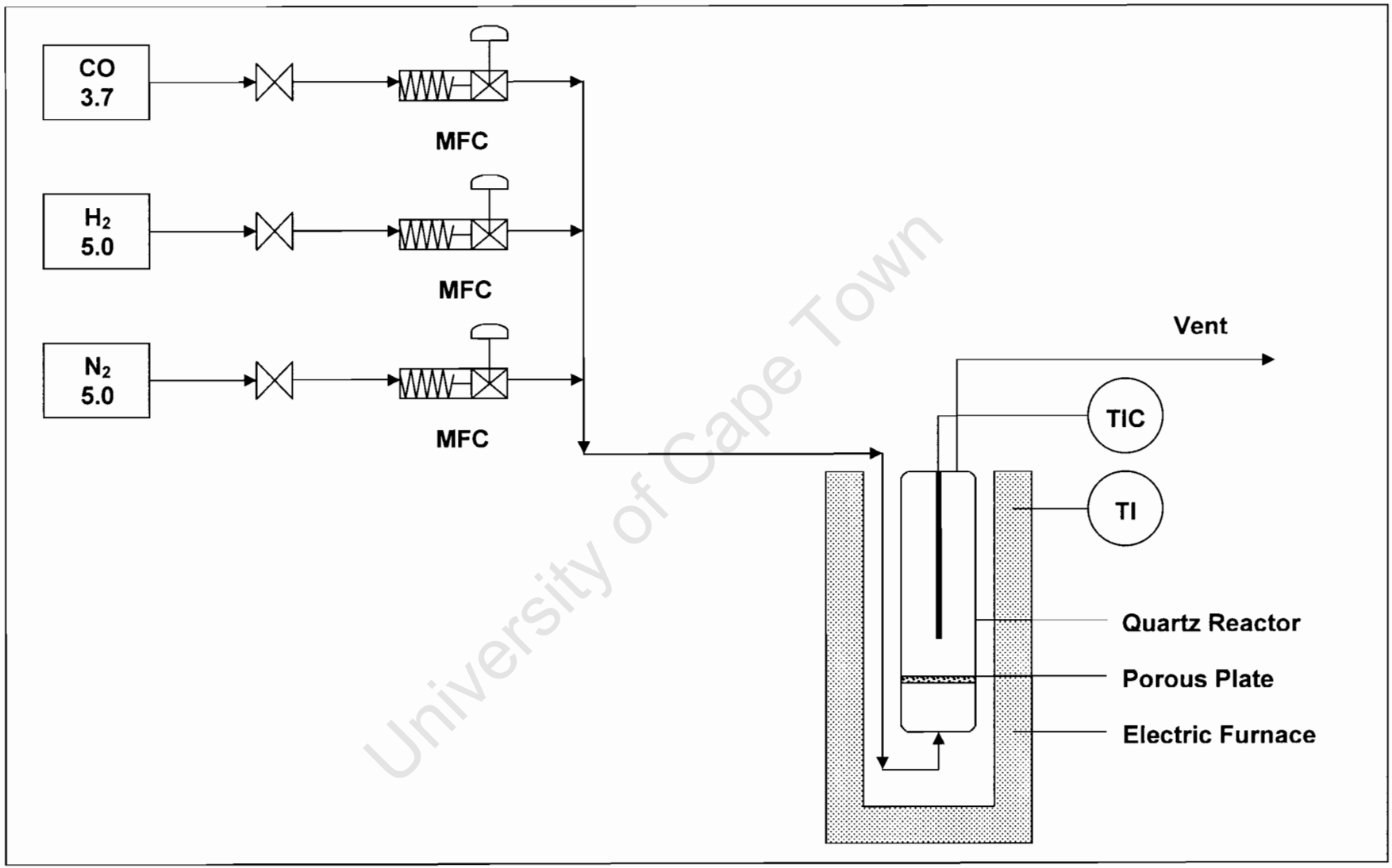

Figure 2- 1. The experimental rig used to reduce the catalyst and synthesise carbon nanotubes.

Table 2- 2. The experimental programme for the synthesis of carbon nanotubes.

	Experiment 1	Experiment 2	Experiment 3
Water to Surfactant Ratios	WS 20-33	All ratios	WS 15-50
Temperature (°C)	520 - 650	560	560 - 650
Sample Size (g)	0.2	0.4	0.4
WHSV ($L(STP)/g_{cat}\cdot min$)	1.9	0.9	0.9
WHSV (mol $CO/g_{cat}\cdot min$)	0.017	0.0083	0.0083
P_{CO} (bar)	0.2	0.2	0.2
P_{H2} (bar)	0.07	0.07	0.07

The mass of the quartz reactor was zeroed and the appropriate amount of catalyst accurately weighed and added. The reactor was then connected to the gas line and placed into the electrically heated furnace. The catalyst sample was subsequently reduced in the reactor in 20% H_2 in N_2 at a space velocity of 1.9L (STP)/$g_{cat}\cdot$min in Experiment 1 and 0.9L (STP)/$g_{cat}\cdot$min in Experiment 2 and 3. The reduction involved heating the catalyst sample at a rate of 2°C/min up to 400°C and maintaining the temperature for 12hrs. After 12hrs, the H_2 flow was stopped and the sample was allowed to reach the synthesis temperature at a rate of 5°C/min under N_2 at 1.5L (STP)/$g_{cat}\cdot$min in Experiment 1 and 0.75L (STP)/$g_{cat}\cdot$min for Experiment 2 and 3.

On reaching the synthesis temperature, the synthesis gas and nitrogen flows were adjusted to 74.5ml (STP)/min CO, 26.1ml (STP)/min H_2 and 272.1ml (STP)/min N_2. This corresponded to 0.017mol $CO/g_{cat}\cdot$min in Experiment 1 and 0.0083 mol $CO/g_{cat}\cdot$min in Experiment 2 and 3. Nanotube synthesis was allowed

to proceed for 7hrs after which the reactor was cooled to room temperature under a flow of N_2 of 140ml (STP)/min. The reactor and its contents were subsequently weighed to determine gravimetrically the amount of carbon nanotubes formed.

2.3 Catalyst and Carbon Nanotube Characterisation

The aims of the catalyst characterisation was to determine the iron loading and hence determine whether the reverse micelle technique was 100% efficient in precipitating all iron in solution as iron crystallites. Catalyst characterisation was also used to measure the obtained crystallite size distribution. In terms of carbon nanotube synthesis, the characterisation techniques were used to determine the morphology and quality of the carbonaceous product.

2.3.1 Titrimetric Analysis of the Catalyst

A catalyst sample of 0.5g was accurately weighed out and recorded and placed in a 100ml Erlenmeyer flask. The sample was then digested by adding 25ml of 6.5N HCl-solution (32%, A.C.E) and heated until boiling for 35min. The sample was quantitively transferred to a 100ml volumetric flask and diluted with distilled water to obtain a 100ml solution. The sample was subsequently filtered since alumina was not digested.

A 5ml aliquot of the digested sample was placed in a 100ml Erlenmeyer flask together with 30ml of a mixture of acids. This acid mixture was prepared by mixing 34.5ml of concentrated H_2SO_4 (98%, Ar grade, A.C.E), 34.5ml of concentrated H_3PO_4 (85%, Merck), 46 ml concentrated HCl (32%, A.C.E) together with 185ml of distilled water.

While still boiling, the sample was removed from the heat source and approximately 4-5 drops of stannous chloride solution was added until the transparent green/yellow colour went completely clear. An additional drop of the stannous chloride solution was then added and the sample allowed to cool for 15min. The stannous chloride solution was prepared by adding 50ml of concentrated (32%) HCl to 50g $SnCl_2$ (98.0%, A.C.E) and heating until all the salt was dissolved. The mixture was allowed to cool and transferred to a 2L beaker diluted with enough distilled water to make a 1L solution.

After cooling, 10ml of mercuric chloride solution was added and a silky white precipitate was observed. The mercuric chloride solution was prepared by adding 50g of $HgCl_2$ (99.8%, A.C.E) to 1L of distilled water and stirring until all the salt had dissolved. Approximately 4 drops of the barium diphenylamine sulphonate indicator was added to the silky white precipitate and the mixture titrated against 0.00149M $K_2Cr_2O_7$ (determined gravimetrically) until a permanent colour change from a green/yellow to an intense purple colour was observed.

The total iron concentration was found using the following equation:

$$Fe = \frac{C_{K_2Cr_2O_7} * V_T * 55.85 * 6}{V_{sol}} \quad (g/l) \qquad (2\text{-}1)$$

In equation 2-1, $C_{K_2Cr_2O_7}$ is the molarity of the indicator, V_T is the titration volume and V_{sol} is the solution aliquot, which in this case is 5ml. The iron content in grams can then be calculated by relating the concentration found in equation 2-1 to the 100ml solution prepared initially.

2.3.2 Atomic Absorption (AA) Spectroscopy

A catalyst sample of 0.1g was accurately weighed and placed in a 250ml Erlenmeyer flask. The sample was then digested by first adding 10ml of an HCl

(30% - CP Grade)/HF (40% - CP Grade) mixture made up of 4 parts HCl and 1 part HF by volume and heating the mixture until boiling. 10ml of HNO_3 (60% - CP Grade) was added and the mixture was allowed to boil until approximately 2ml of the sample volume remained. 5ml of $HClO_4$ (CP Grade) was added to the flask and again allowed to boil until approximately 2ml of the sample volume remained. The sample was subsequently transferred to a 100ml volumetric flask and the remaining volume made up with distilled water. The sample was filtered and the filtrate analysed on the Varian SpectrAA – 30.

From atomic absorption spectroscopy an elemental analysis of the catalyst sample was obtained. More specifically, AA gave the relative amounts of iron and alumina in the catalyst sample as a percentage of the total mass and hence the iron loading could be determined.

2.3.3 X-ray Diffraction (XRD)

X-ray diffraction was used to determine the iron phases present after catalyst calcination and before carbon nanotube synthesis. XRD was also used to obtain the average crystallite size of the various catalyst samples prepared for different water to surfactant ratios.

XRD was performed on a Philips X-ray diffractometer with Cu Kμ as the radiation source with a wavelength of 1.542 Å. In order to determine the iron phases present after calcination, the obtained diffractograms were compared with reference patterns of various iron containing compounds. Examples of the reference patterns used can be found in Appendix B. Elementary line broadening analysis using the Debye-Scherrer equation (2-2) was used to determine the average crystallite size.

$$L = \frac{K\lambda}{\beta_{1/2}\cos(\theta)} \qquad \text{(A)} \qquad \text{(2-2)}$$

In equation 2-2, L is the crystallite diameter; K is taken as 0.9, λ is the wavelength of radiation, $\beta_{1/2}$ is the peak width at half the maximum intensity and θ is the angular position at the peak maximum.

2.3.4 Temperature Programmed Reduction (TPR)

Temperature programmed reduction (TPR) was used to obtain the temperature at which the catalyst sample was completely reduced.

The temperature programmed reduction experiments were performed on a Micromeritics AutoChem 2910. The detachable sample U-tube was first filled with silanised glass wool and the mass of the U-tube and glass wool noted. A catalyst sample of 0.1g was then accurately weighed and added. The U-tube containing the sample and glass wool was then reconnected to the TPR unit and the reduction programme entered into the computer together with the initial sample mass. The sample was reduced with a constant gas flow of 46 ml (STP)/min of 5% H_2/Ar. It should be noted that during TPR, 5% H_2/Ar was used but in the reduction of the catalyst before carbon nanotube synthesis, 20% H_2/N_2 was used. The difference in the hydrogen concentration may lead to an enhanced reducibility.

The temperature was ramped at a rate of 10°C/min from 30°C up to 120°C under a flow of Ar. The temperature was held at 120°C for 30min so that all water was properly removed from the sample. The sample was allowed to cool to room temperature (ca. 30°C) under a flow of argon. The gas was switched to 5% H_2/Ar and the sample heated at a rate of 10°C/min from 30°C up to 900°C. The temperature was held at 900°C for 30min. The sample was then allowed to cool to room temperature under a flow of argon.

2.3.5 Transmission Electron Microscopy (TEM)

Transmission electron microscopy was used to determine the particle size distribution of the catalyst sample. In terms of the carbon nanotube synthesis, TEM was used to characterise the nanotubes in terms of both the external and internal diameters in order to obtain a distribution. Transmission electron microscopy was also used to characterise the nanotubes in terms of their general shape and morphology.

The catalyst or carbon nanotube sample was placed in a small plastic vial and approximately 5ml of methanol (99%, Merck) was added. The vial was then placed in an ultrasonic cleaner (Branson, SmithKline Company) for 1min and a drop of the finely dispersed liquid placed on a carbon coated copper grid. This was allowed to dry overnight. The images were taken on a LEO EM912 (120kV) electron microscope and a Philips CM200. The images were analysed using a public domain image processing software package called ImageJ (v1.32j).

2.3.6 Scanning Electron Microscopy

Scanning electron microscopy was also used to characterise both the catalyst and carbon nanotube samples. In terms of the catalyst, SEM was used to characterise the catalyst in terms of its surface topology. In terms of the characterising the carbon nanotube samples, SEM was used to observe the morphology and shape of carbon nanotube bundles. To this end, a Leica S440 scanning microscope and a JEOL JSM-6000F scanning microscope were used.

For the Leica S440 scanning microscope, an aluminium stub was first coated with a water-based carbon glue. The sample was then placed on the stub and subsequently covered with a thin film of carbon using an evaporation coater. For the JEOL JSM-6000F, the same procedure used by Prinsloo (2000) was employed.

CHAPTER 3: RESULTS

3.1 Determination of Iron Content

The intended iron loading was kept constant so that the effect of the crystallite size and temperature alone could be observed. An intended loading of 15 wt.-% was chosen so that the active metal phase was well distributed on the alumina support with the hope that minimal sintering at the high synthesis temperatures of between 520 and 650°C would occur. The intended loading was calculated during the reverse micelle synthesis by assuming the process was 100% efficient. By knowing both the concentration of iron in solution and the volume added, the mass of iron could easily be calculated by assuming 100% efficiency.

The iron loading was determined using two different methods namely titrimetric analysis and atomic absorption spectroscopy (AA). The results obtained from these methods can be seen in Table 3-1 and Figure 3-1 respectively.

Table 3- 1. Metal loading for different characterisation techniques together with the intended loading in calcined catalysts.

Sample ID	Desired Loading (wt% Fe)	Titrimetric Analysis (wt% Fe)	Atomic Absorption (wt% Fe)
WS 5-40	15	8.2	8.7
WS 9-35	15	7.5	8.1
WS 15-50	15	13.6	10.5
WS 15-40	15	6.9	6.7
WS 20-33	15	11.0	9.2

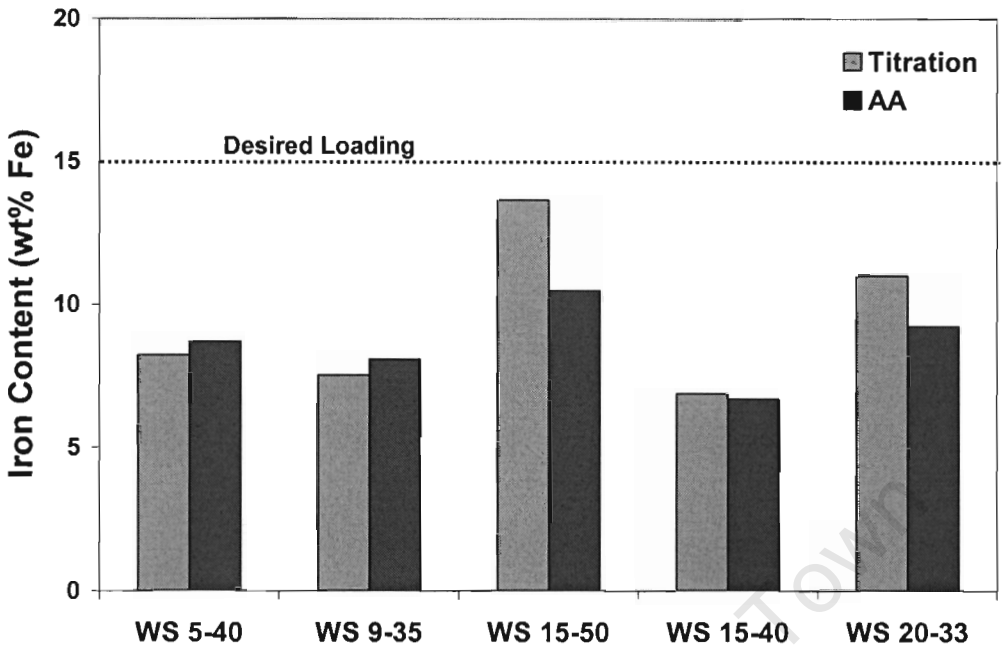

Figure 3- 1. A comparison of the iron loading using different characterisation techniques for catalysts prepared using different water to surfactant ratios. The dashed line represents the intended loading of 15 wt.-% iron.

From Figure 3-1 and Table 3-1, it is clear that there is general agreement in the iron loading between the two different characterisation techniques. In samples WS 15-50 and WS 20-33 however, the difference in loading is >1.5% between titration and AA. The difference in the iron loading between these two samples suggests that an experimental error may exist either in the AA or titrimetric analysis.

It is clearly evident from both Figure 3-1 and Table 3-1 that the intended loading of 15 wt.-% was not achieved in any of the catalyst samples prepared irrespective of the water to surfactant ratios.

The results of all characterisation techniques strongly suggest that the reverse micelle technique is in fact not 100% efficient in the precipitation of iron in solution as iron oxide crystallites. This could account for the difference in the intended and the obtained loading. It is not necessarily stated that the inefficiency of the reverse micelle technique is in the precipitation step. Precipitated iron may also have been lost during the extensive cleaning procedure used to remove the surfactant. The weak anchorage of the iron on the support could also have been disturbed during the calcination in the fluidised bed where iron oxide nano-particles could have been blown out of the reactor. The apparent higher loading in sample WS 15-50 may have been attributed to insufficient alumina being added to produce the desired loading.

Due to the general similarities in the iron loading between the titrimetric analysis and AA, the recorded loading will be taken as an average of the loading obtained from the aforementioned characterisation techniques (Table 3-2).

Table 3- 2. Loading of the prepared catalyst sample taken as an average of the loading from titration and AA results.

Sample ID	Average Loading (wt% Fe)
WS 5-40	8.5 ± 0.4
WS 9-35	7.8 ± 0.4
WS 15-50	12.1 ± 2.2
WS 15-40	6.8 ± 0.1
WS 20-33	10.1 ± 1.3

3.2 Temperature Programmed Reduction

Temperature programmed reduction was performed to characterise the reduction behaviour of prepared catalyst samples.

3.2.1 Reduction Profiles

The temperature programmed reduction of Fe_2O_3 is believed proceed via the following reaction scheme (Kock et al., 1985):

$$3Fe_2O_3 + H_2 \Leftrightarrow 2Fe_3O_4 + H_2O \quad (3\text{-}1)$$

$$Fe_3O_4 + H_2 \Leftrightarrow 3FeO + H_2O \quad (3\text{-}2)$$

$$FeO + H_2 \Leftrightarrow Fe + H_2O \quad (3\text{-}3)$$

$$Fe_3O_4 + 4H_2 \Leftrightarrow 3\alpha - Fe + 4H_2O \quad (3\text{-}4)$$

Hematite (Fe_2O_3) is believed to firstly reduce to magnetite (Fe_3O_4), then to wustite (FeO) and finally α-Fe. Wustite is thermodynamically unstable and is generally not seen in the reduction profile. The reduction of hematite is thus seen as a two-step process, which occurs via the reactions 3-1 and 3-4.

In a typical reduction profile of hematite, the 1st peak is associated with equation 3-1 and should correspond to 11.1% of the total consumption of H_2 required for complete reduction (Brown et al., 1982). The 2nd peak is then associated with the reduction of magnetite to α-Fe. The results of the TPR performed can be found in Figure 3-2 and Table 3-3.

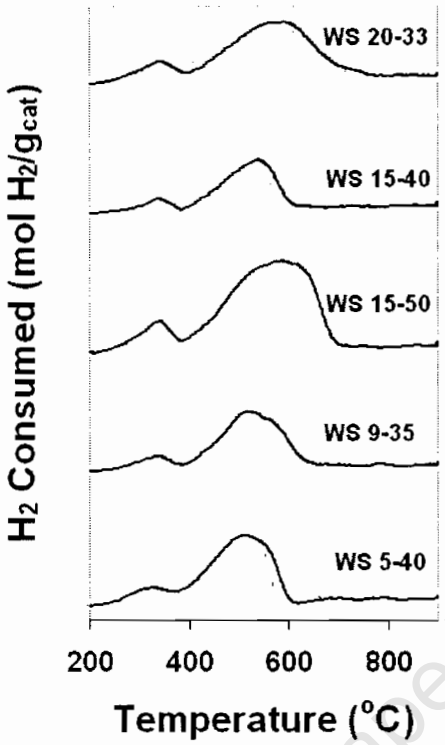

Figure 3- 2. Temperature programmed reduction profiles for the catalyst samples with different water to surfactant ratios. The TPR was performed in 5% H_2/Ar at a flow rate of 46 ml (STP)/min.

Table 3- 3. Quantitative analysis of the TPR data generated for catalyst samples with different water to surfactant ratios.

Sample	% of Total H_2 consumed in 1st Peak	% of Total H_2 consumed in 2nd Peak	Ratio H_2 consumed/Fe (mol/mol)
WS 5-40	18.7	81.3	1.68
WS 9-35	11.0	89.0	1.43
WS 15-50	10.8	89.2	1.79
WS 15-40	13.2	86.8	1.24
WS 20-33	9.9	90.1	1.39

The temperature programmed reduction profiles show two reduction peaks for all water to surfactant ratios. The start of the first reduction peak, which corresponds to the reduction of Fe_2O_3 to Fe_3O_4, is found at approximately 207°C and the start

of second peak, which corresponds to the reduction of Fe_3O_4 to α-Fe, occurs at 360°C. On average, the 1st peak maximum was found to be at approximately 320°C and the second at 520°C.

The first peak maximum in the reduction profile is found to be at least 20°C less and for the 2nd peak maximum, at least 80°C less than those reported by Hughes and Newman (1987) for unsupported Fe_2O_3 and by Bukur and Sivaraj (2002) for alumina supported Fe_2O_3. This could be attributed to the small crystallite sizes, which have been synthesised via the reverse micelle technique. These smaller crystallites with their higher surface area per unit volume might be responsible for the onset of reduction at lower temperatures.

The 2nd peak maximum in the reduction profile of sample WS 15-50 (Figure 3-2) is distinctly broader and larger than other catalyst samples. Since the iron loading can be directly related to the hydrogen consumption and the hydrogen consumption to the area under the TPR profile, a larger and broader peak represents a larger loading. This confirms the results obtained from both titrimetric analysis and AA.

No high temperature peaks were present beyond the second reduction peak for all water to surfactant ratios, which indicated that strong support-metal interactions were not present. Despite this, the identification of high temperature peaks would have proved difficult due to the high signal to noise ratio encountered at the elevated temperatures (>700°C) which may have masked such peaks. Strong support-metal interaction is not expected by the catalyst synthesis technique applied because the metal oxide precursor was already precipitated before the alumina support was added. Any interaction between the support and metal oxide precursor is expected to be of a weak van der Waals nature.

In Table 3-3, the average H_2 consumption associated with the 1st peak with respect to the total H_2 consumption was found to be 11.2% for the samples WS 9-35, 15-50, 15-40 and 20-33. This is in agreement with the expected 11.1% for complete reduction of Fe_2O_3 to Fe_3O_4. Sample WS 5-40 showed a H_2 consumption of the 18.7%. This result could be attributed to the lack of resolution in peaks as seen in Figure 3-2. It also has been hypothesised by Bukur and Sivaraj (2002) that a larger than the 11.1% 1st peak may be attributed to some hematite being directly reduced to α-Fe.

If all iron is present as hematite then the following equation should represent the reduction of hematite to alpha iron:

$$Fe_2O_3 + 3H_2 \rightarrow 2Fe + 3H_2O \quad (3\text{-}5)$$

This equation indicates the molar ratio of hydrogen consumed to iron should be 1.5. In Table 3-3, a great variation in the molar ratio can be seen. In samples WS 9-35, 15-40 and 20-33, the molar ratios are lower than 1.5, which could indicate that all iron is not present as hematite. This could indicate that some iron is present as magnetite although this was not seen in XRD (section 3.2.2). In the case of ratios greater than 1.5, the increased consumption could be attributed to the surfactant which may not have been properly removed during the cleaning regime implemented. The great deviation in the ratio could also be attributed to uncertainty in the iron content determination.

3.2 Particle Size Distribution and Iron Phase Determination

The particle size distribution was of particular importance to the study because one of the aims of the study was to identify the relationship between the external nanotube diameter and the diameter of the metal crystallite.

3.2.1 TEM and SEM Images of the Metal Catalyst

TEM and SEM images were taken of the calcined catalysts with different water to surfactant ratios to observe the shape and morphology of the iron crystallites and their distribution on the alumina support. The TEM images can be seen in Figure 3-3 to Figure 3-7. TEM was also used to generate particle size distributions for the various catalyst samples. In measuring the size of the aforementioned crystallites, the iron crystallites were assumed to be spherical.

It is clear from many of the TEM images that there was no clear contrast between the iron oxide crystallites and the alumina support. This made both the determination and measurement of the iron oxide crystallite sizes difficult. This proved particularly problematic at the lower water to surfactant ratios i.e. WS 5-40 and WS 9-35. An attempt was made to overcome this problem by first taking images of blank alumina and then comparing these to the images of iron oxide on alumina. This was done so that the basic shape and morphology of alumina could be used as a reference when trying to identify the iron oxide crystallites. The characterisation of the catalyst still proved difficult because the overlap of alumina crystallites appeared to resemble iron oxide crystallites. This can clearly be seen in Figure 3-3.

A similar issue concerning the lack of contrast between iron and the γ-alumina support when using TEM as the characterisation technique was encountered by Kock et al. (1985). This lack of contrast was attributed to the well crystallised γ-alumina support. The support produces an extensive diffraction contrasts in TEM compared to that of iron and hence can completely dominate the image.

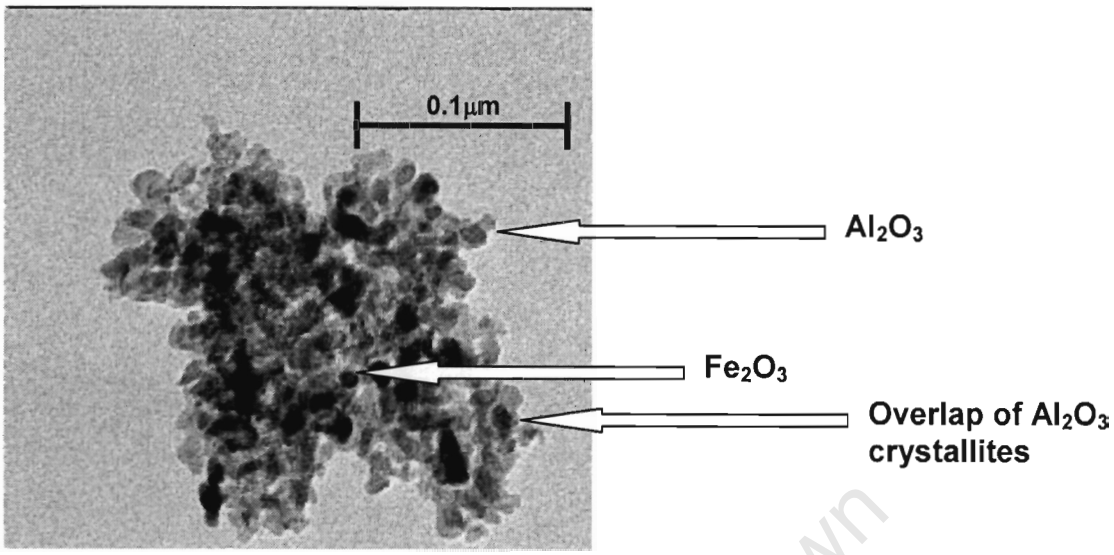

Figure 3- 3. A TEM image of sample WS 20-33 showing both the catalyst and support together with overlap of support crystallites which can be mistaken for a Fe_2O_3 crystallite.

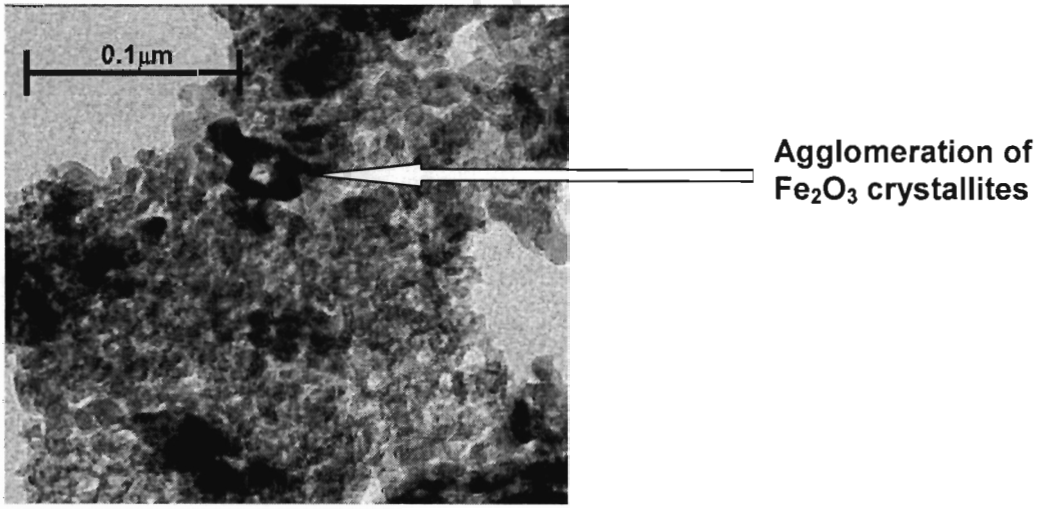

Figure 3- 4. A TEM image of sample WS 15-40 showing the agglomeration of Fe_2O_3 crystallites.

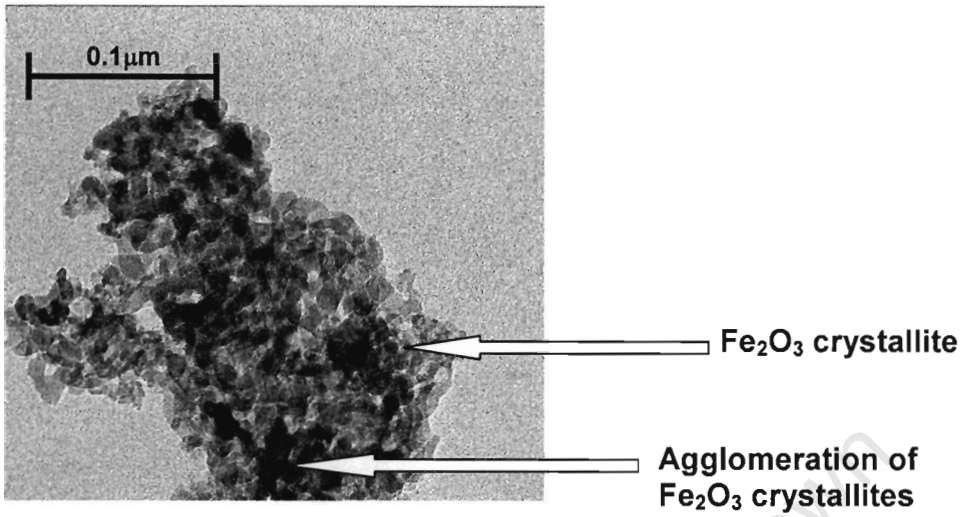

Figure 3- 5. A TEM image of sample WS 15-50 showing the difficulty in identifying single Fe_2O_3 crystallites.

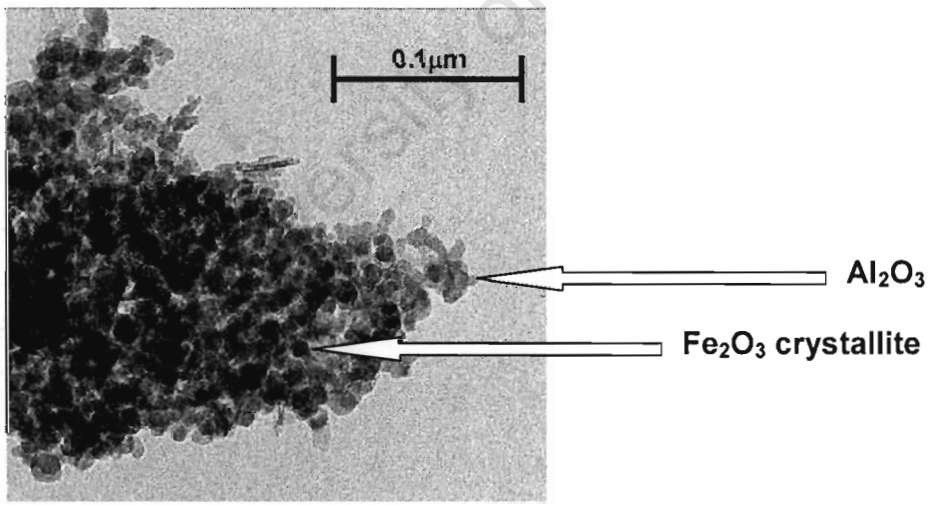

Figure 3- 6. A TEM image of sample WS 9-35 indicating both Fe_2O_3 and Al_2O_3 crystallites. The dense agglomeration of the crystallites should be noted together with the apparent smaller crystallite size.

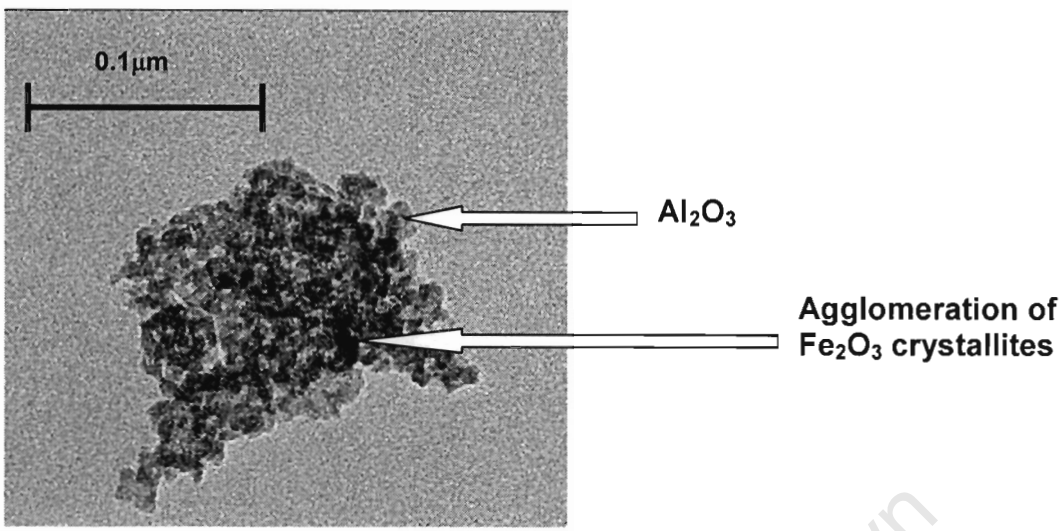

Figure 3- 7. A TEM image of sample WS 5-40. It should be noted that the Fe_2O_3 crystallites could not be clearly identified.

A reduction in iron crystallite size is not clearly apparent from the TEM images in Figure 3-3 to Figure 3-7. In sample WS 20-33 (Figure 3-3), the Fe_2O_3 crystallites could be identified but in sample WS 5-40 (Figure 3-7), single Fe_2O_3 crystallites could not identified with enough certainty so as to generate a particle size distribution. It was concluded that the crystallites in WS 5-40 were too small to be identified and therefore that result suggested that the reverse micelle technique had successfully generated small crystallites. As mentioned before, the difficulty in identification was also enhanced by the agglomeration of the Fe_2O_3 crystallites on the support and hence the lack of distribution of the metal on the support. This suggests that the ultrasonic steps had not achieved the intended distribution of the metal on the catalyst support. The particle size distributions generated from the TEM images can be seen in Figure 3-8 and are summarized in Table 3-4.

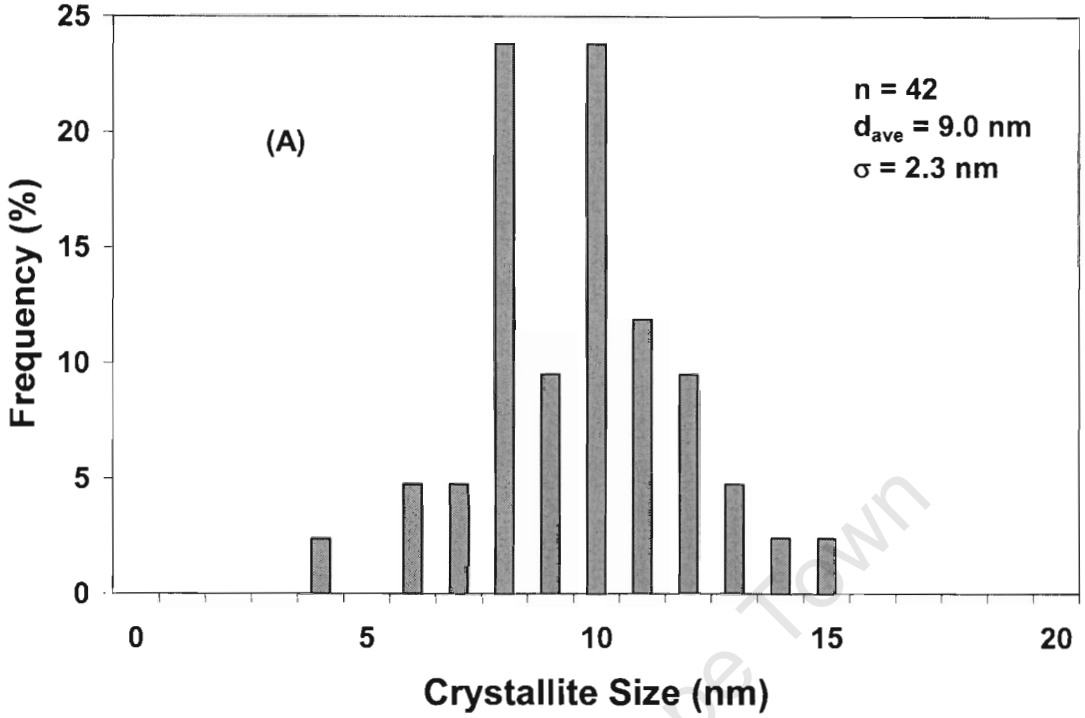

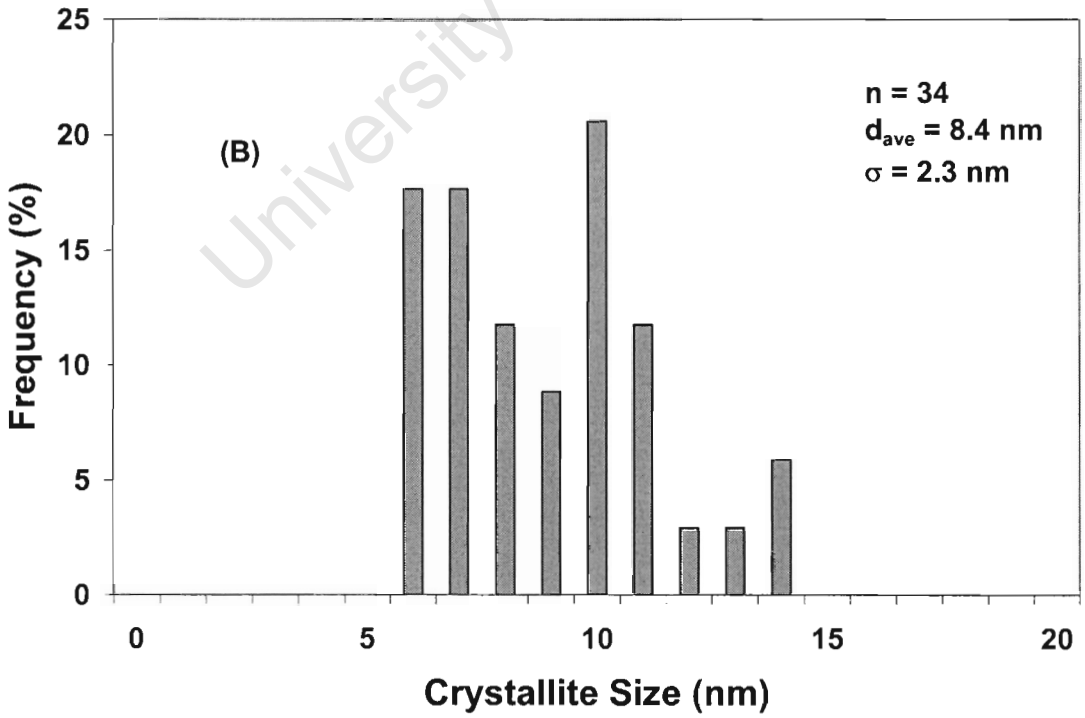

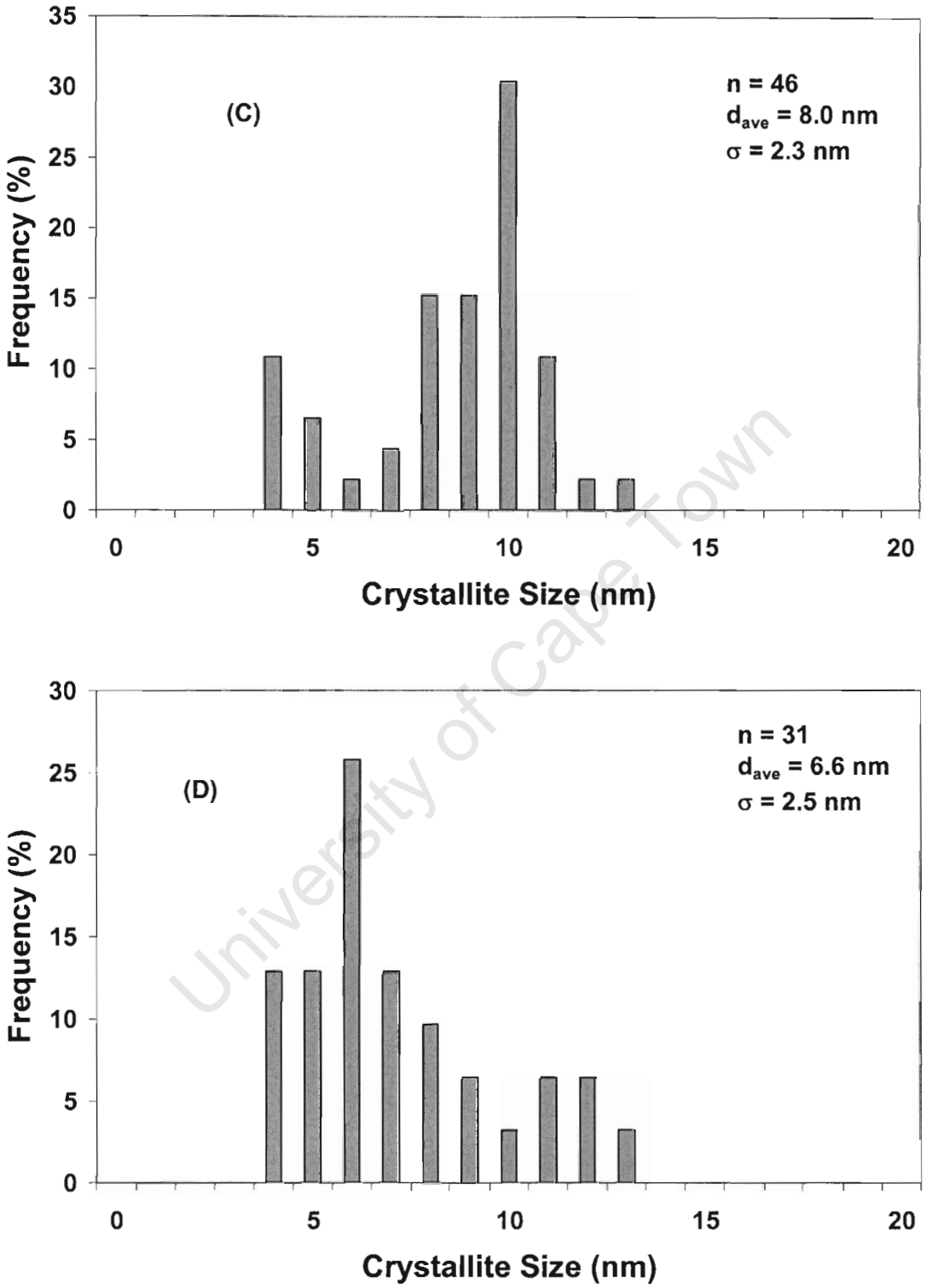

Figure 3- 8. Particle size distribution of the metal catalyst for samples (A) WS 20-33, (B) WS 15-40, (C) WS 15-50 and (D) WS 9-35.

Table 3- 4. Average crystallites sizes for different crystallite samples generated from the particle size distributions.

Sample ID	Average Crystallite Size (nm)	σ (nm)	n
WS 9-35	6.6	2.5	31
WS 15-50	8.0	2.3	46
WS 15-40	8.4	2.3	34
WS 20-33	9.0	2.3	42

The results in Figure 3-8 and Table 3-4 show that in general, the reverse micelle technique was able to produce crystallites in the nanometre range. The results do show however that there is a general decrease in the crystallite size from sample WS 9-35 to sample WS 20-33. It should be stressed again that as the crystallite size decreased, it become more difficult to identify individual iron crystallites as indicated by the greater standard deviation in sample WS 9-35. As mentioned before, the crystallite sizes in sample WS 5-40 could not be identified with certainty and as such no particle size distribution could be generated. Attention should also be drawn to the sample sizes seen in Table 3-4 identified as n. The sample sizes are relatively small and this confirms the difficulty in both finding and measuring the iron crystallites.

Although the sample sizes were small when generating a particle size distribution, an indication of the crystallite size was the settling time of the iron precipitate after synthesis and during the cleaning procedure. As noted before sample WS 20-33 settled very quickly within 15min with the settling time increasing with a decrease in the water to surfactant ratio. Sample WS 5-40 remained in suspension and required a centrifugation step. The apparent increase in settling time with a decrease in water to surfactant ratio does confirm the general trend observed with respect to the particle size distribution.

The results in Table 3-4 do indicate that nanometre crystallites were synthesised with an appreciable difference between samples. This would hopefully allow the crystallite size effect to be realised during the synthesis of carbon nanotubes.

The TEM images above also show that the Fe_2O_3 crystallites were not well distributed on the Al_2O_3 support. The Fe_2O_3 crystallites tended to form agglomerates, which made the identification of single crystallites difficult as mentioned above. This could be due to the use of the ultrasonic steps, which instead of breaking the agglomerates might have been responsible for forcing the Fe_2O_3 crystallites into the Al_2O_3 pores. The weak van der Waals interaction between the iron and the alumina support may have easily been disrupted during the ultrasonic cleaning steps allowing the metal to either find its way into the pores or simply leaving the support altogether. These results were confirmed by the SEM images seen in Figure 3-9 and Figure 3-10.

From Figure 3-9 the dark grey and spherical particles were found to be Al_2O_3 and the brighter and more irregular particles were found to be Fe_2O_3. This result was confirmed by the EDS function available on the SEM unit. A particle as described earlier is defined as a collection of crystallites. It is evident from Figure 3-9 that some Fe_2O_3 is well distributed on the Al_2O_3 support identified by the small bright specks found on the spherical Al_2O_3 support. It should be mentioned however that the bright specks are not iron crystallites at the magnification represented above but rather smaller agglomerates of Fe_2O_3 crystallites. It is also evident that some Fe_2O_3 particles are found to be separate from the support altogether. This is probably due to both the weak interactions and the ultrasonic steps as mentioned above.

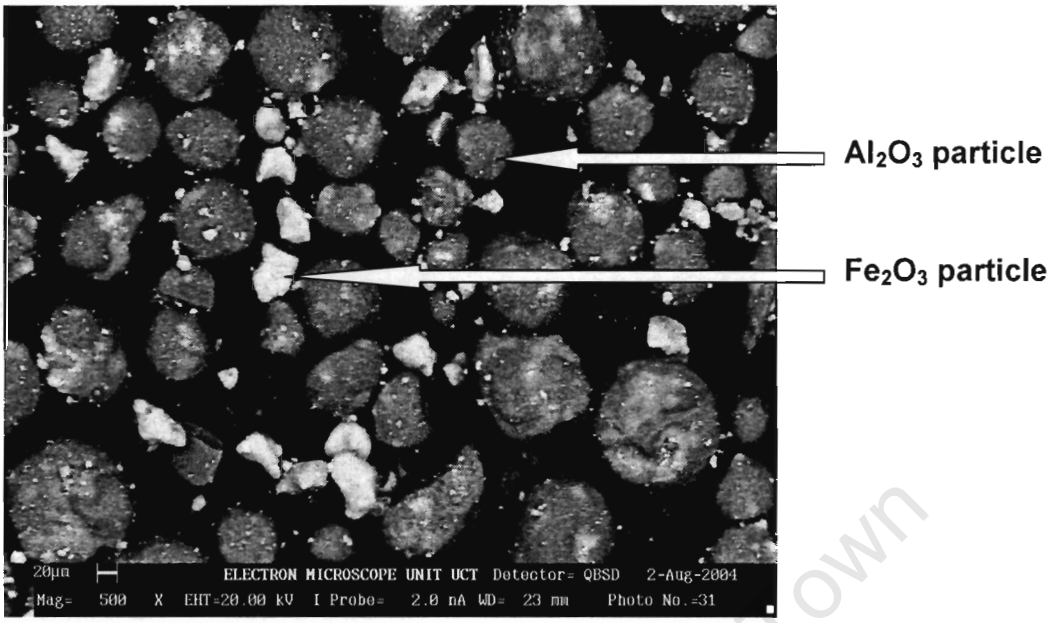

Figure 3- 9. SEM image of sample WS 9-35.

In Figure 3-10 the agglomeration of the Fe_2O_3 crystallites on the Al_2O_3 support is clearly seen. This is highlighted by 1 and 2 on the SEM image. The image clearly shows the dense agglomeration on the supported identified by the white patches on the darker spherical support. This also contributes to the difficulty in the identification of the individual Fe_2O_3 crystallites in the TEM images shown above.

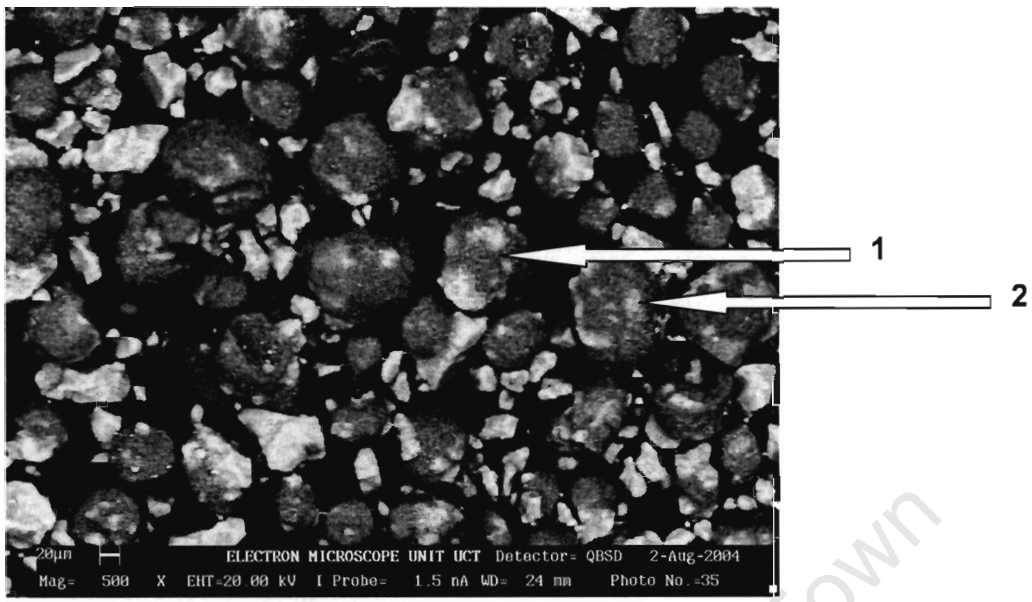

Figure 3- 10. SEM image of sample WS 20-33.

3.2.2 X-Ray Diffraction

X-ray diffraction was used to determine the iron phase present after catalyst calcination. It was also used to quantitatively determine the diameter of the iron crystallites, which could be used as a method of validation and comparison with the crystallite size obtained from TEM measurements. An XRD spectrum for sample WS 9-35 can be seen in Figure 3-11.

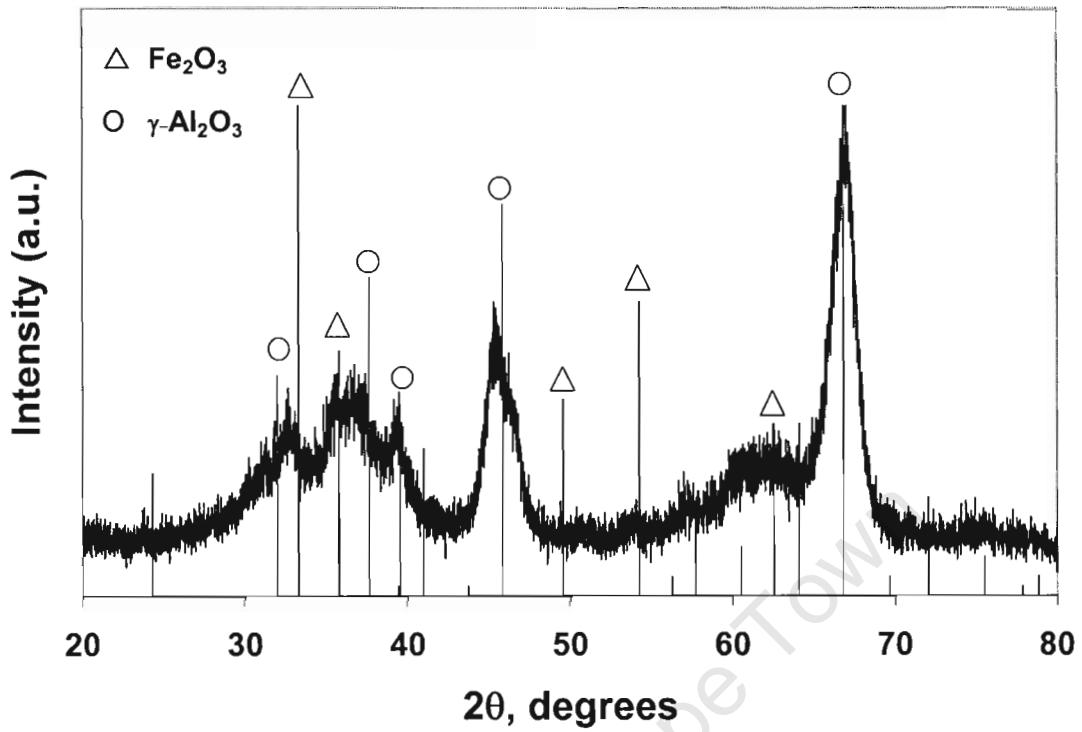

Figure 3- 11. X-ray diffraction pattern of sample WS 9-35 after calcination.

It can clearly be seen in Figure 3-11, that two alumina peaks are clearly identifiable at $2\theta = 45.8^{o}$ and 62.8^{o} while it is difficult to identify prominent hematite peaks especially between $30^{o}>2\theta>40^{o}$ due to their close proximity to the alumina peaks in that same interval. At this stage it was believed that due to the apparent low loading, hematite peaks may not have been identifiable. This phenomenon at low iron loading was seen in the work of Takenaka et al. (2004), where it appeared that crystallites sizes could not be determined for Fe_2O_3/Al_2O_3 at loadings as low as 7 wt % iron due to the lack of resolution between the hematite and alumina peaks. However, on increasing the loading, the hematite peaks were easily observed and hence crystallite diameters could be easily calculated.

In order to identify the hematite peaks, X-ray diffraction was performed on the interval between $30^{o}>2\theta>40^{o}$ to see if the prominent hematite peak at $2\theta = 33.3^{o}$

could be observed and used to calculate the crystallite diameter. The results can be seen in Figure 3-12.

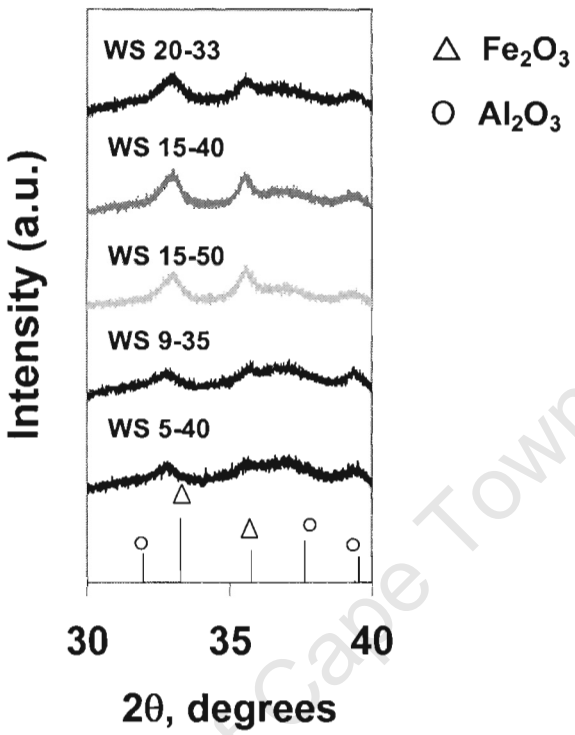

Figure 3- 12. X-ray diffraction patterns for different water to surfactant ratios.

The results in Figure 3-12 show that as the water to surfactant ratio increased, so the resolution of the peaks increased as well. This is clearly seen in the difference between sample WS 9-35 and WS 15-50. The diffraction peak at $2\theta = 33.3$ was used to estimate the crystallite diameter using the Debye-Scherrer equation (peak width at half the height of the chosen diffraction peak) and the results are given in Table 3-5. The results do suggest that there was definitely a size difference between the samples with different water to surfactant ratios. These results show a similar trend to those found via TEM where there was a definite size increase in the crystallite size from WS 5-40 up to WS 20-33.

Table 3- 5. Average crystallite diameters obtained from the peak line broadening in XRD by the Debye-Scherrer equation.

Sample ID	Crystallite Size (nm)
WS 5-40	6.1
WS 9-35	7.4
WS 15-50	9.0
WS 15-40	9.0
WS 20-33	9.6

3.3 Characterisation of Carbon Nanotubes

3.3.1 Analysis of the Carbonaceous Product Synthesised at Different Temperatures

The productivity of the carbon nanotubes was determined gravimetrically by weighing the catalyst sample before and after carbon nanotube synthesis and normalising it with respect to the catalyst mass and the time of synthesis. Included in the mass gain due to carbon formation was the additional mass lost due to oxygen removal from hematite during the reduction step (see Appendix C). However, the mass loss due to reduction of the supported iron catalyst is minimal and does not affect the reported productivity significantly.

It can be seen (Figure 3-13) that the productivity increases rapidly from 0.08gC/g_{cat}.hr at 520°C up to 0.42gC/g_{cat}.hr at 560°C where a maximum productivity is observed. This indicates an increase in productivity of 590% over a 40°C temperature increase. A further increase in temperature results in a steep decrease in the productivity from 560 to 630°C and a subsequent levelling off of the productivity to a level of 0.025gC/g_{cat}.hr up to 650°C. A similar trend has been previously observed (Li et al., 2002; Ermakova et al., 2001) with respect to productivity. It suggests that the yield is a strong function of temperature and that an optimum temperature exists for certain productivity.

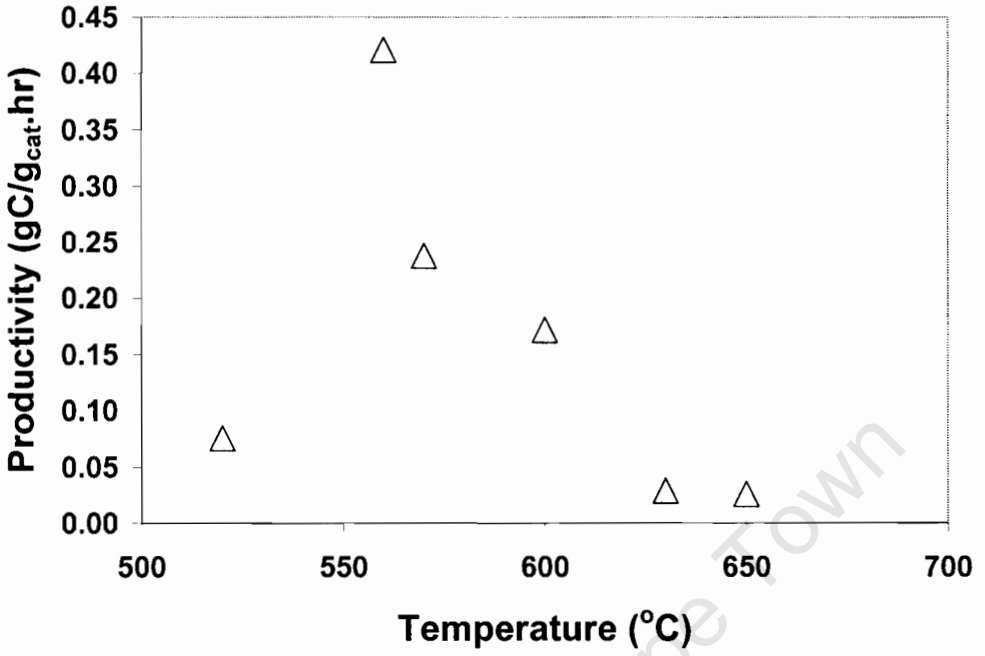

Figure 3- 13. Productivity of carbon nanotubes as a function of synthesis temperature for the sample WS 20-33. Experimental conditions: WHSV = 1.9 L (STP)/g_{cat}.min

Some additional insight can be gained with respect to the morphology of carbonaceous product by observing the TEM images (Figure 3-14 to 3-22). It appears that at low temperature both thick fibrils with an external diameter of 110nm as well as carbon nanotubes with diameter of 13nm are grown (Figure 3-14 and 3-15 and Table 3-6). The low standard deviation in the external diameter of the carbon nanotubes (6nm), the lowest encountered in all external diameter measurements, indicates the uniformity of the narrow diameter nanotubes at this temperature. This result differs from that of Hoogenraad (1995) at low temperature who reported an absence of carbon nanotubes with a narrow external diameter.

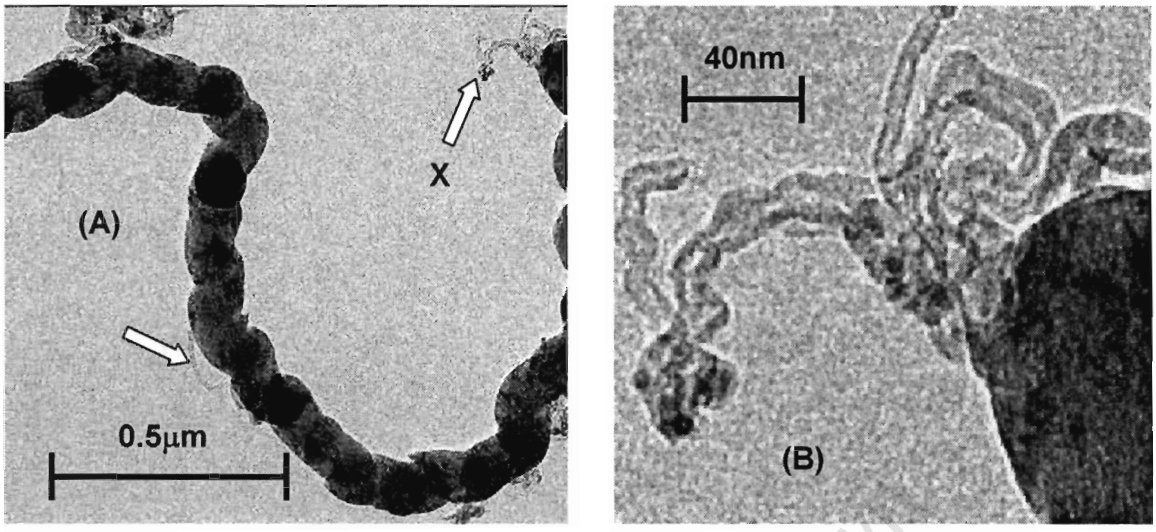

Figure 3- 14. TEM images of (A) a carbon fibril and (B) an enlargement of region marked as X showing the presence of nanotubes grown at 520°C with sample WS 20-33.

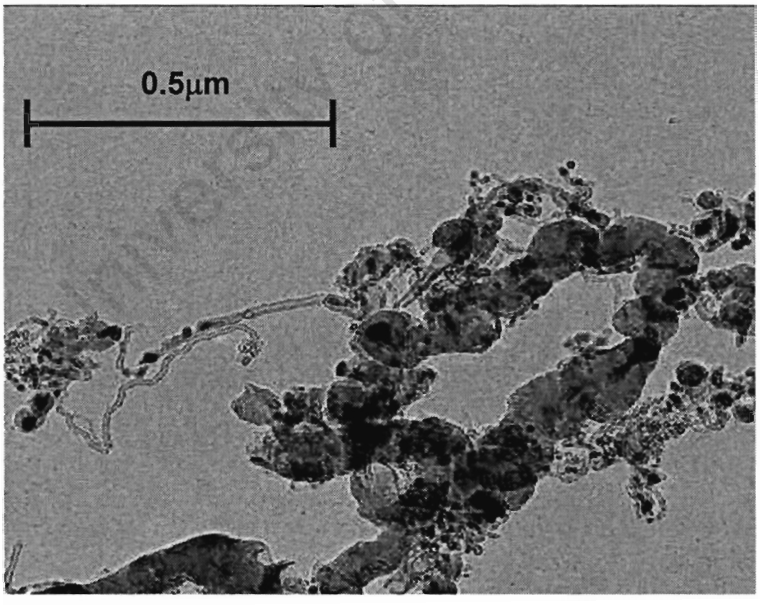

Figure 3- 15. A TEM image of both carbon nanotubes and a thick carbon fibril grown at 520°C with sample WS 20-33.

Table 3- 6. Carbon fibrils and carbon nanotube diameters for sample WS 20-33 grown at different synthesis temperatures.

			Carbon Nanotubes				
Temperature (°C)	Fibril Diameter (nm)	σ_F (nm)	External Diameter (nm)	σ_{Ext} (nm)	Internal Diameter (nm)	σ_{Int} (nm)	n
520	110	16	13	6	4	2	37
560	N/A	N/A	37	18	7	3	33
600	188	59	30	12	11	5	30
630	N/A	N/A	13	5	7	3	48
650	N/A	N/A	13	5	7	3	52

As the temperature increases, a complete disappearance of carbon fibrils occurs and all carbon deposited forms carbon nanotubes with a resulting increase in the nanotube diameter from 13nm at 520°C to 37nm at 560°C. With a further increase in temperature above 560°C and up to 650°C, the carbon nanotube diameter decreases to an almost uniform value of 13nm and this is the same value as that synthesised at 520°C. The presence of fibrils was not expected in the product at 600°C. At the higher synthesis temperatures of 630°C and 650°C, the carbon nanotubes were composed of both straight tubes and bamboo-like tubes (Ermakova et al., 2001) (Figure 3-18A and B) with the internal channel closed with a parabolic-shaped carbon layer. For the purposes of this study both morphologies were regarded as nanotubes as they were both encountered at 630 and 650°C.

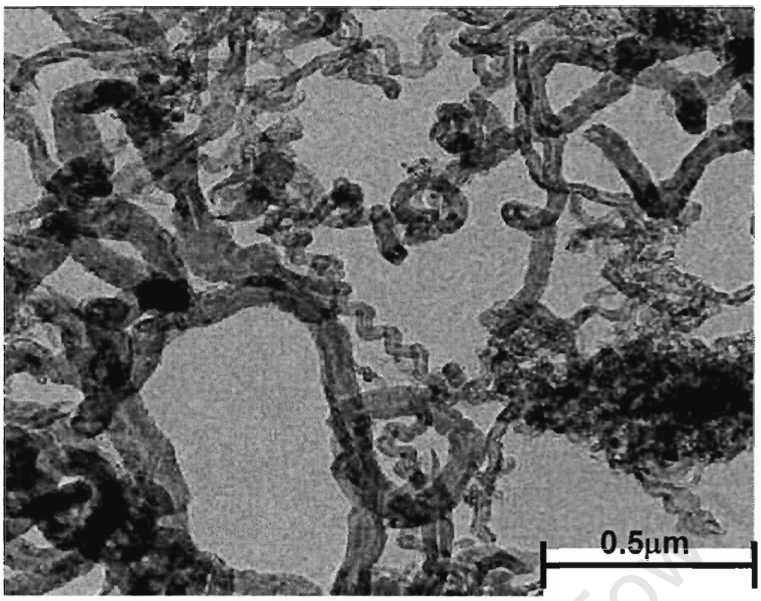

Figure 3- 16. A TEM image of the carbon nanotubes grown from sample WS 20-33 at 560°C.

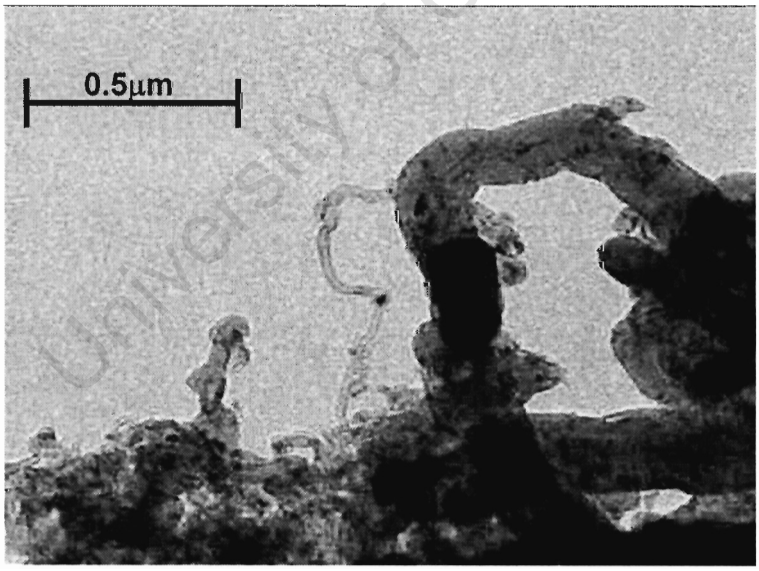

Figure 3- 17. A TEM image of carbon nanotubes and carbon fibrils growth from sample WS 20-33 at 600°C.

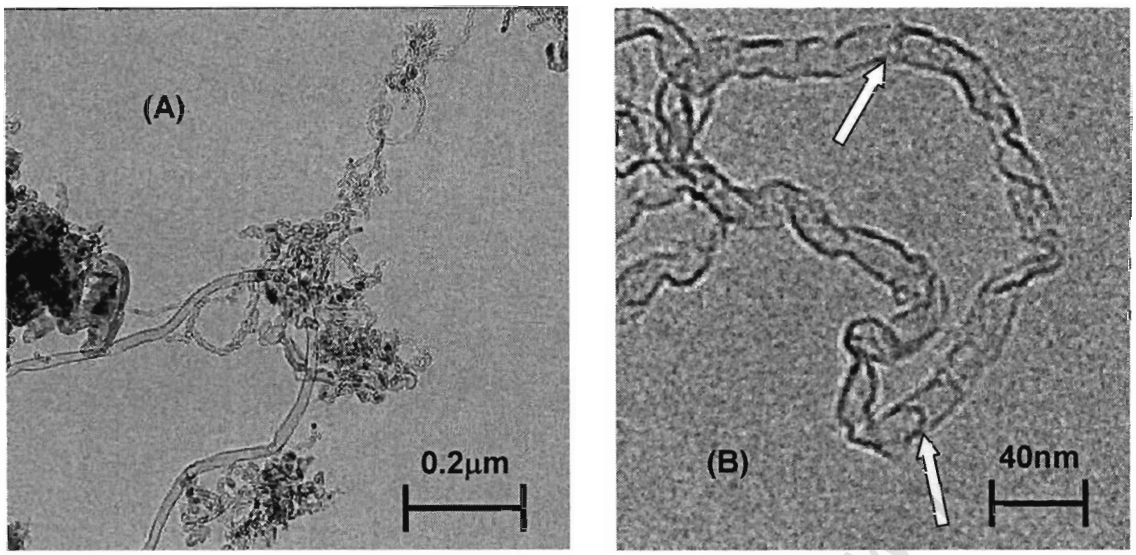

Figure 3- 18. TEM images of (A) carbon nanotubes grown from sample WS 20-33 and (B) showing the bamboo-like formation at 630°C.

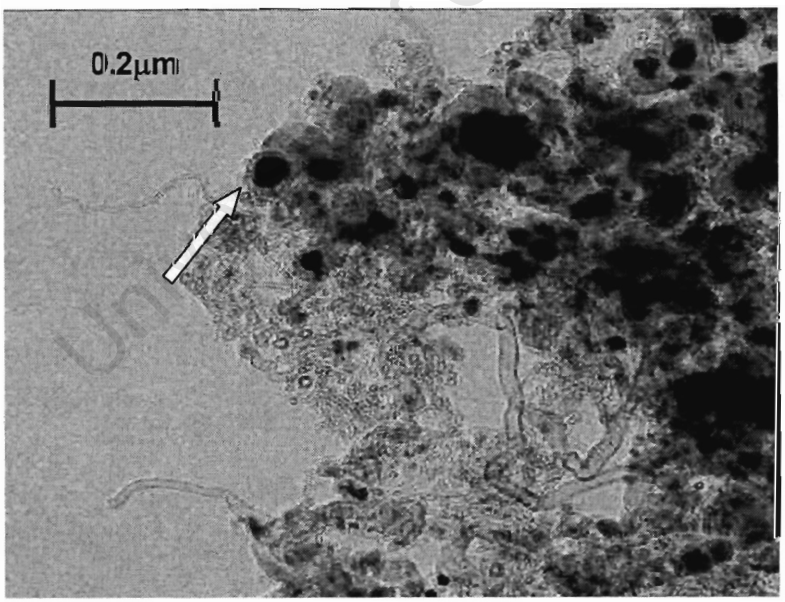

Figure 3- 19. A TEM image of carbon nanotubes synthesised at 630°C showing not only the prevalence of narrow diameter nanotubes but also large encapsulated metal particles (white arrow head).

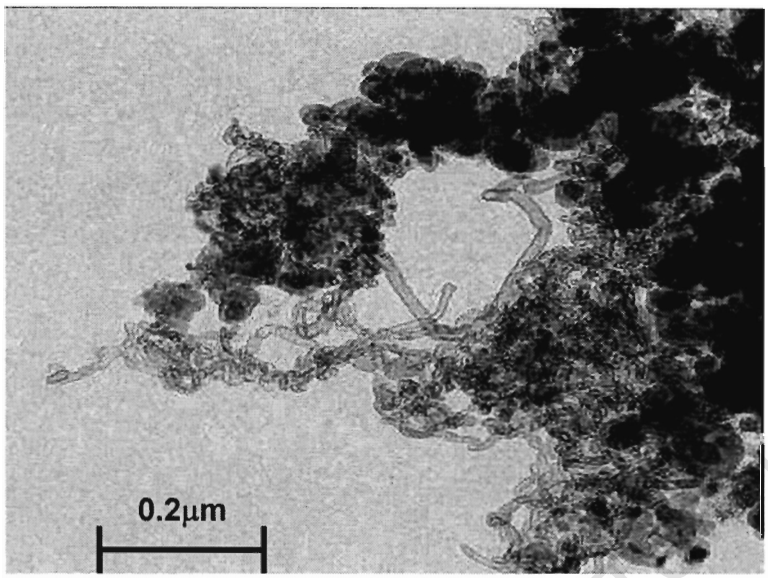

Figure 3- 20. A TEM image of the showing both the carbon nanotubes and the metal particles encapsulated with carbon at 650°C grown from sample WS 20-33.

There was no obvious trend observed for the internal diameter of the as-grown carbon nanotubes. The lowest synthesis temperature of 520°C produced the smallest internal diameter. The internal diameter at 560, 630 and 650°C are all approximately 7nm while at 600°C, the internal diameter was found to be 11nm. Again, the sample synthesised at 600°C produced results which tended to differ either from those expected i.e. with respect to the formation of fibrils at elevated temperatures or produced results which were different from other samples.

Another important feature observed with the increase in temperature is the formation of large amounts of encapsulated metal particles with an increase in synthesis temperature (Figure 3-19 and 3-20). These metal particles are covered with a carbonaceous deposit and were clearly not involved in nanotube growth. These encapsulated particles ranged from 18nm up to 46nm at 650°C, which is

larger than the average nanotube diameters observed at that synthesis temperature. These results do suggest that a certain crystallite size is active at a specific temperature.

The decrease in the standard deviation of the external diameters from 560 to 650°C suggests that the nanotubes grown become more uniform in diameter and could suggest improved quality of the sample with an increase in temperature as previously reported (Ivanov et al., 1995; Li et al., 2002; Kibria et al., 2002). Of course, this result can only be confirmed with the use of HRTEM where the actual orientation of the lattice planes can be observed.

The results above seem to suggest that in order to control the diameter of carbon nanotubes; the synthesis temperature itself needs to be optimised with respect to the nanotube external diameter rather than the crystallite size. This result is confirmed by the fact that there is no relation between the carbon nanotube diameter at any growth temperature and sample WS 20-33 which was found to have an average diameter of between 9 and 9.6nm (Table 3-4 and Table 3-5).

In a similar experiment, carbon nanotubes were grown at 560°C and 650°C but from sample WS 15-50 (with average crystallite size of 8.5nm) and the WHSV was decreased to 0.9L (STP)/g_{cat}·min. Despite the reduction in WHSV, similar results were obtained and can be seen in Figure 3-21 and 3-22 as well as Table 3-7.

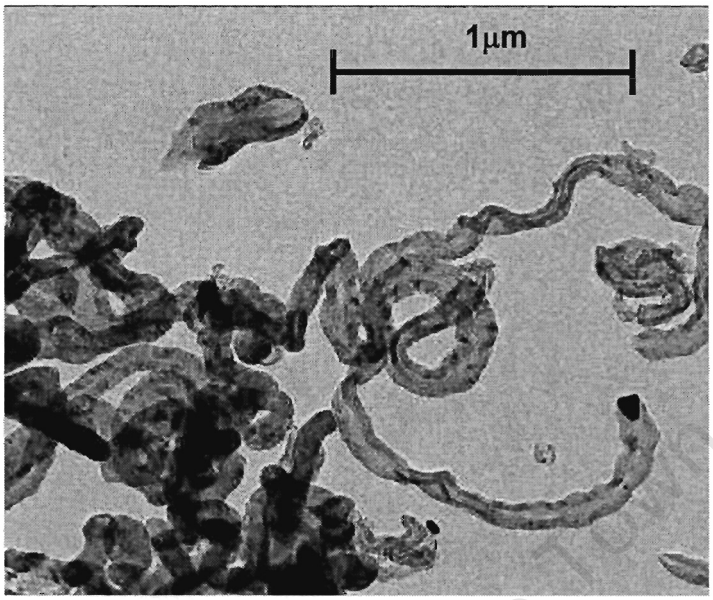

Figure 3- 21. A TEM image of carbon nanotubes grown from sample WS 15-50 at 560°C.

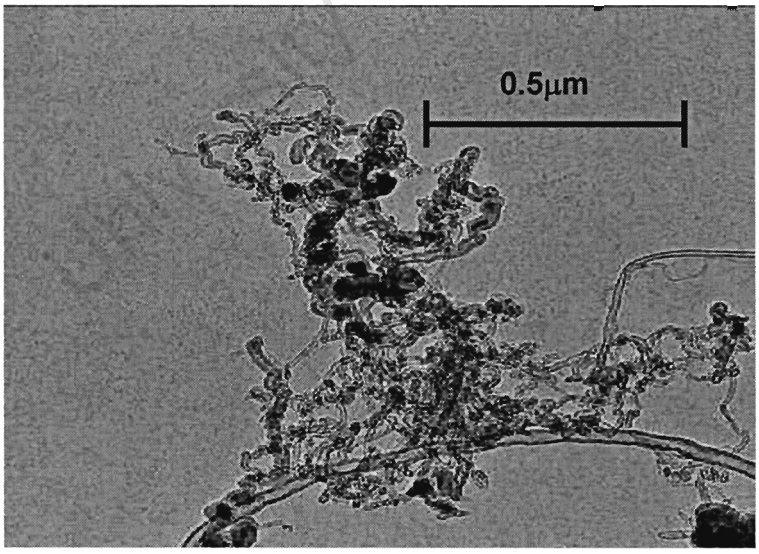

Figure 3- 22. A TEM image of carbon nanotubes grown from sample WS 15-50 at 650°C.

Table 3- 7. Carbon nanotube diameters for the sample WS 15-50 grown at different synthesis temperatures.

	Carbon Nanotubes				
Temperature (°C)	Average External Diameter (nm)	σ_{Ext} (nm)	Average Internal Diameter (nm)	σ_{Int} (nm)	n
560	80	39	18	10	30
650	15	7	7	3	47

The results in Figure 3-21 and 3-22 together with Table 3-7 show the same nanotube morphology and trend as in the similar experiment conducted with sample WS 20-33 and at twice the WHSV of 1.9L/g_{cat}.hr. At the moderate temperature of 560°C, the product of sample WS 15-50 appears to be similar to that of sample WS 20-33 and consists of nanotubes with a large average diameter of 83nm together with a great variation in external diameter. Sample WS 20-33 also consists of large diameter nanotubes but the external diameter is only found to be 37nm. The large initial nanotube diameters associated with sample WS 15-50 can possibly be attributed to the higher metal loading. The higher loading probably reduces the distribution of metal on the support and enhances sintering at the elevated temperatures associated with carbon nanotube synthesis.

At the highest synthesis temperature of 650°C, both sample WS 15-50 and WS 20-33 contain small diameter nanotubes with an abundance of encapsulated metal particles as seen in Figure 3-20 and 3-22. Again, the nanotubes of sample WS 15-50 were slightly larger at 16nm. Again, there is no correlation between the original crystallite size of the sample and the final product at any of the synthesis temperatures.

To conclude the results on the effect of temperature on morphology, it can be seen that as the temperature of nanotube synthesis increases, the diameter of the carbon nanotubes decreases and becomes more uniform.

3.3.2 Analysis of the Carbonaceous Product at Synthesised using Catalysts with Different Crystallite Sizes

The productivity together with the TEM and SEM images for the products synthesised with different water to surfactant ratios (and hence different crystallite sizes) can be seen in Figure 3-23 to 3-28. The results of the TEM images are summarised in Table 3-8. In this set of experiments using WS 15-50 the WHSV was halved to 0.9 L (STP)/g_{cat}·min and was compared to that of sample WS 20-33 which was synthesised at 1.9L (STP)/g_{cat}·min.

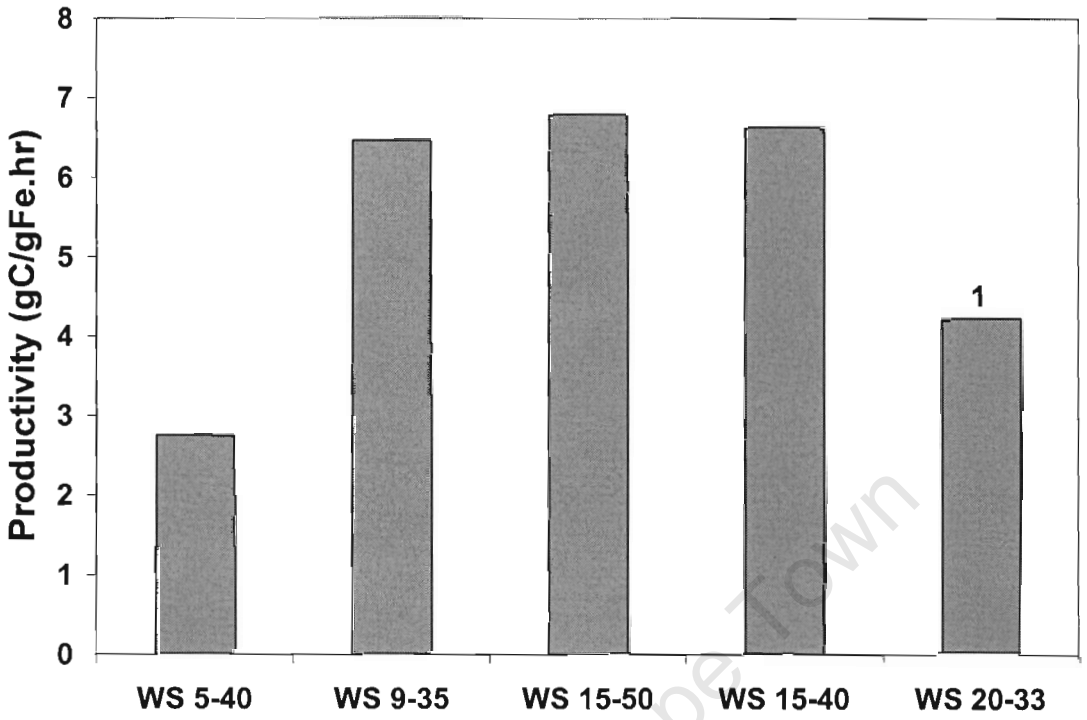

Figure 3- 23. Productivity with respect to iron content as a function of crystallite size at a synthesis temperature of 560°C. Experimental conditions: 0.9L (STP)/g_{cat}·hr.

1. The 15nm crystallite sample (Experimental condition: 1.9L (STP)/g_{cat}·hr) which was also normalised with respect to iron content.

The productivity was defined with respect to iron content due to the non-uniform loading found for the different water to surfactant ratios (Table 3-2). The lowest productivity was found sample WS 5-40 and the highest for the sample WS 15-50. It would appear that for crystallites above a certain size, the productivity would seem to be independent of the iron loading for a constant WHSV. The results in Figure 3-23 also suggest that with an increase in WHSV, there is an associated decrease in productivity.

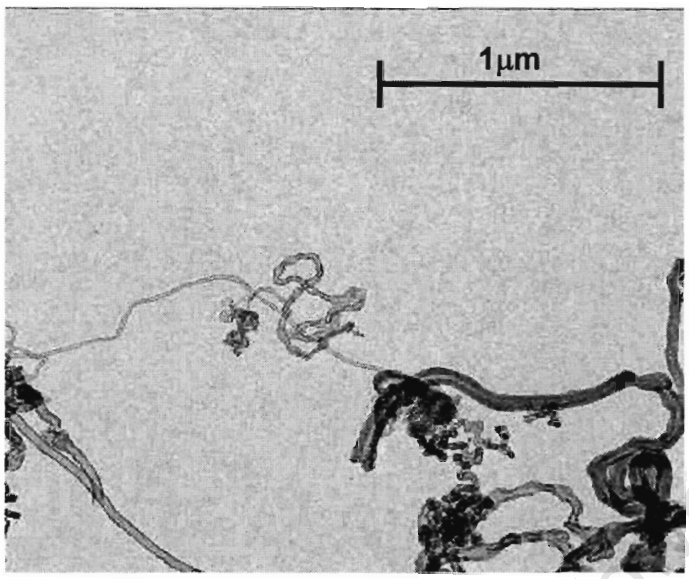

Figure 3- 24. TEM image of carbon nanotubes grown at 560°C from sample WS 5-40.

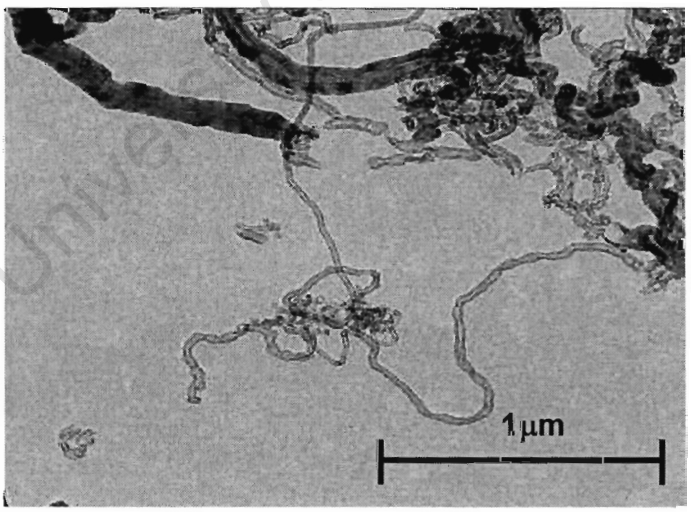

Figure 3- 25. A TEM image of carbon nanotubes grown from sample WS 9-35 at 560°C.

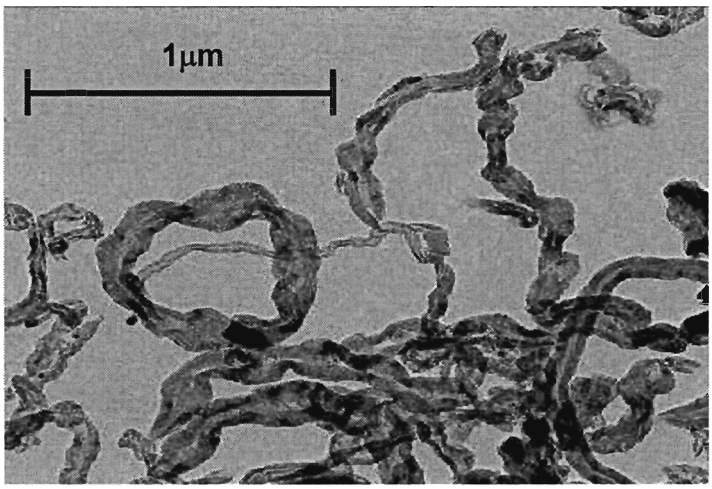

Figure 3- 26. A TEM image of carbon nanotubes grown sample WS 15-50 at 560°C.

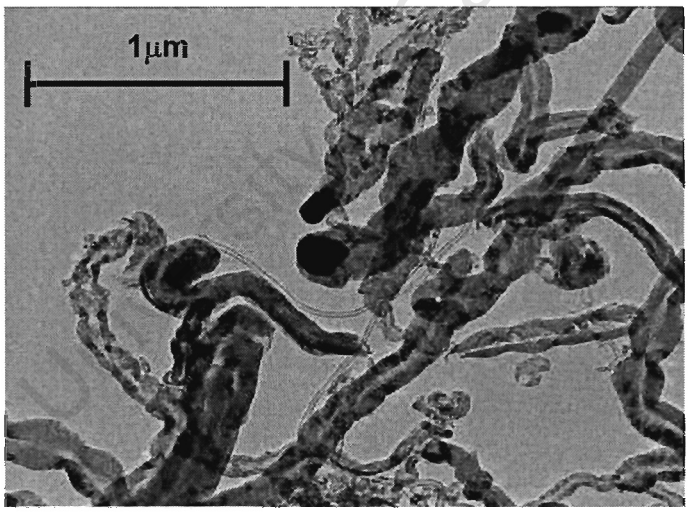

Figure 3- 27. A TEM image of carbon nanotubes grown sample WS 15-40 at 560°C.

The TEM images above for different water to surfactant ratios show that the morphology of the carbon nanotubes appears to be similar. This is clearly

obvious for all catalyst samples. The product itself is certainly non-uniform. The tubes vary in external diameter from 8nm in the sample WS 9-35 up to 161nm in the sample WS 15-50. The product consisted of nanotubes with both narrow and wide external and internal diameters. There was also the prevalence of both straight and twisted tubes as seen Figure 3-28. The average carbon nanotube diameters and the associated standard deviations can be seen in Table 3-8.

Table 3- 8. Carbon nanotube diameters shown for water to surfactant ratios together with the associated standard deviation.

	Carbon Nanotubes				
Sample ID	External Diameter (nm)	σ_{Ext} (nm)	Internal Diameter (nm)	σ_{Int} (nm)	n
WS 5-40	38	12	18	6	54
WS 9-35	40	29	12	8	56
WS 15-50	80	39	18	10	30
WS 15-40	64	34	14	8	43
WS 20-33[1]	37	18	7	3	33

1. Sample WS 20-33 was included for the sake of comparison although it was synthesised at twice the WHSV at 1.9L (STP)/g_{cat}·min as mentioned before.

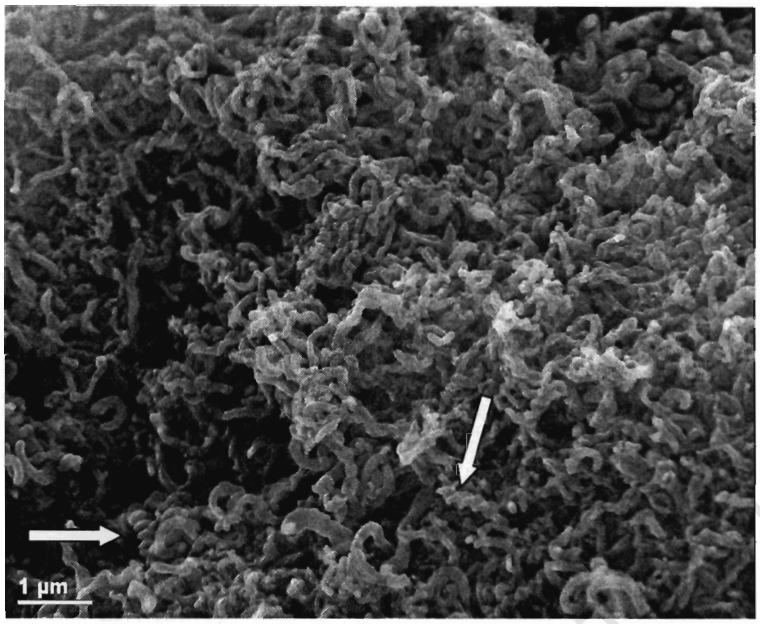

Figure 3- 28. A SEM image of carbon nanotubes synthesised at 10nm showing twisted tubes.

The results in Table 3-8 show that there is no direct link between the crystallite size obtained from a certain water to surfactant ratio (Table 3-4 and 3-5) and the resulting nanotube external diameter. Sample WS 15-50 (+/- 8.5nm) is expected to produce carbon nanotubes with a larger external diameter due to higher loading and increased sintering as mentioned above. This result is clearly seen in Table 3-8. However, sample WS 15-40 (8.7nm) produced the second largest tubes with an average diameter of 68nm despite having the lowest loading of 5.5% which does suggest that the increase in crystallite size due to the increase in water to surfactant ratio does also play a role in the morphology of the as grown carbon nanotubes.

It is also interesting to note that for sample WS 5-40 (6.1nm) and WS 9-35 (7nm), the average external diameters are similar to those of sample WS 20-33 (9.3nm) despite the different WHSV. All 3 of the aforementioned samples are produced at the same temperature and again might suggest that a certain crystallite size is

active at a specific temperature. The deviation of samples WS 15-50 and WS 15-40 crystallite samples does not necessarily refute the above statement but certainly suggests that further investigation is required to verify the above claim. Despite the large diameter nanotubes produced by sample WS 15-50, there does appear to be a general increase in nanotube external diameter with an increase in water to surfactant ratio, which does indicate that there is an effect of the crystallite size.

The results also indicate that carbon nanotubes of <10nm were synthesised. This suggests that the crystallite size effect on the nanotube diameter can only be realised if the metal particles are well distributed on the support surface. As mentioned before, sintering is probably responsible for the larger diameter tubes, which suggests that the metal particles responsible were in close proximity to one another. This result is in agreement with the observations of the metal catalysts where it was found that due to ultrasonic treatment, agglomerates of the metal catalysts were seen in both TEM and SEM images.

CHAPTER 4: DISCUSSION

4.1 Catalyst Preparation and Characterisation

4.1.1 The Effect of Catalyst Preparation on Iron Loading

The aim of using the reverse micelle technique was to produce nanometre sized iron oxide crystallites, which could be well distributed on an alumina support. In order to have the metal well distributed on the support, a desired loading of 15 wt.-% was chosen. By knowing the concentration and volume of the iron salt solution, the mass of iron produced could be calculated assuming all iron in solution precipitated as iron oxide crystallites.

The reverse micelle synthesis produced an iron loading of <13% for all water to surfactant ratios. This indicated that the reverse micelle technique may not lead to the precipitation of all iron in solution as iron oxide crystallites. This might have led to the lack of consistency in the average iron loading, which ranged from as low as 6.8% up to 12.1%.

The variation in iron loading might have originated from the extensive cleaning and washing steps applied in the synthesis of the catalyst accompanying the reverse micelle technique. During the cleaning and washing steps, acetone was used to remove the surfactant. The iron catalyst and support was allowed to settle and the clear liquid decanted off. With the large number of these washing steps iron crystallites which may not have settled would have been lost with the decanted liquid. To account for the mass loss of iron, the decanted liquid could have been placed in beaker with a known mass. The acetone could have been subsequently burned off and the mass loss determined with each washing step.

The precipitate itself could have also been analysed perhaps via AA to determine the relative amounts of iron and possibly aluminium lost.

Another reason linked to the cleaning steps is that a single reverse micelle synthesis produces only approximately 0.2g of iron and as a result, a number of batches needed to be synthesised in order to produce sufficient catalyst for repeated nanotube synthesis experiments.

If precipitated iron can be removed easily, the anchorage of the iron on the alumina support is rather weak. This weak anchorage stems from the method of synthesis. The precipitation of the iron in solution occurs prior to the adding of the alumina support. The iron and support are then combined as a physical mixture. This differs from "conventional" catalyst synthesis where the metal is usually in solution when contacted with the support. This may then result in strong metal-support interaction due to adsorption of iron ions onto the support.

The introduction of an ultrasonic treatment which was implemented both before and after drying under a vacuum, might have disrupted the already weak interaction as seen by the fact that in many cases the metal oxide was not associated with the support at all. The fluidisation conditions during calcination could also have resulted in both a loss of metal (which accounts for the lower than expected loading) and the disruption of the already weak metal-support interaction.

4.1.1.1 Uncertainty in Iron Content Determination

Both titrimetric analysis and atomic absorption spectroscopy were used to characterise the calcined catalyst to determine the iron loading. The results in terms of the iron loading were then compared. There was general agreement in the iron loading between AA and titration as expected but between sample WS 15-50 and WS 20-33, there was a difference in loading of >1.5% which can be

regarded as a significant difference. In both samples, the AA results were lower and this suggested a possible error in the AA results.

The error in AA was quantified by performing a mass balance on the obtained AA results. The mass balance was performed by taking the weight percentages given of iron and aluminium by AA and calculating the stoichiometric oxygen by assuming all iron as Fe_2O_3 and all aluminium as Al_2O_3. By subsequently adding the mass of iron, aluminium and oxygen, the projected mass could be calculated (see Table 4-1).

Table 4- 1. The difference between the actual catalyst mass and the projected catalyst mass using the values obtained from AA.

Sample	Catalyst Mass (g)	Projected Mass[1] (g)	Error (%)
WS 5-40	0.122	0.076	37.3
WS 9-35	0.106	0.080	25.0
WS 15-50	0.099	0.088	11.2
WS 15-40	0.101	0.075	26.0
WS 20-33	0.108	0.082	24.0

1: Taking the iron content and aluminium content as analysed using AAS and assuming iron to be present as Fe_2O_3 and aluminium as Al_2O_3 in the sample

In a similar manner, the aluminium content was calculated from the titration results by assuming all iron as Fe_2O_3 and subtracting this mass from the catalyst mass used (0.5g) to perform the titration. The remaining mass was assumed to be alumina and hence the mass of aluminium could be determined again via stoichiometry (Table 4-2).

Table 4- 2. Comparison of aluminium content obtained from AA and titrimetric analysis.

Sample	Al Content from AA (wt %)	Al Content from Titration (wt %)
WS 5-40	26.54	46.71
WS 9-35	33.52	47.24
WS 15-50	39.03	42.61
WS 15-40	34.21	47.74
WS 20-33	33.38	44.61

The above tables show that the determination of the Al-content using AAS results in an underestimation of the aluminium content. The underestimation of the aluminium content might be a result of incomplete digestion of the alumina during sample preparation for AA. The above tables also show that the greater the difference between the aluminium content in AA and the titrimetric analysis, the greater the error associated with the projected mass.

4.1.2 Synthesising Catalysts with Different Crystallite Sizes

The water-in-oil microemulsion or reverse micelle technique was used to control the size of the iron crystallites in the nanometre range. The control of the iron oxide crystallite diameter was achieved by varying the water to surfactant ratio according to Mabaso et al. (2005) for unsupported iron oxide.

It was found that the reverse micelle technique did produce nanometre sized crystallites with an increase in the water to surfactant ratio (Table 4-3) although they were not well distributed over the catalyst support.

Table 4- 3. A comparison of crystallites sizes for various water to surfactant ratios.

Sample	W/S ratio[1]	Crystallite Size[2] (nm)	Crystallite Size[3] (nm)
WS 5-40	0.13	6.1	3.0
WS 9-35	0.26	7.0	7.4
WS 15-50	0.30	8.5	8.2
WS 15-40	0.38	8.7	9.0
WS 20-33	0.61	9.3	17.2

1. W/S : water to surfactant ratio
2. Crystallite size taken as an average of XRD and TEM measurements
3. Crystallite size taken from the work of Mabaso et al. (2005) also as an average of XRD and TEM measurements.

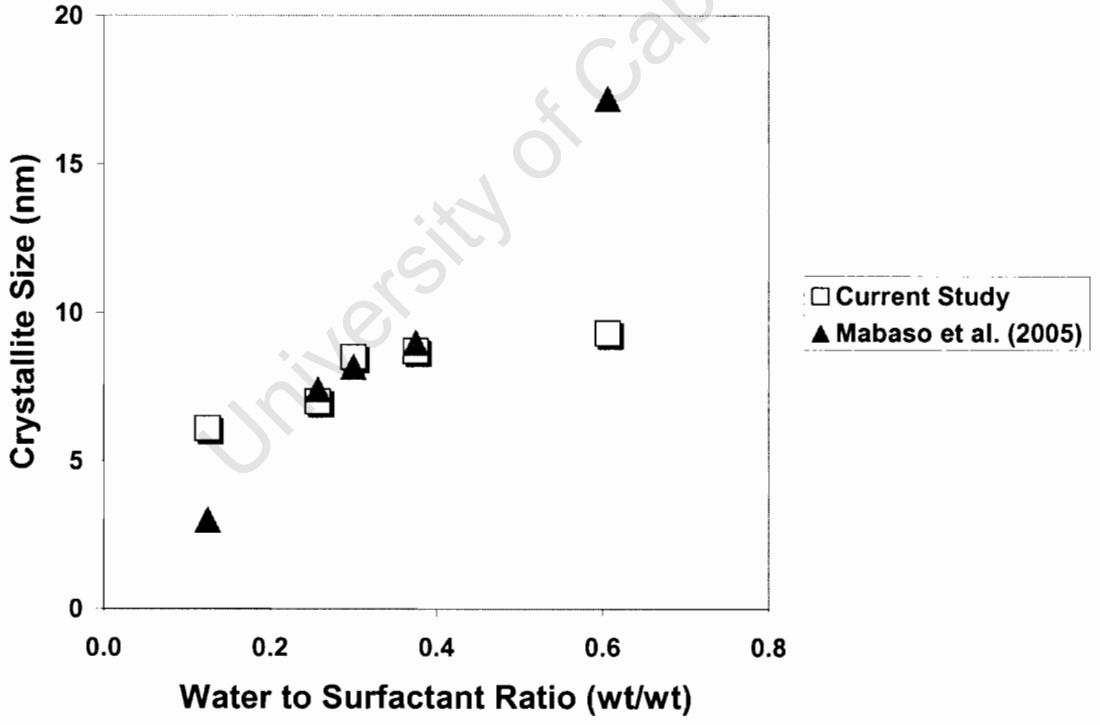

Figure 4- 1. Comparison of the average crystallite size obtained with increasing water to surfactant ratios. The crystallite size is taken as an average of XRD and TEM measurements.

An increase in the water to surfactant ratio is expected to produce an increase in crystallite size. An increase in the amount of water compared to the surfactant should produce larger crystallites due to an increase in size of the water droplet and hence the reverse micelle (Fulton et al., 1993). The actual micelle is the micro reactor in which precipitation of the crystallite takes place and hence reflects the size of the crystallite.

In comparison with the work of Mabaso et al. (2005), the obtained crystallite sizes appear to be similar for samples WS 9-35, WS 15-50 and WS 15-40 with the major differences appearing at the smallest and largest water to surfactant ratios. Mabaso et al. (2005) found a linear relationship between the water to surfactant ratio and the obtained crystallite size. That relationship is not completely realised in the current study due to the differences at the lowest and highest water to surfactant ratios.

The greatest difference is found in the highest water to surfactant ratio with a difference of 8nm between the crystallite size in the current study and the work of Mabaso et al. (2005). The smaller crystallite size encountered at WS 20-33 was thought to be attributed to some interaction of the support with the metal oxide during synthesis. This however is unlikely due to the fact that interchange of reactants between micelle droplets during collisions is believe to be rapid and as such occurs during the mixing stage (Lopez-Quintela and Rivas, 1993). This means that precipitation would have occurred before the support had been added.

The differences in average crystallite size in the current work and that of Mabaso et al. (2005) can be attributed to the differences in the synthesis route taken. In the current study, far more attention was given to ensuring that the metal crystallites were well distributed on the support and hence a number of additional steps were included during catalyst synthesis compared to the work by Mabaso

et al (2005). The greatest difference between the current study and that of Mabaso et al. (2005) was the inclusion of the ultrasonic steps. The addition of the ultrasonic steps together with increased cleaning and drying steps can account for the difference in average crystallite size. This is perhaps due to the loss of a certain size fraction of iron oxide crystallites during these vigorous ultra sonic and cleaning steps as discussed above.

Mabaso et al. (2005) observed an increase in the standard deviation with an increase in water to surfactant ratio. This produced larger crystallites with a wider particle size distribution. This was attributed to the fact that larger water to surfactant ratios produce larger droplets and this decreases the ability of the surfactant to stabilize these larger droplets. The particles are believed to undergo slow flocculation and hence produce larger crystallites and greater size distributions (Limin et al., 1996). Quite contrary to these findings, the standard deviation in the current study decreased with increasing water to surfactant ratios. This was probably due the ease of observing and counting iron oxide crystallites with TEM when larger crystallites were produced. At lower water to surfactant ratios, the smaller crystallites were harder to identify due to agglomeration and as such produced larger standard deviations.

4.2 Carbon Nanotube Synthesis

4.2.1 Effect of Temperature on Productivity

It was observed that with increasing temperature the productivity for the synthesis of carbon nanotubes reached a maximum and then decreased. This effect is not typically expected, and might be an indication of thermodynamic limitations or catalyst deactivation.

The carbon nanotube synthesis can be stoichiometrically written as:

$$2CO \rightarrow CO_2 + C_{nanotubes} \qquad \Delta H^{rxn}(298K) = -172.5 \text{ kJ/mol} \qquad (4\text{-}1)$$

or in the presence of hydrogen,

$$CO + H_2 \rightarrow H_2O + C_{nanotubes} \qquad \Delta H^{rxn}(298K) = -131.3 \text{ kJ/mol} \qquad (4\text{-}2)$$

If the reaction goes to equilibrium, the ratio of the partial pressures corresponds to the equilibrium constant. The product composition emerging from the reactor was not measured, but the conversion of carbon monoxide (and hydrogen in the case of reaction 4-2) and the yield of carbon dioxide and water can be related to the productivity of carbon nanotubes. Suppose, that the mass increase due to the formation of carbon nanotubes is Δm, then the rate at which carbon nanotubes are formed is given by $\Delta m/(t_{synthesis} \cdot M_C)$ with M_C the molar mass of carbon. Thus, the molar flow rates of the gaseous components are given by:
If only reaction 4-1 takes place then:

$$F_{CO} = F_{CO,in} - 2 \cdot \Delta m/(t_{synthesis} \cdot M_C)$$
$$F_{CO2} = \Delta m/(t_{synthesis} \cdot M_C)$$
$$F_{H2} = F_{H2,in}$$
$$F_{N2} = F_{N2,in}$$

If only reaction 4-2 takes place:

$$F_{CO} = F_{CO,in} - \Delta m/(t_{synthesis} \cdot M_C)$$
$$F_{H2} = F_{H2,in} - \Delta m/(t_{synthesis} \cdot M_C)$$
$$F_{H2O} = \Delta m/(t_{synthesis} \cdot M_C)$$
$$F_{N2} = F_{N2,in}$$

The partial pressure of each component can then be determined by the ratio of the flow of that component relative to the total flow rate times the total pressure.

The ratio of the partial pressures can then be plotted in a van't Hoff plot (see Figure 4-2). The data points calculated from the productivity at temperatures of 560°C and higher are reasonably represented by a straight line. The slope of the straight line is for both reactions approximately the same and would correspond to a heat of reaction of -233 kJ/mol. The calculated heat of reaction is significantly higher than the heat of reaction for the same reaction yielding graphite (for the Boudouard reaction the heat of reaction is -172.5 kJ/mol and for the reaction yielding graphite and water is -131.3 kJ/mol).

The position of the equilibrium for the formation of carbon nanotubes is shifted in comparison to that of the formation of graphite. The equilibrium partial pressure ratio at 570°C for the formation of graphite through the Boudouard reaction is 25.31 and for the formation of graphite and water (reaction 4-2) 7.94. These values are much larger than those seen in Figure 4-2 (0.1 for the formation of carbon nanotubes with carbon dioxide as a co-product and 0.3 for the formation of carbon nanotubes with water as co-product). This would indicate that the formation of carbon nanotubes is thermodynamically less favoured than the formation of graphite, which might be attributed to the strain energy in carbon nanotubes.

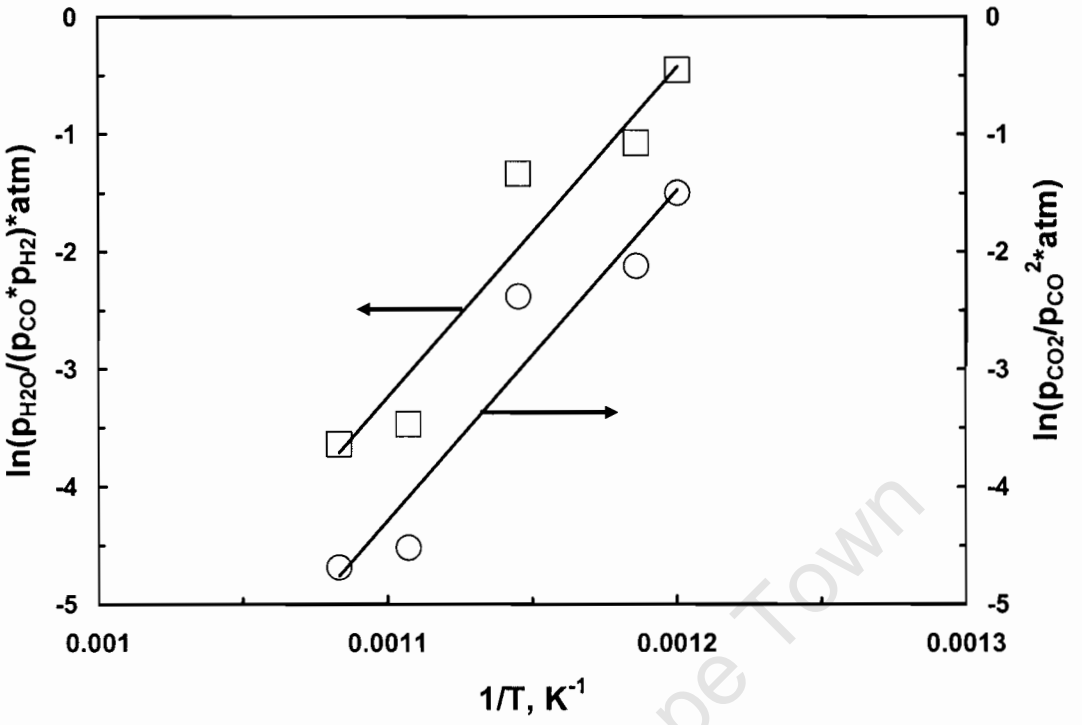

Figure 4- 2. Van't Hoff plot for the formation of carbon nanotubes assuming the synthesis proceeds to equilibrium with water as a co-product (□; left axis) and with carbon dioxide as co-product (○; right axis)

However, there is also some evidence suggesting encapsulation of the metal crystallites with carbon at elevated temperatures, which may lead to catalyst deactivation (see Figure 4-3). The encapsulation of the iron with carbon results in the blocking of the active sites necessary for carbon dissociation and adsorption and subsequent nanotube growth ceases. Initially, the decomposition of the carbon containing gas is the rate-determining step in nanotube growth (Toebes et al., 2002) but with an increase in temperature, the rate of the catalytic decomposition of the carbon containing gas increases. Steady state nanotube growth requires the delicate balance between decomposition and adsorption on the catalyst surface, diffusion through the metal and finally precipitation of the carbon as carbon nanotubes. As the synthesis temperature increases, the rate-determining step becomes the diffusion of carbon through the metal

(Bartholomew, 2001). If the rate of carbon decomposition and deposition on the catalyst surface becomes greater than the diffusion through the metal, encapsulation occurs. This might have led to a decrease in the productivity at temperatures greater than 560°C.

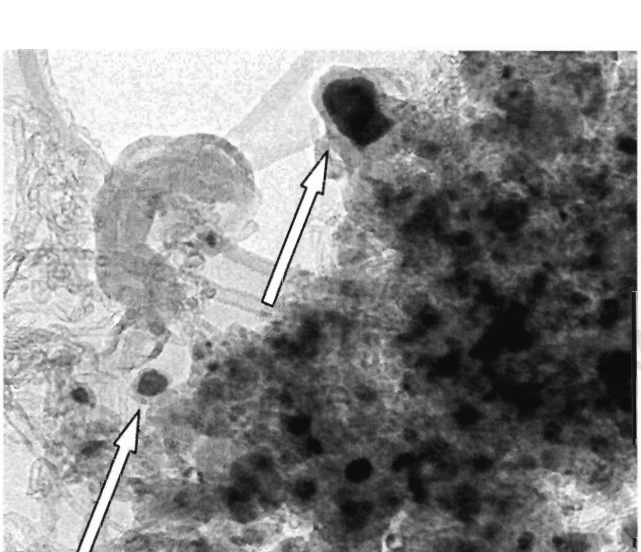

Figure 4- 3. A TEM image of encapsulated metal crystallites from sample WS 20-33 at 630°C.

A means to counteract the encapsulation of the catalyst is through gasification of the excess carbon. This provides a method to sustain the growth of carbon nanotubes and possibly tailor the productivity. Bartholomew (2001) has suggested that the rate of deactivation of the catalyst is defined by the following equation:

$$r_d = r_f - r_g \tag{4-3}$$

In the above equation, r_d is the rate of deactivation, r_f is the rate of formation and r_g is the rate of gasification. This hypothesis can then also be applied to the metal surface where r_f would represent the rate of the carbon source dissociating and

adsorbing onto the catalyst surface. In the case of the catalyst surface, the surface can be gasified by increasing the partial pressure of hydrogen in the feed as the synthesis temperature is increased or increase the H_2/CO ratio. The implications for the current study are then that the productivity can then be increased at elevated temperatures and the narrower and homogenous carbon nanotubes can be produced.

4.2.2 Controlling the External Diameter of Carbon Nanotubes at Constant Synthesis Temperature

The reverse micelle technique was used to produce different sized crystallites in the nanometre range. These different sized crystallites would hopefully allow size control of the external nanotube diameter at a constant synthesis temperature of 560°C.

The external diameters of the as-grown carbon nanotubes at a constant synthesis temperature did not directly correspond to the average diameter of the iron oxide crystallites (see Table 4-4). This result was contrary to the findings of Cheung et al. (2002) where the nanotube external diameters clearly reflected the iron nanocluster size. This result was also not expected because it was believed that if the size of the iron oxide crystallites was defined, then the carbon nanotube external diameters could be controlled. The external diameters of the as grown carbon nanotubes did however correspond to the metal crystallites at the tips of these nanotubes (see Figure 4-4). This result was expected according to the results of Baker et al. (1972). The size increase of the iron oxide crystallites at the tip of the carbon nanotubes can be attributed to sintering.

Table 4- 4. Comparison of the average calcined crystallite size with the average external nanotube diameter synthesised at 560°C. The iron content of the calcined catalyst is also shown.

Sample	Average Crystallite Size (TEM & XRD) (nm)	Average Nanotube External Diameter (nm)	Loading (wt % Fe)
WS 5-40	6.1	37.7	8.5
WS 9-35	7.0	40.5	7.8
WS 15-50	8.5	80.0	12.1
WS 15-40	8.7	64.1	6.8

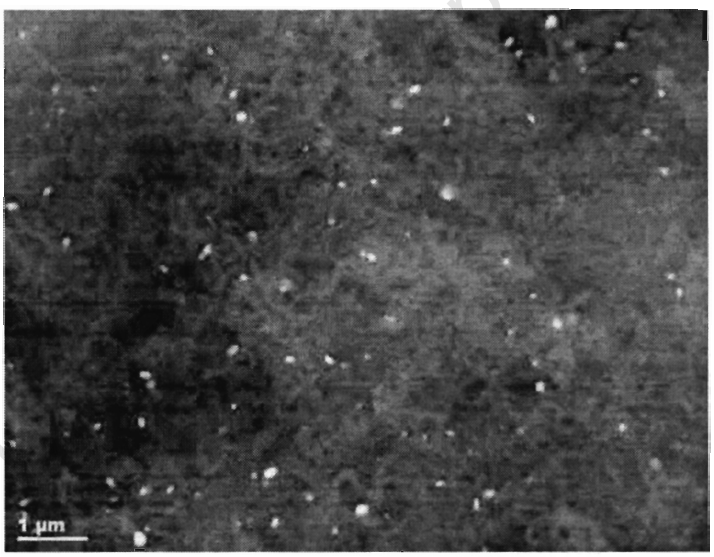

Figure 4- 4. SEM backscatter image of carbon nanotubes synthesised with WS 15-50 (d_{ave} = 8.5nm) showing the metal tips at the end of the tubes. The metal tips (d_{ave} = 80.6nm) are shown as the bright spots in the above figure and corresponds to the external nanotube diameter.

Sintering is defined as the thermal loss of catalytic surface area via crystallite growth (Bartholomew, 2001) and accounts for the large crystallites seen at the

tips of the as grown nanotubes. The presence of sintering is clearly evident for all catalyst samples as seen by the difference between the original crystallite size and final nanotube diameter (Table 4-4).

Sintering is dependent on a number of factors; of which temperature is the most important. For atoms or ions in the bulk to become sufficiently mobile the Tammann temperature needs to be attained while for species at the surface, the Hüttig temperature needs to be attained (Knözinger and Taglauer, 1997). These temperatures are defined as follows and the corresponding values can be found in Table 4-5:

$$T_{Tam} \approx 0.5T_{melt}^{bulk} \text{ (K)} \quad (4\text{-}4)$$

$$T_{Huttig} \approx 0.33T_{melt}^{bulk} \text{ (K)} \quad (4\text{-}5)$$

Table 4- 5. Melting, Tammann and Hüttig temperatures of pure iron.

	T_{melt} (K)	$T_{Tammann}$ (K)	$T_{Hüttig}$ (K)
Fe	1808	904	603

From the above table, it can be seen that the temperature of both reduction (400°C) and nanotube synthesis (560°C) are well above the Hüttig temperature of iron (330°C). This would indicate that species at the surface were already mobile during reduction and then again during nanotube synthesis. Although sintering is a kinetically slow process (Bartholomew, 2001), the reduction time of 12hrs would have been sufficient to facilitate sintering before nanotube synthesis actually occurred.

The effect of sintering might have been enhanced by the suggested weak metal-support interaction (Knözinger and Taglauer, 1997). This could possibly have

increased the mobility of iron on the support to produce both collision and coalescence. Cheung et al. (2002) in contrast, showed no sintering of iron on the support which suggested a strong bond of the metal on the support. This allowed for a direct correlation between the iron nanocluster size and the external diameter of the as grown carbon nanotubes. Localisation of metal crystallites in the pores of the support and in agglomerates formed during the reverse micelle synthesis might also have enhanced the effect of sintering (Knözinger and Taglauer, 1997).

Although a direct relationship between crystallite size and nanotube diameter was not realised, the increase in external nanotube diameters does appear to mirror the increase in crystallite size (Table 4-4). A similar trend was observed by Kukovistky et al. (2002) for nickel particles supported on amorphous carbon, where the distribution of nanotube diameters mirrored that of the particle size distribution of the catalyst for nanotube synthesis at 700°C. This was despite the difference in the initial nickel crystallite diameters and the final nanotube external diameters.

The only exception is in sample WS 15-50 for which the average nanotube diameter is the greatest at 80.0nm. This again could be related to the extent of sintering. In the case of sample WS 15-50, the greater loading of 12.1% (see Table 4-4) accounts for increased sintering in this sample because with an increase in metal loading, a corresponding decrease in the activation energy can be seen (Bartholomew, 2001).

4.2.3 The Effect of Synthesis Temperature on the Size and Morphology of Carbon Nanotubes

The aim of keeping the crystallite size constant (sample WS 20-33) and varying the synthesis temperature was to observe the effect of temperature on both the

size and morphology of as grown carbon nanotubes. It should be noted that in general the quality of the nanotubes grown in the current is poor (see Figures 3-14 to 3-22 and Figure 3-24 to 3-28). This is highlighted by the absence of straight tubes as well as the prevalence of defects such as bent and curled tubes. This is probably due to the low synthesis temperature (520 to 650°C) since the quality of the carbon nanotubes grown is dependent on temperature as previously discussed. At the lowest synthesis temperature there is the prevalence of thick fibrils with no hollow internal cavity while at the highest synthesis temperature, there are little long straight tubes. It should be noted that the highest synthesis temperature used to synthesise carbon nanotubes in the current study is 150°C lower than that used by Cheung et al. (2002) to synthesise long straight tubes with a low density of defects.

It was found that with an increase in temperature, the external nanotube diameter reached a maximum value of 37nm and then decreased to a value of 13nm. With this decrease in external diameter, the product itself became more uniform in terms of both morphology and external diameter as indicated by the accompanying decrease in standard deviation (see Table 4-6).

Table 4- 6. The effect of temperature on the external carbon nanotube diameter.

Temperature (°C)	External Diameter (nm)	σ_{Ext} (nm)	n
520	13	6	37
560	37	18	33
600	30	12	30
630	13	5	48
650	13	5	52

The increase of external diameter with temperature has been attributed to sintering (Lee et al., 2001; Li et al., 2002; Ducati et al., 2002). The decrease in external diameter with an increase in synthesis temperature from 630 to 650°C was not expected. This was due to the close proximity of these temperatures with the Tammann temperature (631°C) of pure iron. Hoogenraad (1995) attributed this decrease in external nanotube diameter to the carbon source gas (CO) and the exothermicity of the Boudouard reaction. This produced lower carbon partial pressures on the surface of the metal crystallites with an increase in temperature and only facilitated growth on the smaller more reactive crystallites. This hypothesis does not account for the sintering, which should occur at elevated synthesis temperature or the prevalence of more uniform external nanotube diameters.

The above argument could suggest that it is quite possible that another mechanism or perhaps more than one mechanism can be prevalent during the growth of carbon nanotubes. At low temperature, the tip growth mechanism

(Baker et al., 1972) is most likely the mechanism active in the growth of carbon nanotubes and fibrils as seen by the metal tip of the as grown carbon nanotube. As the synthesis temperature increases, it is believed that a liquid or quasi-liquid state (Kukovitsky et al., 2002; Reshetenko et al., 2004) emerges as a result of iron oversaturated with carbon. The base growth or extrusion mechanism is also believed to become active (Kukovitsky et al., 2002; Qian et al., 2003) (see Figure 4-5). A possible tell-tail sign of this is that there is no metal crystallite at the tip of the carbon nanotube (see Figure 4-6a).

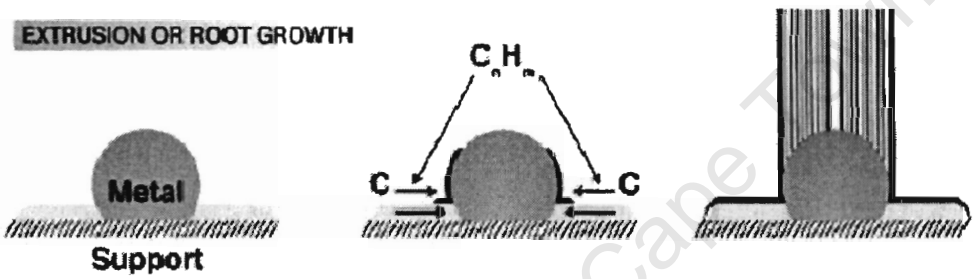

Figure 4- 5. A schematic diagram showing the base growth or extrusion mechanism for carbon nanotube growth (from Daenen et al., 2003).

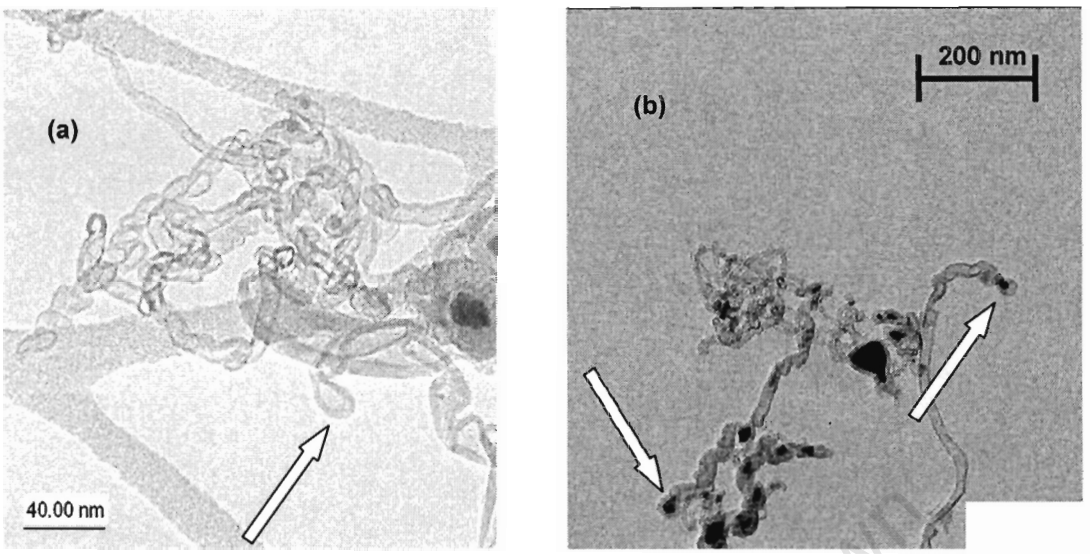

Figure 4- 6. (a) A TEM image of carbon nanotubes grown from sample WS 20-33 at 630°C showing no metal tip at the end of the nanotube indicating the possibility of the base growth mechanism. (b) A TEM image of carbon nanotubes grown at 650°C from sample WS 15-40 confirming the tip growth mechanism.

The liquid-like behaviour of the iron oversaturated with carbon now produces a much stronger bond to the support and can account for the absence of the metal particle at the tip (Kukovitsky et al., 2002). Sintering is still believed to occur as a result of the mobility of this quasi-liquid state at the elevated synthesis temperatures. The sintered material most likely undergoes fragmentation or redispersion (opposite of sintering) of the metal crystallites to produce a more Gaussian-like and narrower particle size distribution which then produces nanotubes of a narrower and more uniform size distribution in terms of the external diameter and morphology. The nanotube diameter now becomes a function of the equilibrium shape and size of the metal under capillary forces and surface tension (Kukovitsky et al., 2002) and not of the original catalyst particle size distribution.

The base growth mechanism can be responsible for metal particles being found at the base, within the tube and possibly at the tips as well. This is possibly due to the capillary forces and the immense strain imposed by the graphite layers on the metal (Hoogenraad, 1995). The implication of these forces is that the metal particle is squeezed into the nanotube from the base of the nanotube. This squeezing action together with the quasi-liquid state imposed by the high synthesis temperature can also result in the formation of nanowires (Qian et al., 2003). There is evidence of this in the current study that does allude to the possibility of this quasi-liquid state discussed earlier and the possibility of multiple growth techniques being active (see Figure 4-7)

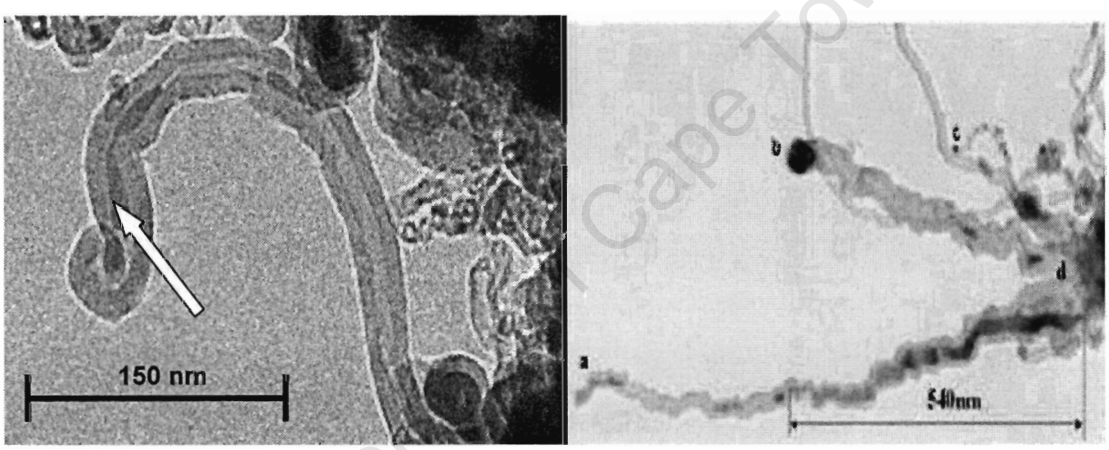

Figure 4- 7. Two TEM images showing the similarities between the current work (Left) grown from sample WS 15-30 at 630°C and the nanowires (Right) grown by Qian et al. (2003) with $Fe/Mo/Al_2O_3$ at 550°C and ethylene as the carbon source.

The mechanism of Hoogenraad (1995), certainly accounts for the growth of smaller nanotubes at elevated temperatures and the complete lack of larger nanotubes. It appears that iron crystallites of larger than 20nm do not facilitate nanotube growth possibly due to the lower or insufficient carbon partial pressures at the surface to facilitate nanotube growth.

Ducati et al. (2002) propose that for a fixed pressure and certain carbon source, there exists an optimum metal crystallite size for carbon source decomposition, diffusion and precipitation. This translates to optimum operation conditions for steady state nanotube growth to occur for a certain crystallite size. This hypothesis seems to be in agreement with the work of Hoogenraad (1995), where a certain crystallite size facilitates growth while larger crystallites do not. This hypothesis also accounts for the fact that larger sintered crystallites produce no nanotubes.

These hypothesises do not however answer the question of why despite the presence of sintering, the nanotube diameter becomes more uniform. Hence, the hypothesis of both Kukovitsky et al. (2003) and Qian et al. (2003) seems to provide an alternative or rather a joint mechanism to account for this.

CHAPTER 5: CONCLUSIONS

The iron loading for all water to surfactant ratios was below the desired level of 15 wt.-% and it was concluded that perhaps the reverse micelle technique does not precipitate all iron in solution as iron oxide crystallites. The loss of iron oxide was also attributed to the extensive cleaning regime implemented together with the weak anchorage of the metal oxide on the support. The reverse micelle technique did produce nanometre sized iron oxide crystallites but a direct linear relationship between the water to surfactant ratio and crystallite size was not achieved.

The productivity of carbon nanotubes over supported iron catalysts was governed by kinetics at low temperature while at high temperature it was not clear whether the productivity was governed by kinetics or thermodynamic equilibrium limitations. Some evidence of kinetic limitations was the encapsulation of the iron oxide crystallites with carbon. However, thermodynamic limitation on the growth of carbon nanotubes could not be ruled out.

The carbon nanotube external diameters did not mirror the calcined iron oxide crystallite sizes for a constant synthesis temperature. This difference was attributed to sintering or coalescence enhanced by the weak metal-support interaction. The carbon nanotube external diameters did mirror the increase in iron oxide crystallite size with the increase in water to surfactant ratio.

The effect of synthesis temperature on a fixed water to surfactant ratio showed that as temperature increased the external nanotube diameter increased, reached a maximum and then decreased to a uniform value. The increase in external diameter was again attributed to sintering. The decrease in external nanotube diameter might be attributed to the formation of a quasi-liquid state comprised of iron oversaturated with carbon, which caused redispersion and a

narrower Gaussian-like distribution. It was also concluded that perhaps more than one growth mechanism became active with an increase in temperature namely from the tip growth at low temperature to a base growth at elevated temperatures.

REFERENCES

Ajayan, P. M., Zhou, O.
"Applications of carbon nanotubes"
Carbon Nanotubes
(ed. M. S. Dresselhaus and G. Dresselhaus),
Springer-Verlag Publications, p391, (2001).

Avdeeva, L. B., Goncharova, O. V., Kochubey, D. I., Zaikovskii, V. I., Plyasova, L. M., Novgorodov, B. N., Shaikhutdonov, S. K.
"Coprecipitated Ni-alumina and Ni-Cu-alumina catalysts of methane decomposition and carbon deposition – Evolution of the catalysts in reaction"
Applied Catalysis A: General **141** (1996), 117.

Avdeeva, L. B., Reshetenko, T. V., Ismagilov, Z. R., Likholobov, V. A.
"Iron-containing catalysts of methane decomposition"
Applied Catalysis A: General **228** (2002), 53.

Baker, R. T. K., Barber, M. A., Harris, P. S., Feates, F. S., and Waite, R. J.
"Nucleation and Growth of Carbon Deposits from the Nickel Catalyzed Decomposition of Acetylene"
Journal of Catalysis **26** (1972), 51

Bartholomew, C. H.
"Mechanisms of Catalyst Deactivation"
Applied Catalysis A: General **212** (2001), 17

Baughman, R. H., Zakhidov, A. A., de Heer, W. A.
"Carbon-Nanotubes-the Route toward Applications"
Science **297** (2002), 787

Blahd, K., Falk, L. K. L., Rohmund, F.
"On the iron catalysed growth of single-walled carbon nanotubes and encapsulated metal particles in the gas phase"
Applied Physics A **70** (2000), 317

Bethune, D. S., Kiang, C. H., de Vries, M. S., Gorman, G., Savoy, R., Vazquez, J., Beyers, R.
"Cobalt-catalysed growth of carbon nanotubes with single-atomic-layer walls"
Nature **363** (1993), 605

Bonard, J., Laszlo, F., Ugarte, D., de Heer, W., Chatelain, A.
"Physics and Chemistry of Carbon Nanostructures"
European Chemistry Chronicle **3** (1998), 9

Boutonnet, M., Kizling, J., Stenius, P., Maire, G.
"The preparation of monodisperse colloidal metal particles from microemulsions"
Colloids and Surfaces **5** (1982), 209

Brown, R., Cooper, M. E., Whan, D. A.
"Temperature Programmed Reduction of Alumina-Supported Iron, Cobalt and Nickel Bimetallic Catalysts"
Applied Catalysis **3** (1982), 177

Bukur, D. B., and Sivaraj, C.
"Supported iron catalysts for slurry phase Fischer-Tropsch synthesis"
Applied Catalysis A: General **231** (2002), 201

Capek, I.
"Preparation of metal nanoparticles in water-in-oil (w/o) microemulsions"
Advances in Colloid and Interface Science **110** (2004), 49

Chang, G., Huang, T., Hung, H.
"Reverse Micelles as Life-Mimicking Systems"
Proc. National Science Council. ROC (B) **24** (2000), 89

Cheung, C. L., Kurtz, A., Park, H., Lieber, C. M.
"Diameter-Controlled Synthesis of Carbon Nanotubes"
Journal of Physical Chemistry **106** (2002), 2429

Daenen, M., de Fouw, R. D., Hamers, B., Janssen, P. G. A., Schouteden, K., Veld, M. A. J.
"The wonderous world of carbon nanotubes – a review of current carbon nanotube technologies"
A literature review and report by the Eindhoven University of Technology, 2003.

Dai, H., Rinzler, A. G., Nikolaev, P., Thess, A., Colbert, D. T., Smalley, R.
"Single-wall nanotubes produced by the metal-catalysed disproportionation of carbon monoxide"
Chemical Physics Letters **260** (1996), 471

De Bokx, P. K., Kock, A. J. H. M., Boellaard, E., Klop, W., Geus, J. W.
"The Formation of Filamentous Carbon on Iron and Nickel Catalysts (Thermodynamics)"
Journal of Catalysis **96** (1985a), 454

De Jong, K. P., Geus, J. W.
"Carbon Nanofibers: Catalytic Synthesis and Applications"
Catalysis Review – Science and Engineering **42** (2000), 481

Demczyk, B.G., Wang, Y.M., Cumings, J., Hetman M., Han, W., Zettl, A.
"Direct mechanical measurement of the tensile strength and elastic modulus of multiwalled carbon nanotubes"
Materials Science and Engineering **A334** (2002), 173

Dresselhaus, M. S., Dresselhaus, G., and Saito, R.
"Physics of Carbon Nanotubes,"
Carbon **7** (1995), 883.

Ducati, C., Alexandrou, I., Chhowalla, M., Amaratunga, G. A. J., Robertson, J.
"Temperature selective growth of carbon nanotubes by chemical vapor deposition"
Journal of Applied Physics **92** (2002), 3299

Ebbesen, T. W., Ajayan, P. M.
"Large-scale synthesis of carbon nanotubes"
Nature **358** (1992), 220

Ermakova, M. A., Ermakov, D. Y., Chuvilin, A. L., Kuvshinov, G. G.
"Decompositon of Methane over Iron Catalysts at the Range of Moderate Temperatures: The influence of Structure of the Catalytic Systems and the Reaction Conditions on the Yield of Carbon and Morphology of Carbon Filaments"
Journal of Catalysis **201** (2001), 183

Fulton, J. L., Bean, R. M., Linehan, J. C.
"Process of Forming Metal Compounds Using Reverse Micelle or Reverse Microemulsion Systems"
US Patent **WO9314022** (1993)

Guo, T., Nikolaev, P., Thess, A., Colbert, D. T., Smalley, R. E.
"Catalytic growth of single-walled nanotubes by laser vaporization"
Chemical Physics Letters **243** (1995), 49

Hernadi, K., Fonseca, A., Nagy, J. B., Bernaerts, D., Lucas, A. A.
"Fe-Catalyzed Carbon Nanotube Formation"
Carbon **34** (1996), 1249

Hernadi, K., Fonseca, A., Nagy, J. B., Siska, A., Kiricsi, I.
"Production of nanotubes by the catalytic decomposition of different carbon-containing compounds"
Applied Catalysis A: General **199** (2000), 245

Hernadi, K., Konya, Z., Siska, A., Kiss, J., Oszko, A., Nagy, J. B., Kiricsi, I.
"On the role of catalyst, catalyst support and their interaction in the synthesis of carbon nanotubes by CCVD"
Materials Chemistry and Physics **77** (2002), 536

Hoogenraad, M.
"Growth and Utilization of Carbon Fibrils"
PhD Thesis, University Utrecht Netherlands (1995).

Hughes, I. S. C., and Newman, J. O. H.
"The Characterisation of Unsupported Iron and Manganese-Promoted Iron Catalysts by X-ray Photoelectron Spectroscopy and Temperature-Programmed Reduction"
Applied Catalysis **30** (1987), 303

Iijima, S.
"Helical microtubules of graphitic carbon"
Nature **354** (1991), 56

Iijima, S., Ichihashi, T.
"Single-shell carbon nanotubes of 1-nm diameter"
Nature **363** (1993), 603

Ivanov, V., Fonseca, A., Nagy, J. B., Lucas, A., Lambin, P., Bernaerts, D., Zhang, X. B.
"Catalytic Production and Purification of Nanotubes Having Fullerene-Scale Diameters"
Carbon **33** (1995), 1727

Jacobsen, R. L., Tritt, T. M., Guth, J. R., Ehrlich, A. C., Gillespie, D. J.
"Mechanical properties of vapour-grown carbon fiber"
Carbon **33** (1995), 1217

Jose-Yacaman, M. J., Miki-Yoshida, M., Rendon, L.
"Catalytic growth of carbon microtubules with fullerene structure"
Applied Physics Letters **62** (1993), 202

Journet, C., Maser, W. K., Bernier, P., Loiseau, A., Lamy de la Chapelle, M., Lefrant, S., Deniard, P., Lee, R., Fischer, J. E.
"Large-scale production of single-walled carbon nanotubes by the electric-arc technique"
Nature **388** (1997), 756

Kibria, A. K. M. F., Nahm, K. S., Mo, Y. H., Kim, M. J.
"Synthesis of narrow-diameter carbon nanotubes from acetylene decomposition over an iron-nickel catalyst supported on alumina"
Carbon **40** (2002), 1241

Knözinger, H., Taglauer, E.
Spreading and Wetting
In "*Handbood of Heterogeneous Catalysis*"
(Edited by Ertl, G., Knözinger, H., Weitkamp, J.)
Wiley-VCH Verlagsgesellschaft mbH, Weinheim
Vol 1, (1997)

Kock, A. J. H. M., Fortuin, H. M., Geus, J. W.
"The Reduction Behavior of Supported Iron Catalysts in Hydrogen or Carbon Monoxide Atmospheres"
Journal of Catalysis **96** (1985), 261

Kukovitsky, E. F., L'vov, S. G., Sainov, N. A., Shustov, V. A., Chernozatonskii, L. A.
"Correlation between metal catalyst particle size and carbon nanotube growth"
Chemical Physics Letters **355** (2002), 497

Kuzmany, H., Kukovecz, A., Simona, F., Holzweber, M., Kramberger, C., T. Pichler, T.
"Functionalization of carbon nanotubes"
Synthetic Metals **141** (2004), 113

Lee, C. J., Park, J., Huh, Y., Lee, J. Y.
"Temperature effect on the growth of carbon nanotubes using thermal chemical vapour deposition"
Chemical Physics Letters **343** (2001), 33.

Li, W. Z., Wen, J. G., Ren, Z. F.
"Effect of temperature on growth and structure of carbon nanotubes by chemical vapour deposition"
Applied Physics A **74** (2002), 397

Limin, Q., Jiming, M., Humin, C., Zhenguo, Z.
"Preparation of $BaSO_4$ nanoparticles in non-ionic w/o microemulsions"
Colloids and Surfaces A: Physicochemical and Engineering Aspects **108** (1996), 117

Lopez-Quintela, M. A., Rivas, J.
"Chemical Reactions in Microemulsions: A Powerful Method to Obtain Ultrafine Particles"
Journal of Colloid and Interface Science **158** (1993), 446

Lui, J., Rinzler, A. G., Dai, H., Hafner, J. H., Bradley, R. K., Boul, P. J., Lu, A., Iverson, T., Shelimov, K., Huffman, C. B., Rodriguez-Macias, G., Shon, Y. S., Lee, T. R., Colbert, D. T., Smalley, R. E.
"Fullerene Pipes"
Science **280** (1998), 1253

Mabaso, E. I., Claeys, M., van Steen, E
"A Novel Preparation Method for Nano-sized Monodispersed Fe_2O_3 Crystallites"
To be submitted for publication (2005)

Mauron, P., Emmenegger, C., Sudan, P., Wenger, P., Rentsch, S., Zuttel, A.
"Fluidised-bed CVD synthesis of carbon nanotubes on Fe_2O_3/MgO"
Diamond and Related Materials **12** (2003), 780

Nagaraju, N., Fonseca, A., Konya, Z., Nagy, J. B.
"Alumina and silica supported metal catalysts for the production of carbon nantubes"
Journal of Molecular Catalysis A: Chemical **181** (2002), 57

Nhut, J., Viera, R., Pesant, L., Tessonnier, J., Keller, N., Ehret, G., Pham-Huu, C., Ledoux, M. J.
"Synthesis and catalytic uses of carbon and silicon carbide nanostructures"
Catalysis Today **76** (2002), 11

Niyogi, S., Hamon, M. A., Hu, H., Zhao, B., Bhowmik, P., Sen, R., Itkis, M. E., Haddon, R. C.
"Chemistry of Single-Walled Carbon Nanotubes"
Accounts of Chemical Research **35** (2002), 1105

Pillai, V., Kumar, P., Hou, M. J., Ayyub, P., Shah, D. O.
"Preparation of Nanoparticles of Silver Halides, Superconductors and Magnetic Materials using Water-In-Oil Microemulsions as Nano-Reactors"
Advances in Colloid and Interface Science **55** (1995), 24

Popov, V.
"Carbon nanotubes: properties and application"
Materials Science and Engineering **R43** (2004), 61

Prinsloo, F. F.
"Fischer-Tropsch synthesis over carbon nanotube supported iron catalysts"
MSc Thesis, University of Cape Town (2000).

Qian, W., Wei F., Lui, T., Wang, Z. W.
"The formation mechanism of the coaxial carbon-metal nanowires in a chemical vapor deposition process"
Solid State Communications **126** (2003), 365

Reshetenko, T. V., Avdeeva, L. B., Ushakov, V. A., Moroz, E. M., Shmakov, A. N., Kriventsov, V. V., Kochubey, D. I., Pavlyukhin, Y. T., Chuvilin, A. L., Ismagilov, Z. R.

"Coprecipitated iron-containing catalysts ($Fe-Al_2O_3$, $Fe-Co-Al_2O_3$, $Fe-Ni-Al_2O_3$) for methane decomposition at moderate temperatures. Part II. Evolution of the catalysts in reaction"
Applied Catalysis A: General **270** (2004), 87

Rostrup-Nielsen, J. R.
"Sulfur-passivated nickel catalysts for carbon-free steam reforming of methane"
Journal of Catalysis **85** (1984), 31

Serp, P., Corrias, M., Kalck, P.
"Carbon nanotubes and nanofibers in catalysis"
Applied Catalysis A: General **253** (2003), 337

Snoeck, J. W., Froment, G. F., Fowles, M.
"Filamentous carbon formation and gasification: thermodynamics, driving force, nucleation and steady state growth"
Journal of Catalysis **169** (1997), 240

Takenaka, S., Serizama, M., Otsuka, K.
"Formation of filamentous carbons over Fe catalysts through methane decomposition"
Journal of Catalysis **222** (2004), 520

Thess, A., Lee, R., Nikolaev, P., Dai, H., Petit, P., Robert, J., Xu, C., Lee, Y. H., Kim, S. G., Rinzler, A. G., Colbert, D. T., Scuseria, G. E., Tomanek, D., Fischer, J. E., Smalley, R. E.
"Crystalline Ropes of Metallic Carbon Nanotubes"
Science **273** (1996), 483

Toebes, M. L., Bitter, J. H., Jos van Dillen, A., de Jong, K. P.
"Impact of the structure and reactivity of nickel particles on the catalytic growth of carbon nanofibers"
Catalysis Today **76** (2002), 33

Weizhong, Q., Fei, W., Tang, L., Hao, Y., Guohua, L., Lan., X.
"Production of Carbon Nanotubes in a Packed Bed and a Fluidized Bed"
AIChe J **49** (2003), 619

Yakobson, B.I. Brabec, C.J. Bernholc, J.
"Nanomechanics of carbon tubes: instabilities beyond linear response"
Physics Review Letters **76** (1996), 2511.

Yang, R. T., Chen, J. P.
"Mechanism of Carbon Filament Growth on Metal Catalysts"
Journal of Catalysis **115** (1989), 52

Yu, M., Lourie, O., Dyer, M. J., Moloni, K., Kelly, T. F., Ruoff, R. S.
"Strength and breaking mechanism of multiwalled carbon nanotubes under tensile load"
Science **287** (2000), 637

APPENDICES

Appendix A

For both TPR and CVD, Brooks mass flow controllers were used to regulate and control flow. The mass flow controllers were calibrating using a wet gas flow meter at atmospheric pressure. The following figures are the mass flow calibration curves for the CVD unit in which both catalyst reduction and carbon nanotube synthesis was performed at Sasolburg as well as the calcination unit at UCT.

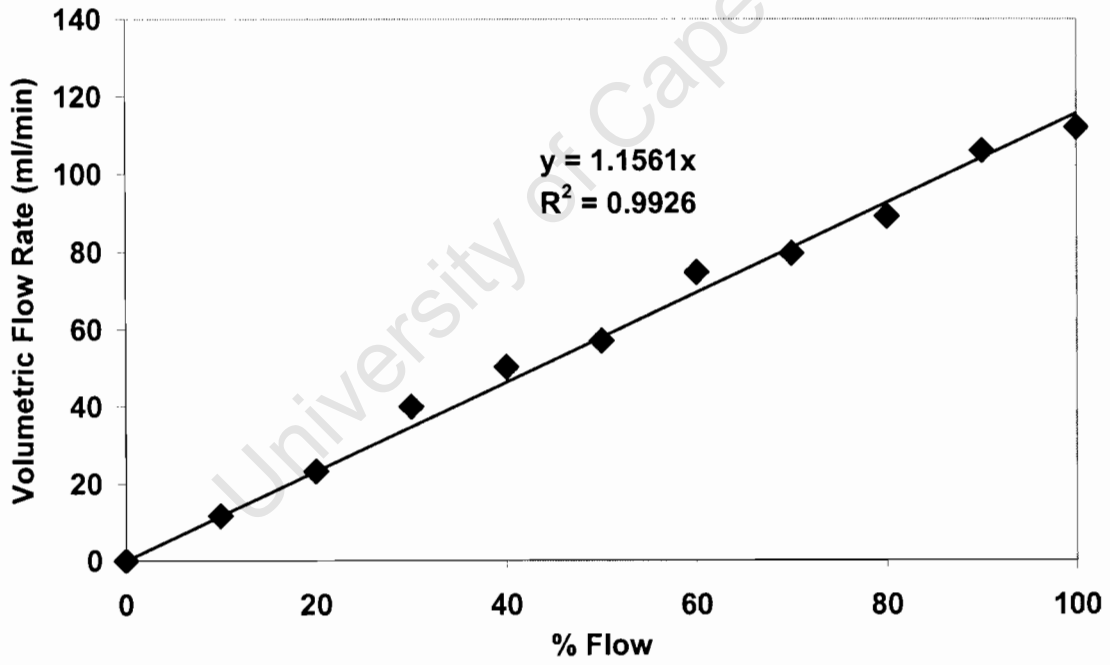

Figure A- 1. Mass flow calibration curve for carbon monoxide for the CVD unit.

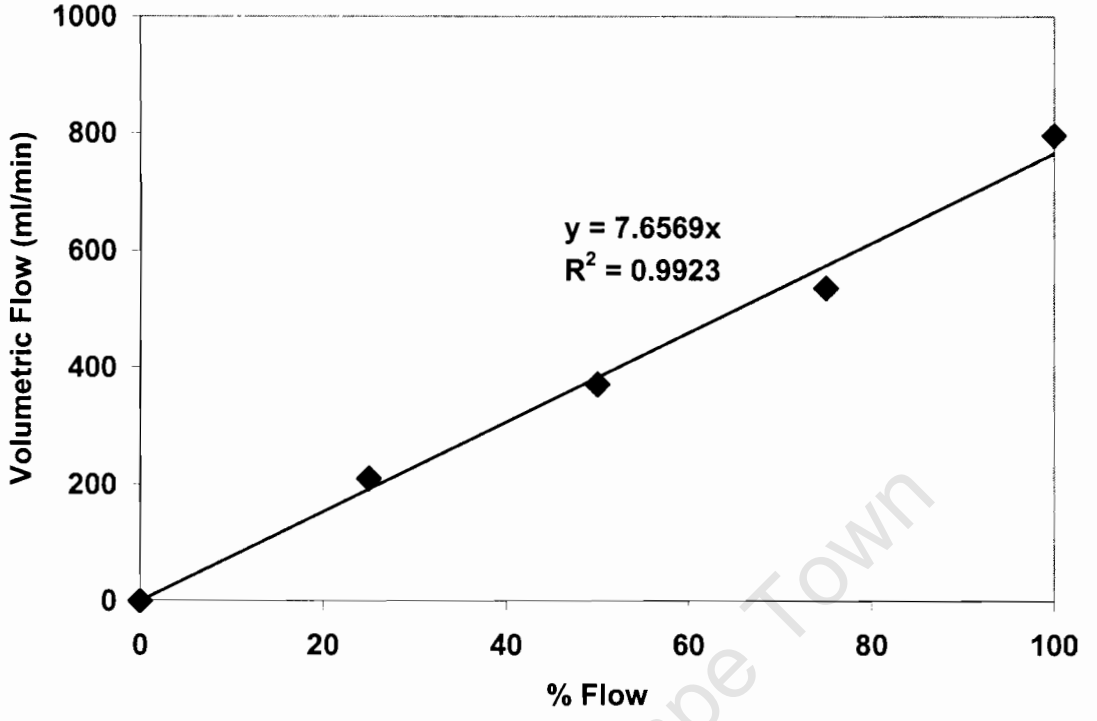

Figure A- 2. Mass flow calibration curve for hydrogen for the CVD unit.

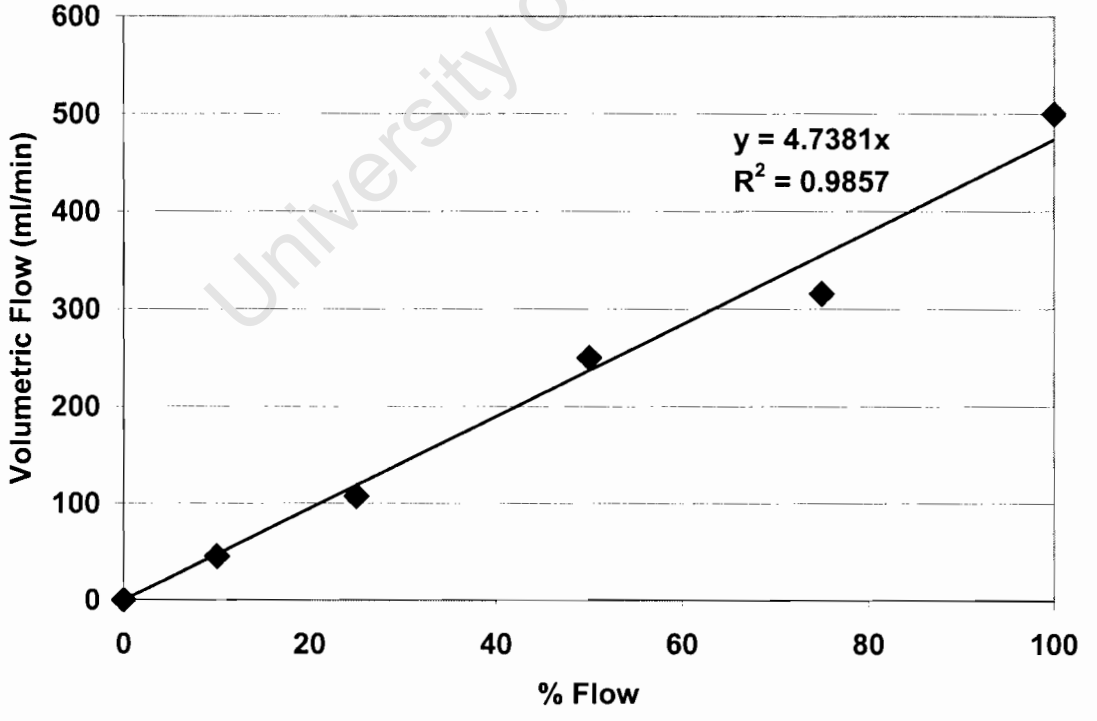

Figure A- 3. Mass flow calibration curve for nitrogen for the CVD unit.

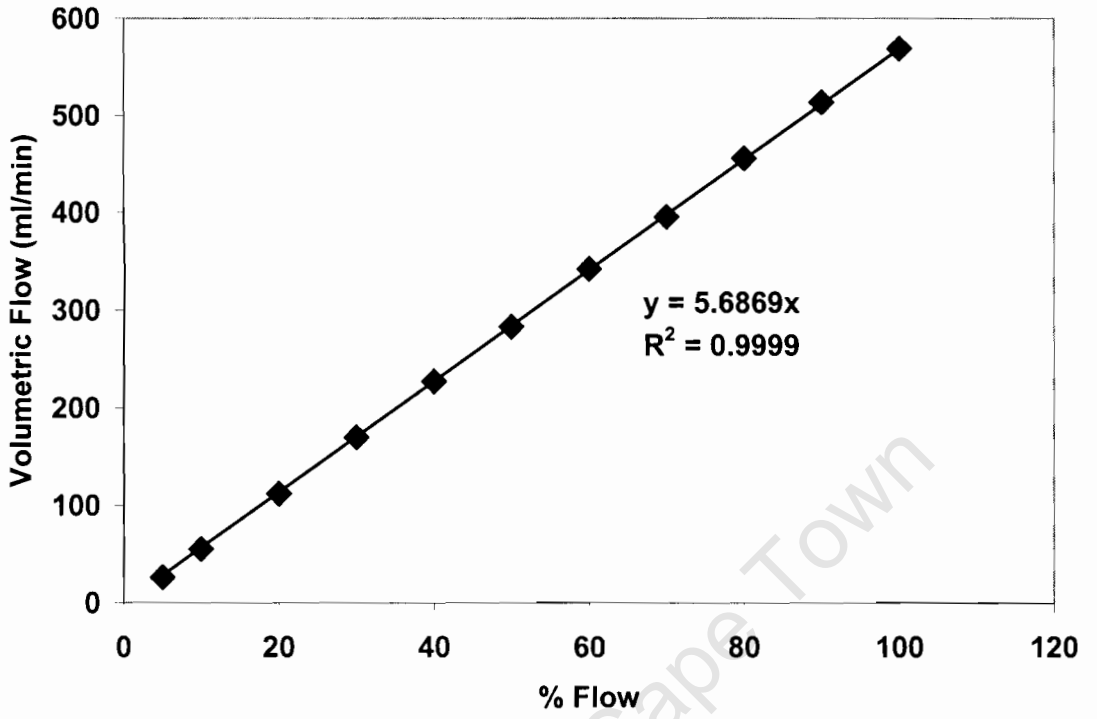

Figure A- 4. Mass flow calibration curve for synthetic air for the calcination unit.

Appendix B

The following figures represent the XRD spectra which were used to identify and characterize the calcined nanotube catalyst.

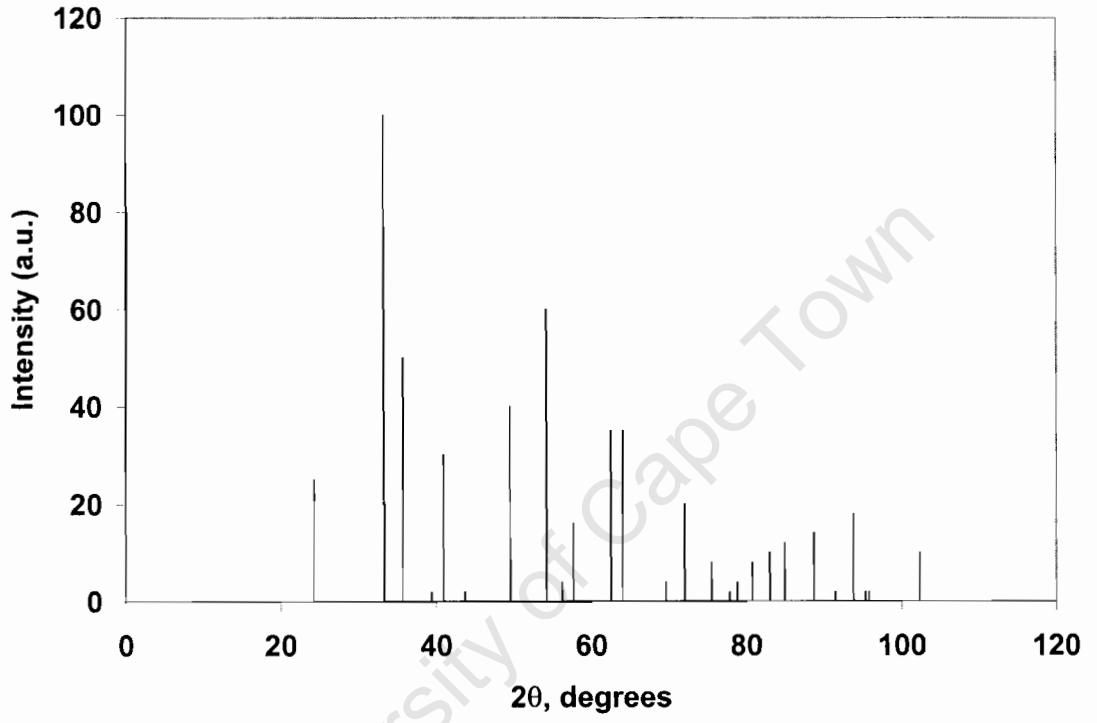

Figure B- 1. Reference XRD pattern for hematite (syn) (Fe_2O_3).

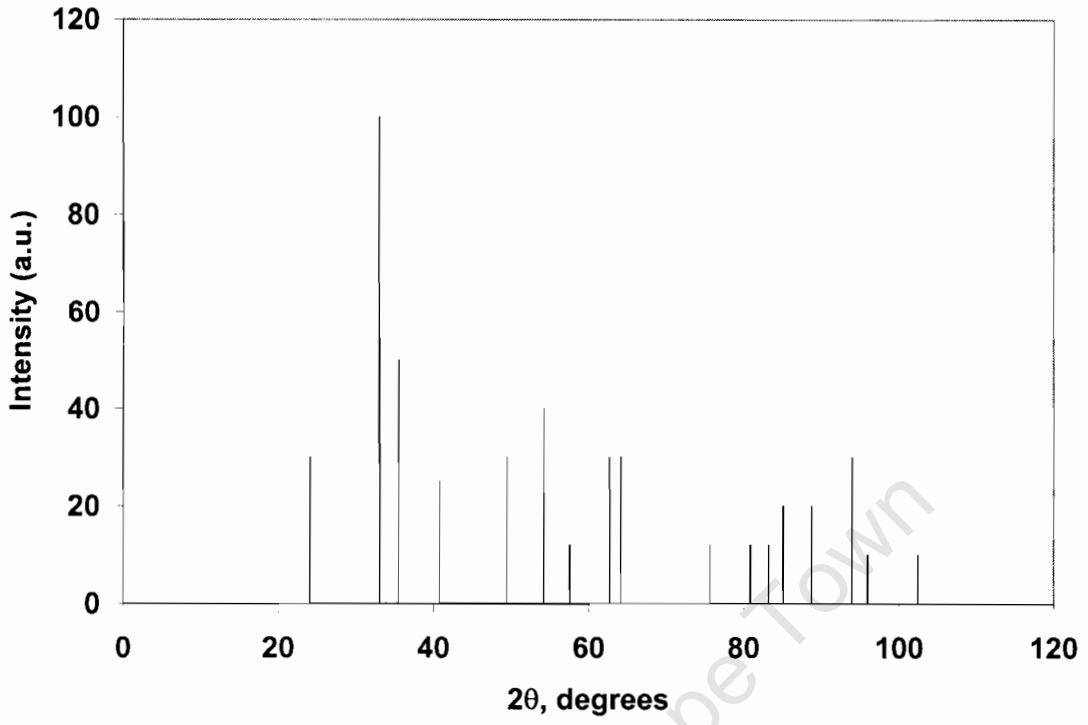

Figure B- 2. Reference XRD pattern for α-Fe_2O_3.

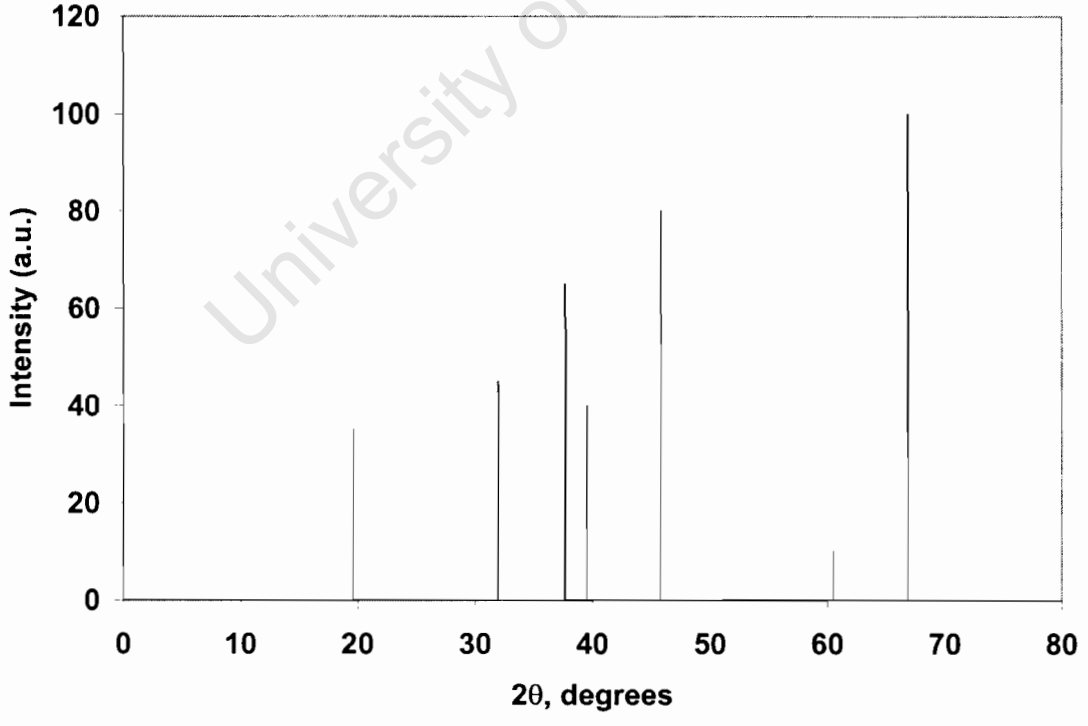

Figure B- 3. Reference XRD pattern for γ-alumina.

Appendix C

The productivity was determined gravimetrically by weighing the catalyst before and the spent catalyst after nanotube synthesis. The following is an example of the how the productivity was calculated taking into account the loss of oxygen during the reduction of the catalyst.

Sample: WS 5-40
Synthesis Temperature: 520°C
Synthesis Time: 7hrs
Initial Catalyst Mass: 0.1998g
Iron Loading: 8.5%
Mass after Synthesis: 0.2970g

Mass of iron: 0.085 x 0.1998g = 0.0170g Fe
Mmol of iron: 0.304 mmol Fe
Mmol of oxygen assuming all iron as Fe_2O_3: 0.456 mmol O

Mass of oxygen: 7.297mg O *(This is the mass lost during reduction)*

Mass of carbon produced = Mass of catalyst after nanotube synthesis – Mass of catalyst before nanotube synthesis

Therefore,
Mass of carbon produced = 0.972 g of carbon

Productivity = (Mass of carbon produced + Mass of oxygen lost during reduction)/ (mass of catalyst x synthesis time)

Productivity = 0.0747gC/g_{cat}.hr